

Copyright

by

Kylara Margaret Martin

2011

**The Dissertation Committee for Kylara Margaret Martin Certifies that this is the approved version of the following dissertation:**

**Geophysical investigations in the Nankai Trough and Sumatran subduction zones**

**Committee:**

---

Sean P. S. Gulick, Supervisor

---

Nathan L. B. Bangs

---

Peter B. Flemings

---

Gregory F. Moore

---

Sharon Mosher

---

Luc L. Lavier

**Geophysical investigations in the Nankai Trough and Sumatran  
subduction zones**

**by**

**Kylara Margaret Martin, B.S. Geophysics**

**Dissertation**

Presented to the Faculty of the Graduate School of

The University of Texas at Austin

in Partial Fulfillment

of the Requirements

for the Degree of

**Doctor of Philosophy**

**The University of Texas at Austin**

**December 2011**

## **Dedication**

For my father, who taught me to ask questions,  
and my mother, who taught me to find answers.

## Acknowledgements

Too many people to list have helped and supported me over the last five years, but a few simply must be mentioned. I must thank my advisor, my committee and all of the collaborators who have worked with me in acquiring, processing and interpreting the data presented in this dissertation. In particular, I am fortunate to have had Dr. Sean Gulick as an advisor and role model. His patience in training his students is second only to his enthusiasm for meaningful science. Prof. Peter Flemings, another enthusiastic researcher and teacher, taught me to begin explanations from the fundamentals, regardless of the audience.

Dr. James Austin, Jr. has taught me a great deal about scientific writing and presentations, particularly the value of figures. Prof. Gregory Moore always read what I sent him and responded with both concise feedback and fundamental scientific questions. Both of these notoriously busy men have helped me articulate my contributions to large-scale scientific projects.

Ocean drilling and marine seismic acquisition are large-scale undertakings. I am especially grateful to the captains, crews and scientific staff of the R/V Sonne and D/V Chikyu Hakken, who do incredible work every day and are always willing to explain their crafts to ignorant intellectuals. I also thank the international scientific collaborators involved in the NanTroSEIZE and CRUST projects. My interpretation of the Kumano 3D seismic data would not have been possible without Emily Davies and her detailed interpretation of the megasplay system and Drs. Saneatsu Sato, Yukari Kido, Yoshinori Sanada and Shigenobu Uraki who helped with the 3D pre-stack depth migration processing.

I am grateful to Prof. Carlos Torres-Verdin and Zoya Heidari of the formation evaluation group in the Department of Petroleum and Geosystems Engineering, who helped me with resistivity tool response models. Katrina Czenkusch of the Department of Chemical Engineering very patiently discussed fluid transport me on a number of occasions. As my godsister, she is required to help me at times, but extensive discussion of dimensionless quantities on Saturday afternoons is above and beyond her obligations. I also must thank Joanne Tudge, who first introduced me to the theory behind well logging and somehow still listens to me.

I owe my remaining sanity to the UTIG staff, particularly Mark Wiederspahn, Steffen Saustrup and Tom Hess, who lent me their technical expertise, and to Judy Sansom who makes the finances run so smoothly. My fellow graduate students at UTIG have also helped me in a thousand little ways, for which I am most grateful.

Dr. Nick Tanushev patiently checked much of my math, even when the concepts were a bit obscure, and always encouraged me. Christina Dwyer/Wasem, Katherine Richardson and a number of other Caltech alumni have kept me going through encouragement, proofreading, critical commentary and lively discussion. My undergraduate advisor, Prof. Joann Stock, is still our role model. I am glad to have been one of the young female scientists she took under her wing (and out to sea).

My research has been supported by several National Science Foundation grants to the University of Texas at Austin and by a postexpedition award from the Consortium for Ocean Leadership for work on data from the Integrated Ocean Drilling Program (IODP) Expedition 314. I have been privileged to receive additional support in the form of a Fellowship in Exploration Geophysics from the Jackson School of Geosciences, the Chevron Energy Technology Company Scholarship and the Gale White Fellowship and Arthur Maxwell Fellowship, both at the University of Texas Institute for Geophysics.

# **Geophysical investigations in the Nankai Trough and Sumatran subduction zones**

Kylara Margaret Martin, Ph.D.

The University of Texas at Austin, 2011

Supervisor: Sean P. S. Gulick

The 2004 Sumatra-Andaman and the 2011 Tohoku-Oki earthquakes demonstrate the importance of understanding subduction zone earthquakes and the faults that produce them. Faults that produce earthquakes and/or tsunamis in these systems include plate boundary megathrusts, splay faults (out of sequence thrusts), and strike-slip faults from strain partitioning. Offshore Japan, IODP Exp. 314 collected logging while drilling (LWD) data across several seismically-imaged fault splays in the Nankai Trough accretionary prism. I combine LWD resistivity data with a model of fluid invasion to compare the permeabilities of sands. My results indicate that sands within faulted zones are 2-3 orders of magnitude more permeable than similar undisturbed sands. Therefore fault zones are likely to be fluid conduits within the accretionary wedge. Fluids can affect the physical and chemical properties of the faulted material, increasing pore pressures and effectively lubricating the faults.

Fluids play an important role in fault slip, but hazard analysis also requires an understanding of fault geometry and slip direction. Both Japan and Sumatra exhibit strain partitioning, where oblique convergence between tectonic plates is partitioned between the megathrust and strike-slip faults proximal to the arc. Offshore Sumatra, I combine profiles from a 2D seismic survey (SUMUT) with previous bathymetry and active seismic surveys to characterize the West Andaman Fault adjacent to the Aceh forearc

Basin. Along this fault I interpret transpressional flower structures that cut older thrust faults. These flower structures indicate that the modern West Andaman Fault is a right lateral strike-slip fault and thus helps to accommodate the translational component of strain in this highly oblique subduction zone.

Offshore the Kii Peninsula, Japan, I analyze a trench-parallel depression that forms a notch in the seafloor just landward of the megasplay fault system, along the seaward edge of the forearc Kumano Basin. Using a 12 km wide, 3D seismic volume, I observe vertical faults and faults which dip toward the central axis of the depression, forming apparent flower structures. The along-strike geometry of the vertical faults makes predominantly normal or thrust motion unlikely. I conclude, therefore, that this linear depression is the bathymetric expression of a transtensional fault system. While the obliquity of convergence in the Nankai Trough is small (~15 degrees), this Kumano Basin Edge Fault Zone could be due to partitioning of the plate convergent strain. The location of the West Andaman Fault and KBEFZ within the forearc may be controlled by the rheology contrast between active accretionary wedges and the more stable crust beneath forearc basins.

## Table of Contents

List of Tables .....	xii
List of Figures .....	xiii
Chapter 1: Introduction .....	1
Chapter 2: Estimating depth of invasion and permeability from LWD resistivity logs in NanTroSEIZE sands .....	8
Abstract .....	8
General background .....	9
Determining Permeability .....	10
Study Area .....	12
Data .....	15
Model .....	18
Formation Invasion Model .....	19
Invasion Model Discussion .....	22
Tool Response .....	24
Sample Selection and Observations .....	30
C0001D .....	30
C0004B .....	35
C0006B .....	40
Results and Discussion .....	42
Model Application .....	42
General Results .....	44
Uncertain Model Parameters .....	47
Absolute Permeability Magnitude .....	48
Future Work .....	49
Conclusions .....	50

Chapter 3: The Kumano Basin Edge Fault Zone as a Potential Strain Partitioning Structure between the Kumano Basin and the Slope of the Nankai Trough Accretionary Prism .....	53
Abstract:.....	53
Introduction:.....	54
Nankai Trough Tectonic Setting.....	56
Data:.....	59
Methods: .....	60
Observations: .....	62
Interpretations: .....	68
Discussion:.....	69
Effect of underlying splay fault: .....	70
Strain Partitioning: .....	73
Implications: .....	76
Conclusions:.....	79
Chapter 4: The West Andaman Fault as strike-slip, strain-partitioning feature at the edge of the Aceh Basin .....	81
Abstract.....	81
Introduction.....	82
Tectonic Setting .....	85
Study Area/Previous Work .....	88
Aceh Basin.....	88
West Andaman Fault.....	90
Tuba Ridge and Tuba Basin.....	92
Data .....	93
Structural Analysis.....	95
Aceh Basin.....	95
Basal Unconformity.....	96
Major Sequence Boundary.....	97
Sequence A .....	100
Sequence B.....	101

West Andaman fault .....	103
Tuba Ridge.....	106
Discussion .....	108
West Andaman Fault.....	108
Thrust Faults .....	109
Quantifying Slip.....	111
Implications.....	112
Conclusions.....	113
Chapter 5: Conclusions .....	115
Appendices.....	119
Appendix A: Advection vs. Diffusion in Non-dimensional analysis .....	119
Appendix B: Fluid Invasion Model Code.....	122
Carslaw_k.m .....	122
ODErhs .....	123
Appendix C: Boundary Flux Method for Fluid Invasion Model .....	124
Boundary_flux.m .....	124
stiffness_test.m.....	125
Appendix D: Pressure Assumptions for Fluid Invasion Model .....	130
Appendix E: SUMUT Survey Processing Flow .....	133
Appendix F: SUMUT Pre-stack Migration Processing Flow .....	140
Appendix G: Example Pre-stack Depth Migrations .....	142
References.....	144

## **List of Tables**

Table 2.1: Invasion Model Parameter Values.....	23
Table 2.2: Tool Response Model Parameters .....	27
Table 2.3: Samples used in quantitative analysis.....	29
Table 2.4: Nomenclature uand Acronyms .....	51
Table 3.1: Mapped faults classified by dip and apparent offset where possible....	64
Table 4.1: Calculated dips of interpreted faults in Figures 4.3-4.6.....	91

## List of Figures

- Figure 1.1: Effect of increased pore pressure on Mohr's Circle. Increased pore pressure decreases effective normal stress, moving Mohr's Circle to the left and nearer the failure envelope.....2
- Figure 1.2: Fault-zone reflector in Nankai Trough seismic images. a) 2d seismic image with a negative polarity reflector along the megasplay fault [*GF Moore et al.*, 2007]. b) 3d seismic volume with cut-out showing high-amplitude, reverse-polarity reflection from the splay fault (red) [*Bangs et al.*, 2009]. Black lines are splay fault branches and blue lines are accretionary wedge thrusts. Blue shaded area is underthrust layer between splay fault and top of the subducting ocean crust.....4
- Figure 1.3: Schematic diagrams of partitioned strain at an oblique subduction zone. Oblique convergence at the margin is partitioned into thrust on the plate boundary fault and shear on a strike-slip fault, often proximal to the arc. Modified from Fitch et al. [1972]. .....6

Figure 2.1: Location of study. a) Location of sites drilled during previous ODP Legs 87, 131, 190 and 196 (Ashizuri and Muroto Transects) on a shaded relief map of the Nankai Trough (Hydrographic Department of Japan's topographic data set, 500 m grid interval). Kumano Transect sites used in this paper are shown as red circles on composite seismic line at far right. [Modified from *Mikada et al.*, 2005] b) Bathymetry of the Nankai Trough, showing the location of the Kumano 3-D seismic volume, megasplay fault and Kumano Basin Edge Fault Zone (KBEFZ). Black line is the location of the composite seismic line shown in (c), which passes through or near Sites C0001-C0008. Inset shows the regional setting of the Nankai Trough. PSP = Philippine Sea Plate; KPR = Kyushu-Palau Ridge; IBT = Izu-Bonin Trench; KP = Kii Peninsula, SI = Shikoku Island. [Modified from *G F Moore et al.*, 2007] c) Interpreted composite seismic line extracted from the Kumano 3-D seismic volume. with labeled drill sites. Morphotectonic zones are labeled between the two sections. PTZ = protothrust zone, BSR = bottom simulating reflector, VE = vertical exaggeration. [Modified from *G F Moore et al.*, 2009] .....14

Figure 2.2: Example section of C0001D with resistivity log separation. All resistivity tracks are on a linear scale. The Resistivity Difference log is the calculated difference between shallow and deep button resistivities. The ring resistivity log is similar to the deep button log, but the bit resistivity log has too high of a sampling volume to respond to beds this thin. The caliper log is shaded above 9.5 inches and shaded red above 10.5 inches. Note that sometimes the resistivity difference changes with the caliper log (red arrows) and sometimes it does not (black arrows). The gamma ray log indicates sandy layers at 496 and 502 m LSF (Sands C and D). Sand C is associated with a caliper high and sand D with a caliper low, arguing that borehole width alone does not control the resistivity difference and formation invasion is also occurring. ....16

Figure 2.3: Radial formation invasion model. a) Schematic borehole diagram. b) Normalized radial pressure profile. Numbers on curves are values of normalized time,  $\tau = Cvt/a^2$ . c) Resistivity profile through time. Numbers on curves are values of  $\tau = Cvt/a^2$ . d) Distance of invasion as a function of time assuming parameter values in Table 2.1. ....20

Figure 2.4: Tool response model for the Schlumberger High-Resolution Laterolog Array (HRLA) tool. a) Input scenario.  $R_w$  = Formation water resistivity and  $R_{mf}$  = mud filtrate resistivity, which is assumed to be near  $R_m$ , that of seawater.  $R_{\chi 0}$  and  $R_t$  are the resistivities of the fully invaded and uninvaded formation respectively. b) Tool response in the form of apparent resistivity measured by each focusing mode (R1-5 where R1 is the mode with the shallowest depth of investigation) as a function of distance of invasion ( $d_i$ ). ....28

Figure 2.5a: C0001D summary log diagram. Logging units defined by shipboard scientists. Gamma ray log used to identify sandy lithologies. All resistivities are plotted on a linear scale. Button resistivities are the average of the azimuthal resistivity values from any given depth for each button sensor. Ring and Bit resistivities have higher sampling volumes than the button sensors. Resistivity Difference is the deep button resistivity minus the shallow button resistivity, with positive values shaded in green. The caliper log is shown with a baseline of 9.5 inches and a reference line at 10.5 inches. Calipers greater than 9.5 inches are shaded and calipers greater than 10.5 inches are colored red. Sonic log is given in units of slowness. Time After Bit (TAB) log shows regular increases where stand changes occurred and less regular anomalies where drilling operations encountered difficulties, generally in faulted zones. Seismic section from the Kumano 3D seismic volume showing interpreted faults. Samples chosen for analysis marked with purple lines and labeled at right. [Modified from *Expedition 314 Scientists*, 2009a]

.....33

Figure 2.5b: Expanded sections of gamma ray, resistivity and caliper logs around each of the samples highlighted in (a). .....34

Figure 2.6a: C0004B summary log diagram. See Figure 2.4 for panel descriptions. Samples chosen for analysis marked with purple lines and labeled at right. Fracture zones identified by onboard scientists are highlighted. Yellow zones correspond to TAB anomalies. Green zones are not solely related to TAB anomalies and likely fractured. [Modified from *Expedition 314 Scientists*, 2009c] .....37

Figure 2.6b: Expanded sections of gamma ray, resistivity and caliper logs around each of the samples marked with purple in (a). .....	38
Figure 2.7: Expanded section from C0004B (Figure 2.6). Illustrates the correspondence of a fracture zone picked by onboard scientists (highlighted in yellow), anomalously conductive resistivity image log and high time after bit (TAB). .....	39
Figure 2.8: C0006B summary log diagram. See Figure 2.4 for panel descriptions. Units I and IV have very high caliper values. In Units II and III, note clear correspondence of high resistivity differences to both low gamma ray values and high caliper. We present this hole as an example of conditions under which our method cannot be applied. [ <i>Expedition 314 Scientists</i> , 2009b] .....	41

Figure 2.9: Model Results. Time after bit (TAB) vs. invasion distance (from tool response model) for each sample plotted over a chart of modeled invasion profiles for varying permeability. Log and model values for each point are in Table 2.3. Parameters used to create invasion profile curves shown in Table 2.1. Circles around samples with high caliper values; these samples are likely reading artificially elevated permeabilities due to washouts. a) C0001D samples. Samples in faults correspond to higher permeability curves than sands not in faults. Sands with caliper values > 10.5 inches also correspond to higher permeability curves than sands with lower caliper values. Low pressure samples from shallower depths (denoted by squares) were drilled with a lower rig floor pumping rate and should only be compared with each other. b) C0004B samples. Two sands (E and F) with different TAB correspond to similar permeabilities (30 and 12 mD). Sand G, which has a high caliper value, shows somewhat elevated permeability. Sand from a faulted zone (Fault C) shows a permeability ~2.5 orders of magnitude above sands not in faulted zone.....43

Figure 3.1: Bathymetry of the Nankai Trough, showing the location of the 3-D seismic survey and previously interpreted faults. The notch feature discussed in this paper crosses near the center of the 3-D survey area, striking NE-SW. The portion of the feature imaged by the 3D seismic dataset is 750 m deep and 3 km across in the northeast and splits to the southwest into several parallel ~250 m deep depressions across a zone of deformation approximately 5 km wide. The deepest part of this feature (~1.2 km deep) is found northeast of the study area. The convergence direction between the Philippine Sea Plate and the Eurasian plate is shown at the lower right [*Seno et al.*, 1993]. Inset shows the regional setting of the Nankai Trough. PSP = Philippine Sea Plate; KPR = Kyushu-Palau Ridge; IBT = Izu-Bonin Trench; KP = Kii Peninsula; Sh = Shikoku Island; Ky = Kyushu Island. [Modified from *G F Moore et al.*, 2007] .....58

Figure 3.2: Bathymetry Maps. a) Bathymetric map generated from the seafloor reflection picked in the 3D seismic data. The notch is deep and narrow to the northeast and shallower and wider to the southwest. Note the linear feature in the right-hand (NE) portion of the depression (arrow). This feature, more evident in the side-scan sonar image to the right, corresponds to the central fault mapped below the northeastern notch (see Figure 3.3). b) Side-scan sonar image draped over bathymetry; collected by deep-tow side-scan sonar Wadatsumi over the forearc Kumano Basin and forearc slope [Ashi *et al.*, 2007]. Yellow dots indicate proposed NanTroSEIZE sites which have now been drilled (IODP sites C0002 and C0003). c) Bathymetric map showing mapped fault locations. Faults which appear to be transform in nature are shown with an offset direction based on convergence direction. Based on the correspondence between faults and bathymetric features, we introduce the idea that the notch is the surface expression of a Kumano Basin Edge Fault Zone (KBEFZ).....61

Figure 3.3: (a-c) Cross sections (in depth) of the notch and (d-f) corresponding interpretations. Sections are displayed with no vertical exaggeration. The notch feature is a linear bathymetric low along the edge of the forearc Kumano Basin and in the hanging wall of the uppermost branch of the megasplay fault system [G F Moore *et al.*, 2007]. A bottom-simulating reflector (BSR) is evident in most of the study area.....67

Figure 3.3 (continued): a) Northeast inline (2650): The notch is narrow (~3 km wide and ~0.75 km deep) with basin sediments truncated by faults bounding the bathymetric low. Faults are mostly steep and occasionally vertical or sinuous, indicating a possible strike-slip nature. The vertical fault at center corresponds to a linear feature in the bathymetry (Figure 3.2). b) Central Inline (2464): The coherent basin sediments begin stepping to the northwest. Steep faulting along the edge of the basin is more laterally continuous than that in the center of the notch. The megathrust splay is deeper here than in the northeast. c) Southwest Inline (2265): Characterized by distinct blocks of sediment where the basin boundary continues to retreat northwest. These sediment blocks may be remnants of basin packages disrupted by faulting. The bathymetric low is wider than that in the northeast and encompasses several shallow depressions. The geometry of the megathrust splay is similar to that in the central part of the study area, placing it deeper than in the northeast.....68

Figure 3.4: Block diagram of KBEFZ (“notch”) and surroundings. Note the corkscrew geometry of the megasplay fault, which twists up to the northeast within the 3d seismic dataset.....71

Figure 3.5: Tectonic setting comparison between Nankai and Sumatra. Major earthquake epicenters and approximate rupture areas are in red. In Sumatra [diagram modified from *Mosher et al.*, 2008], strike-slip faults are found within the volcanic arc (the Sumatra Fault) and along the seaward edge of the forearc basins (West Andaman and Mentawi Faults). Oblique convergence along the margin is partitioned between these strike-slip faults and the megathrust. In Japan, the Median Tectonic Line (MTL) is a strike-slip fault within the volcanic arc and the KBEFZ is a strike-slip fault along the seaward edge of the forearc basin. The Enshu and Kodaiba Faults (EF and KF respectively) are the main strike-slip faults to the northeast associated with subduction of the Izu-Bonin ridge. Oblique strain is known to be partitioned between the MTL and the megasplay fault system. Could the KBEFZ be further evidence of partitioned strain localizing in the forearc? .....74

Figure 4.1: Maps of the Sunda Trench and forearc. Red stars are the epicenter of the 2004 Sumatra-Andaman earthquake. a) Regional tectonic setting. The boundary between Australia and India is a diffuse plate boundary between ~5 S and ~8N [DeMets et al., 2005]. Plate velocities of Australia (orange arrows) and India (red arrows) relative to Sunda modified from Subarya et al. [2006]. Fault traces modified from Cochran et al., 2010 and McCaffrey et al., 2009: AS, Aceh Strand of the Sumatran Fault; BF, Batee Fault; DF, Diligent Fault; EMF, Eastern Margin Fault; SS, Seulimeum strand of the Sumatran Fault; WAF, West Andaman Fault. b) Map of the forearc offshore northern Sumatra showing the seismic surveys used in our analysis. SEATOS in pink, BGR06 in Gray and SUMUT in orange. c) Bathymetry of the central and southern Aceh Basin with locations of the seismic lines shown in Figures 2-4. ....84

Figure 4.2: Previous interpretations of the Aceh Basin. West Andaman Fault Zone (WAF). a) BGR06-107, modified from Berglar et al. [2010]. b) Profile 18 from Seeber et al. [2007] .....89

Figure 4.3: SEATOS lines crossing WAF in the northern part of the study area.

Interpreted Sequence boundaries, marker horizons and faults, particularly steep basin-edge fault traces (Group A). Locations shown in Figure 1c. Line crossings indicated at the top of sections. a) SEATOS-26: Dipping Group E faults separated by a steep slope with possible slumps. b) SEATOS-25: Dipping Group B and C faults interspersed with anticlinal folds in former basin sediments. Surfaces B1 and B2 interpreted based on similarity of basin sediment reflectors to those in SEATOS-24 (c). c) SEATOS-24: Surfaces B1 and B2 show anticlinal folding in WAF (interpreted from line crossings between SEATOS, SUMUT and BGR surveys).....97

Figure 4.4: Multichannel seismic lines crossing the WAF in the northern part of the study area. a) Pre-stack migrated MCS section of SUMUT-03:

uninterpreted on the left and interpreted on the right. Apparent flower structure (Groups A, B and C faults) cuts shallower-dipping thrust faults (Group D, shown in pink). b) Section of MCS line BGR06-107: [Berglar *et al.*, 2010], with additional interpretation. Features are similar to those interpreted on SUMUT-03, with the addition of Group E faults imaged to the west. ....98

Figure 4.5: Seismic lines in the southern part of the Aceh Basin area. Uninterpreted sections above, interpreted sections below show Sequence boundaries, marker horizons and faults. Locations shown in Figure 1c. Line crossings indicated at the top of sections. VE~3X. a) Pre-stack migrated section of SUMUT-05: Group A, B and C faults form a flower structure offsetting Group D thrusts. b) Pre-stack migrated section of SUMUT-07: Wider zone of basin edge deformation than to the north. Steeply-dipping faults form an apparent flower structure, whereas thrust faults offset only the oldest basin sediments.....99

Figure 4.6: Seismic lines in the south (crossing the Tuba Ridge) with interpreted Sequence boundaries, marker horizons and faults. Locations shown in Figure 1c. Line crossings indicated at the top of sections. Faults within the Tuba ridge form an apparent flower structure. T1, T2 and T3 shown on bathymetry in Figure 4.7. a) Section BGR06-143/144 modified from Berglar et al. [2010]: Sequence boundaries interpreted in the Aceh basin to the NW. Berglar et al. correlate the base of the Tuba Basin with Surface A1, the base of the Aceh Basin. Faults below A1 in the Tuba Basin have apparent normal offset. b) Pre-stack migrated section of SUMUT-01: Uninterpreted above, interpreted below. ....102

Figure 4.7: Maps of tectonic interpretation. a) Interpreted bathymetry in the Aceh Basin area. Seafloor traces of interpreted fault Groups A, B, E and T labeled. Black lines are Group C fault traces (Group D does not reach the seafloor). Orange dashed lines are traces of apparent plateau faults in the bathymetry data. Strike-slip West Andaman Fault may bifurcate near the intersection with the Tuba Ridge [Seeber *et al.*, 2007]. The possible SSE-striking branch is indicated by dashed purple line. The other branch curves to the east, forming the pop-up structure of the Tuba Ridge. b) Interpretation from (a) shown in a regional context. Sense of motion indicated by arrows. Red star is epicenter of the 2004 Sumatra-Andaman earthquake. ....107

Figure 5.1: Cross sections of subduction zones showing partitioned strain in the forearc. a) Sumatran Subduction Zone [Malod and Kemal, 1996]: Shows the position of the Mentawai Fault near central Sumatra, which is equivalent to the position of the WAF in the north. b) Nankai Trough Subduction Zone: Shows location of the strike-slip KBEFZ between the Inner and Outer Wedge [Modified from Kimura *et al.*, 2007]. .....117

Figure A.1: Peclet Number vs Time for a range of formation permeabilities .....120

Figure A.2: Same as Figure A.1 on a semilog plot.....121

Figure D.1: Pressure plot from C0006B. The hydrostat (red) is calculated using a water density of 1.024 g/cc and the lithostat (green) using 2.3 g/cc. Both are assumed equal to the APRS log value at the seafloor (to eliminate any issues with how water depth was measured and temperature throughout the water column). ....130

Figure D.2: Pressure plot for C0001. C0001A is the pilot hole and C0001D was logged by the LWD string. Rig floor pumping rate is from hole C001D. Figure courtesy of Casey Moore.....131

## Chapter 1: Introduction

Subduction zones are some of the most geologically hazardous areas of the world. The largest earthquakes (Chile 1960, Alaska 1964, Sumatra 2004) and many of the deadliest tsunamis (Sumatra 2004, Chile 1868, Japan 1498 and 2011) on record are subduction-related [e.g. Dunbar, 2008; Satake and Atwater, 2007]. With the exception of Chile, most of the subduction zones that have produced the largest historical earthquakes and tsunamis are characterized by accretionary wedges. Accretionary wedges form in subduction zones as sediment is scraped off the down-going plate and accreted to the overriding plate [e.g. *Dahlen et al.*, 1984; *Davis et al.*, 1983]. The societal impact of large, often tsunamigenic, seismic events in accretionary subduction zones makes an understanding of the stresses, strains and structures within the accretionary wedges imperative.

This dissertation consists of three studies conducted in two subduction zones, one offshore southeastern Japan and the other offshore northwestern Sumatra. Each study is part of international, multidisciplinary collaborative projects aimed at understanding particular aspects of these subduction zones, from the role of faults as potential fluid conduits to the occurrence of strain partitioning. Both of these aspects of subduction zone processes have implications for where faults form, which faults rupture seismogenically and the direction of slip when faults do rupture.

As sediments on the overriding plate are compacted and buried within the accretionary wedge, the pore water is forced out [e.g. *Neuzil*, 1995; *Saffer and Bekins*, 2002]. This tectonic loading and the resulting fluid supply combined with low-permeability marine sediments can lead to pore pressures elevated well above hydrostatic within the accretionary wedge [e.g. *Saffer*, 2010]. As accretionary wedges are shaped by

faulting processes, the influence of high pore pressures on these faults, particularly the décollement is important to the overall wedge mechanics [e.g. *Davis et al.*, 1983; *Saffer*, 2010; *Saffer and Bekins*, 2002].

The role of fluids in faults has been recognized since the work of Hubbert and Rubey [1959]. A cushion of high-pressure fluid along a fault facilitates lateral movement of the overlying rock. In terms of failure analysis, an increase in pore pressure decreases effective normal stress, moving Mohr's Circle to the left and nearer to the failure envelope (Figure 1.1). Once faults have formed, they are likely to be the weakest parts of the formation and will slip before the formation itself fails (until/unless the fault orientation is no longer close enough to the direction of maximum shear stress).

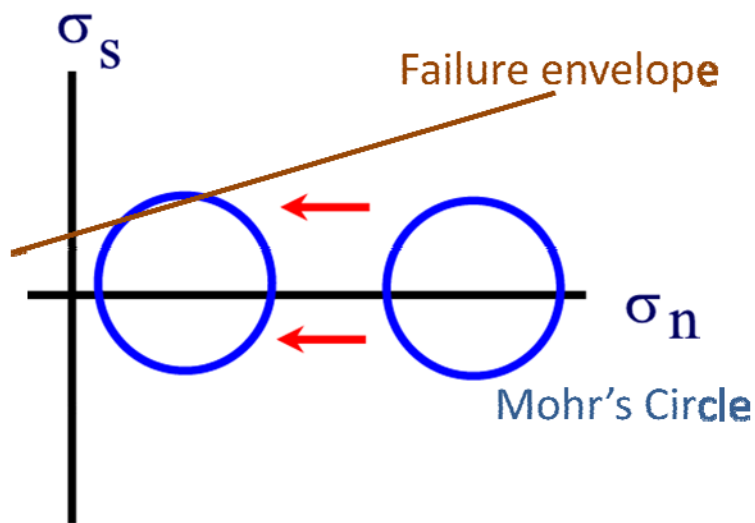


Figure 1.1: Effect of increased pore pressure on Mohr's Circle. Increased pore pressure decreases effective normal stress, moving Mohr's Circle to the left and nearer the failure envelope.

Fracturing and dilation within the fault zone could also enhance permeability, making faulted zones conduits for enhanced fluid flow within the accretionary wedge. If this effect is transitory or other processes (sediment alteration or cementation) block these conduits over time [Gulick and Bangs, 2004], pore fluids will build up higher pressures. Even with elevated permeabilities, the volume of fluids forced out of sediments may still be higher than the volume that can escape along the faulted zones, and pore pressures may still be elevated [Saffer, 2010; Saffer and Bekins, 2002].

Pore pressures above hydrostatic can cause sediments to be underconsolidated, with higher porosities and lower sound velocities than would be expected of normally consolidated sediments under the same gravitational and tectonic stresses [Bangs *et al.*, 1996; J C Moore *et al.*, 1998; Neuzil, 1995; Saffer, 2010]. Higher porosity means lower bulk density, which combines with lower sound velocities to decrease seismic impedance. A decrease in seismic impedance within or across a faulted zone leads to negative polarity reflections in seismic images [e.g. G F Moore *et al.*, 2007; J C Moore *et al.*, 1995; Shipley *et al.*, 1994]. The megasplay fault observed in the Nankai Trough subduction zone is an example of a fault within an accretionary wedge that exhibits negative polarity reflections in seismic images (Figure 1.2a) [G F Moore *et al.*, 2007; G F Moore *et al.*, 2009; Park *et al.*, 2002]. Park *et al.* [2002] and Bangs *et al.* [2009] used this reflectivity to argue for higher pore pressures within and below the megasplay fault, implying that this fault may be the active seismogenic fault within this system (Figure 1.2b).

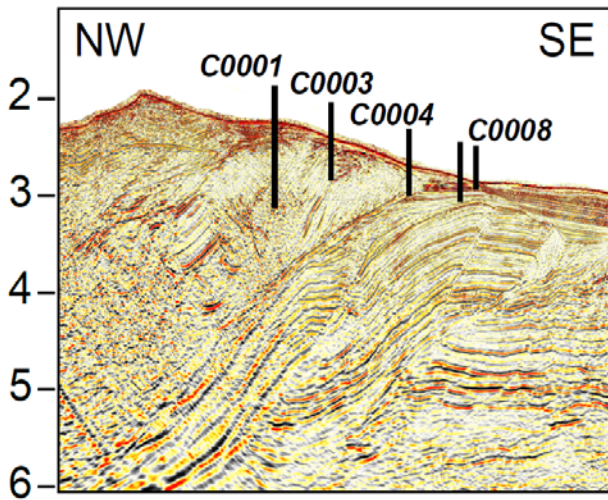
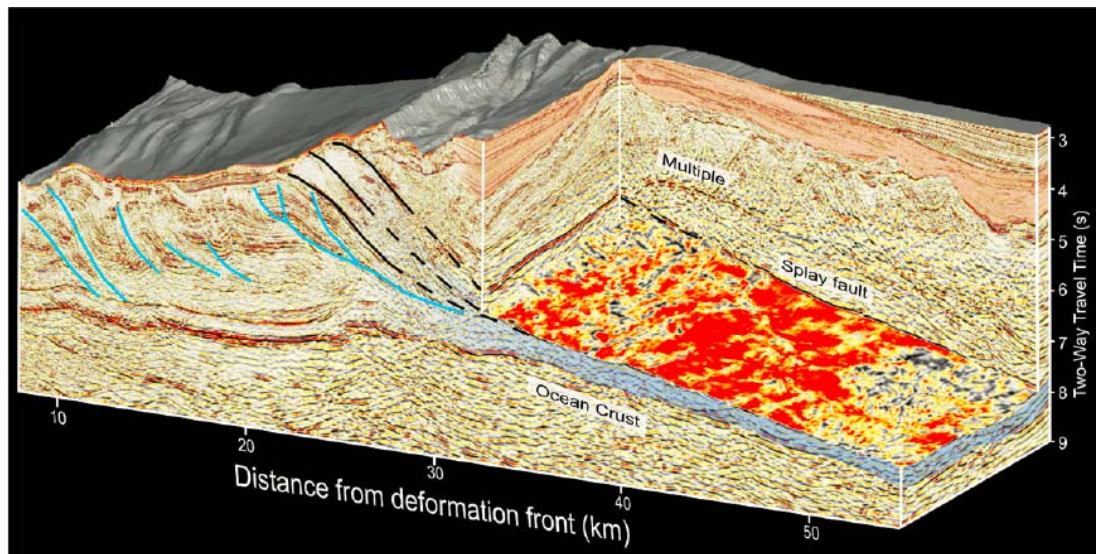


Figure 1.2: Fault-zone reflector in Nankai Trough seismic images. a) 2d seismic image with a negative polarity reflector along the megasplay fault [G F Moore *et al.*, 2007]. b) 3d seismic volume with cut-out showing high-amplitude, reverse-polarity reflection from the splay fault (red) [Bangs *et al.*, 2009]. Black lines are splay fault branches and blue lines are accretionary wedge thrusts. Blue shaded area is underthrust layer between splay fault and top of the subducting ocean crust.



Reflective splays of megasplay fault are shallow enough to be reached by drilling. If the megasplay fault is indeed a seismogenic plate boundary thrust, it provides the unique opportunity to observe one of these faults in both downhole logs and cores, which is the eventual goal of the Nankai Trough Seismogenic Experiment (NanTroSEIZE) [Ashi *et al.*, 2007; Kinoshita *et al.*, 2007]. Chapter 2 describes a model of fluid invasion into the formation around the NanTroSEIZE boreholes. Combining this invasion model

and a tool response model, I analyze logging while drilling (LWD) resistivity logs to estimate permeability in sands. I then compare the modeled permeabilities of undisturbed sands to those of sands within fault zones. My results show that faulted sands are generally more permeable than unfaulted sands, supporting the idea of faults as conduits for fluid flow within the accretionary prism.

Chapters 3 also focuses on the Nankai Trough. I utilize the same 3d seismic dataset used to locate the NanTroSEIZE boreholes [*Bangs et al.*, 2009; *Gulick et al.*, 2010; *G F Moore et al.*, 2007; *G F Moore et al.*, 2009] to study a trench-parallel bathymetric notch just landward of the megasplay fault trace. My three-dimensional analysis shows that this bathymetric depression is caused by a transtensional system of sub-seafloor faults. The apparent offset on this system of faults (dubbed the Kumano Basin Edge Fault Zone or KBEFZ) is consistent with the direction of obliquity in the plate convergence vector at this margin. The KBEFZ may therefore be a zone of localization for partitioned shear strain.

In subduction zones characterized by convergence that is oblique to the plate boundary, partitioning of strain between a plate-boundary megathrust and a trench-parallel transform fault or set of faults is commonly observed (Figure 1.3) [Fitch, 1972]. This partitioning results in a system of faults, typically located near the volcanic arc, which can produce significant strike-slip earthquakes. Examples include the Sumatra fault [*Fitch*, 1972; *Jarrard*, 1986] and the Median Tectonic Line in southern Japan [*Nishimura and Hashimoto*, 2006; *Tabai et al.*, 2002].

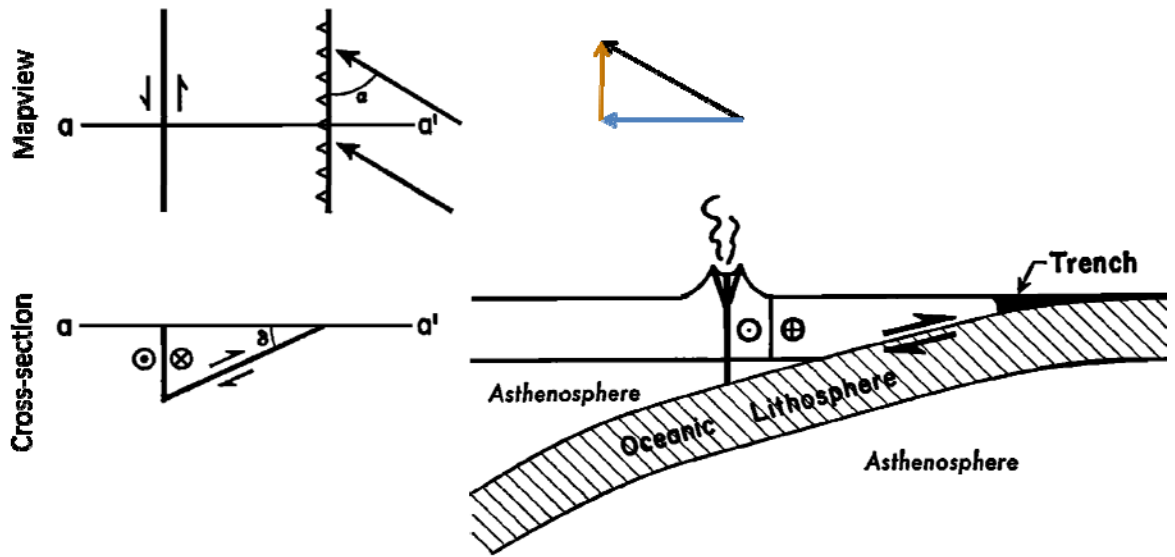


Figure 1.3: Schematic diagrams of partitioned strain at an oblique subduction zone. Oblique convergence at the margin is partitioned into thrust on the plate boundary fault and shear on a strike-slip fault, often proximal to the arc. Modified from Fitch et al. [1972].

Most studies of strain partitioning focus on strike-slip faults near or beneath the volcanic arc, but some margin-parallel motion may occur offshore as well. The West Andaman and Mentawi Fault systems offshore northern and central Sumatra are thought to accommodate a significant amount of dextral transform motion [Malod and Kemal, 1996; Samuel and Harbury, 1996]. Strike-slip faults extend offshore from Hispaniola and many of the observed transform faults along the Cascadia margin are in the submarine forearc. I therefore investigate whether strike-slip faults caused by strain partitioning in oblique subduction zones can nucleate offshore, in the forearc, as well as along the volcanic arc.

Chapter 4 also focuses on the idea of partitioned shear strain localizing in the forearc of an oblique subduction zone. Offshore northern Sumatra, on the seaward edge

of the Aceh forearc Basin, the West Andaman Fault has been interpreted both as a strike-slip [Berglar *et al.*, 2010; Mosher *et al.*, 2008] fault and as a backthrust that may penetrate all the way to plate boundary thrust at depth [Chauhan *et al.*, 2009; Singh *et al.*, 2011]. I utilize several 2d seismic surveys, including the SUMUT survey which was acquired and processed (Appendix E and F) as part of my work, to choose between these two interpretations. The occurrence of flower structures in every crossing of the West Andaman Fault implies to us that this fault is indeed strike-slip. I find no evidence of a modern backthrust at the edge of the Aceh Basin.

These conclusions place a strike-slip fault at the boundary between the forearc basin and the marginal plateau, a position similar to that of the KBEFZ between the Kumano forearc Basin and the actively deforming outer wedge. One possible explanation for this similar positioning is that the rheological transition controlling the location of the forearc basin is also conducive to localization of trench-parallel shear strain.

Chapter 5 summarizes the conclusions and implications from these three studies. I also include several appendices, which are listed in the Table of Contents and cited in the text.

## **Chapter 2: Estimating depth of invasion and permeability from LWD resistivity logs in NanTroSEIZE sands**

### **ABSTRACT**

In accretionary subduction zones, sediments from the down-going plate are scraped off to form a thrust wedge. The mechanics of the faults within this complex, including the plate boundary thrust, are thought to be influenced by elevated pore pressures within the wedge. Permeability is a key parameter in the hydrologic models of these systems. We combine a model of fluid invasion from a borehole into the formation with a model of the effect of this invasion on the logging-while-drilling resistivity tool measurements to estimate the relative magnitudes of permeability in sands. We show that the difference between shallow and deep button resistivity measurements can be used to constrain relative magnitudes of permeability between sandy units, even in LWD operations with short time after bit (TAB) and therefore small distances of fluid invasion. This method requires that TAB be known and is sensitive to caliper values. We use this method to estimate the relative magnitude of permeability in silty to sandy formations in the Nankai Trough subduction zone. Results indicate that sands within faulted zones, as identified in seismic images, generally have a higher permeability (by 1-3 orders of magnitude) than those outside the faulted zones. Based on this study, our method is shown to be viable for estimating relative magnitudes of permeability in logged sections of formations with sparse or absent core permeability data.

## GENERAL BACKGROUND

Accretionary wedges form in subduction zones as sediment is scraped off the downgoing plate and accreted to the overriding plate. Accretionary subduction zones have produced some of the largest earthquakes and deadliest tsunamis on record (Sumatra 2004, Java 1883, Japan 1707) [e.g. *Satake and Atwater, 2007*]. The societal impact of such events makes an understanding of the stresses, strains and structures involved imperative.

The hydrology of accretionary wedges has been demonstrated to strongly influence the mechanics and geometry of these wedges [e.g. *Saffer et al., 2010a*]. Incoming sediments are buried and compressed, forcing dewatering and a dramatic decrease in porosity. The low permeabilities of typical marine sediments combined with these expelled fluids can drive pore pressures well above hydrostatic [e.g. *Neuzil, 1994; Screaton et al., 1990*]. Elevated pore pressures reduce the effective stress, decreasing the shear strength of faults and lowering the taper angle of an accretionary wedge [*Davis et al., 1983*].

Because elevating pore pressure decreases effective stress, the pore pressure along faults is important when considering which faults are likely to be active, seismogenic and potentially hazardous. In seismic data, a negative polarity fault zone reflector is used as evidence for a higher porosity, underconsolidated zone, either along the fault itself or in the underthrust sediments below the fault [e.g. *Bangs et al., 2009; J C Moore et al., 1995*]. These underconsolidated sediments imply an excess of fluid and therefore potentially elevated pore pressures which would lower effective stress and allow faults to slip more easily [*Davis et al., 1983*].

Modeling is one of the key tools used to understand subduction zone structures and evolution as well as earthquake size and nucleation [*Lallemand et al., 1994; Saffer*

and Bekins, 2006; Wang and Hu, 2006]. Such models show the importance of pore pressure in wedge mechanics [e.g. Davis *et al.*, 1983; Saffer, 2010]. Saffer and Bekins [2006] found that incoming sediment thickness and permeability were the most important factors when modeling pore pressures in an accretionary wedge, whereas fault permeability and sediment partitioning between accretion and underthrusting both have smaller effects. Pore pressure in models such as this is determined from both analysis and assumptions of porosity and permeability at depth.

Permeabilities used in these models are commonly determined by assuming permeability is proportional to porosity, with the exact relationship constrained through direct measurements in cores. This method of estimation is necessary because permeability is a more elusive variable than porosity. Neutron porosity logs measure formation water content, which yields porosity in sands [Ellis and Singer, 2007; Rider, 2000]. In clay-rich formations, core analysis and spectral gamma ray logs can allow us to estimate quantities of bound water and transform neutron porosity logs into porosity estimates. Porosity can also be estimated from other properties, such as density, resistivity and sonic logs. In contrast, accurate permeability measurements are mostly obtained from cores, yielding expensive and inherently sparse data.

### **Determining Permeability**

Large-scale, bulk permeabilities needed to model fluid flow across the entire wedge include effects usually not measured in smaller-scale core samples, such as fractures, heterogeneity and anisotropy in deformed sediments [Neuzil, 1994]. Porosity-permeability relationships vary with initial grain size, initial sorting and diagenetic history and compaction [Nelson, 1994]. Even studies which use measured core

permeabilities to derive this relationship make significant assumptions, particularly regarding the effect of varying lithology [e.g. *Saffer and Bekins, 2006*].

In young, unconsolidated formations, such as those drilled at convergent margins, core recovery is biased toward shales and clay-rich formations; cores often wash out in sandy and silty formations and therefore core data provide poor constraints for the porosity-permeability relationship in these formations. Because sandier formations may include zones of enhanced fluid flow, the permeability estimates in these lithologies are important for modeling regional fluid flow. Faulting and deformation introduces fractures, which affect both porosity and permeability but not always in a manner consistent with the porosity-permeability relationship in the rest of the formation. Anomalous areas may exist within a single formation where the porosity-permeability relationship in the faulted intervals is significantly different from that relationship in undeformed portions of the formation. We therefore seek an additional constraint on permeability in sandy and fractured formations.

To complement the core permeability data we seek a continuous log that can serve as a proxy for permeability. Utilizing a downhole log other than neutron porosity or other porosity proxies will minimize error in the fluid flow models by providing an estimate of permeability independent of porosity. The differences between the various resistivity readings, particularly between those with the deepest and shallowest depths of penetration from the borehole into the formation can indicate the degree of borehole fluid invasion into the formation and/or washout in the borehole [*Ellis and Singer, 2007; Rider, 2000; Schlumberger, 2009*]. This degree of invasion, in turn, sheds some light on the relative magnitude of permeability in the formation itself. This approach has been shown effective in hydrocarbon-bearing formations where the contrast between the

invading and *in situ* fluid resistivities is high [e.g. *Cobern and Nuchols*, 1985; *Cozzolino et al.*, 2000; *Salazar et al.*, 2005].

Here we use logging-while-drilling (LWD) *in situ* resistivity data to estimate permeability in boreholes where the resistivity contrast between the borehole fluid and formation fluid is small. We present a hydrologic model of fluid invasion from the borehole wall into the formation and a model of the resistivity tool response to different invasion depths. These models allow us to determine the order of magnitude difference in permeability between different logged silty/sandy zones. We focus on comparing zones inside and outside fault zones due to the role faults may play as permeable conduits for fluids [e.g. *Gulick and Bangs*, 2004].

## **Study Area**

Our study area is the Nankai Trough subduction zone (Figure 1), which is probably the most studied subduction zone in the world [e.g. *Kinoshita et al.*, 2009; *Mikada et al.*, 2005; *Taira et al.*, 1992]. Along this margin, the Philippine Sea Plate subducts beneath the Eurasian Plate at a rate of ~4.1 cm per year and an angle ~15 degrees from trench-perpendicular [*Seno et al.*, 1993]. Despite this minimal obliquity, evidence of strain partitioning is apparent both within the arc [*Tabai et al.*, 2002] and the forearc [*Martin et al.*, 2010]. A subduction megathrust in combination with an associated megasplay fault (Figure 1) accommodates margin perpendicular strain along the plate boundary [*G F Moore et al.*, 2007; *Nishimura and Hashimoto*, 2006; *Park et al.*, 2002].

The Nankai forearc basins, megathrust, megasplay and imbricate thrusts are imaged in seismic data, including two large 3D seismic volumes, one off Cape Muroto and one off the Kii Peninsula (Figure 2.1). Several Ocean Drilling Program (ODP) legs and Integrated Ocean Drilling Program (IODP) expeditions have been undertaken or are

currently planned. ODP Legs 131, 190 and 196 drilled along the Muroto transect [*Mikada et al.*, 2005; *Taira et al.*, 1992]. IODP Expeditions 314, 315, 316, 319 and 322 have drilled along the Kumano transect [*Kinoshita et al.*, 2009; *Saffer et al.*, 2010b; *Saito et al.*, 2010]. Several of these expeditions have produced estimates for permeability.

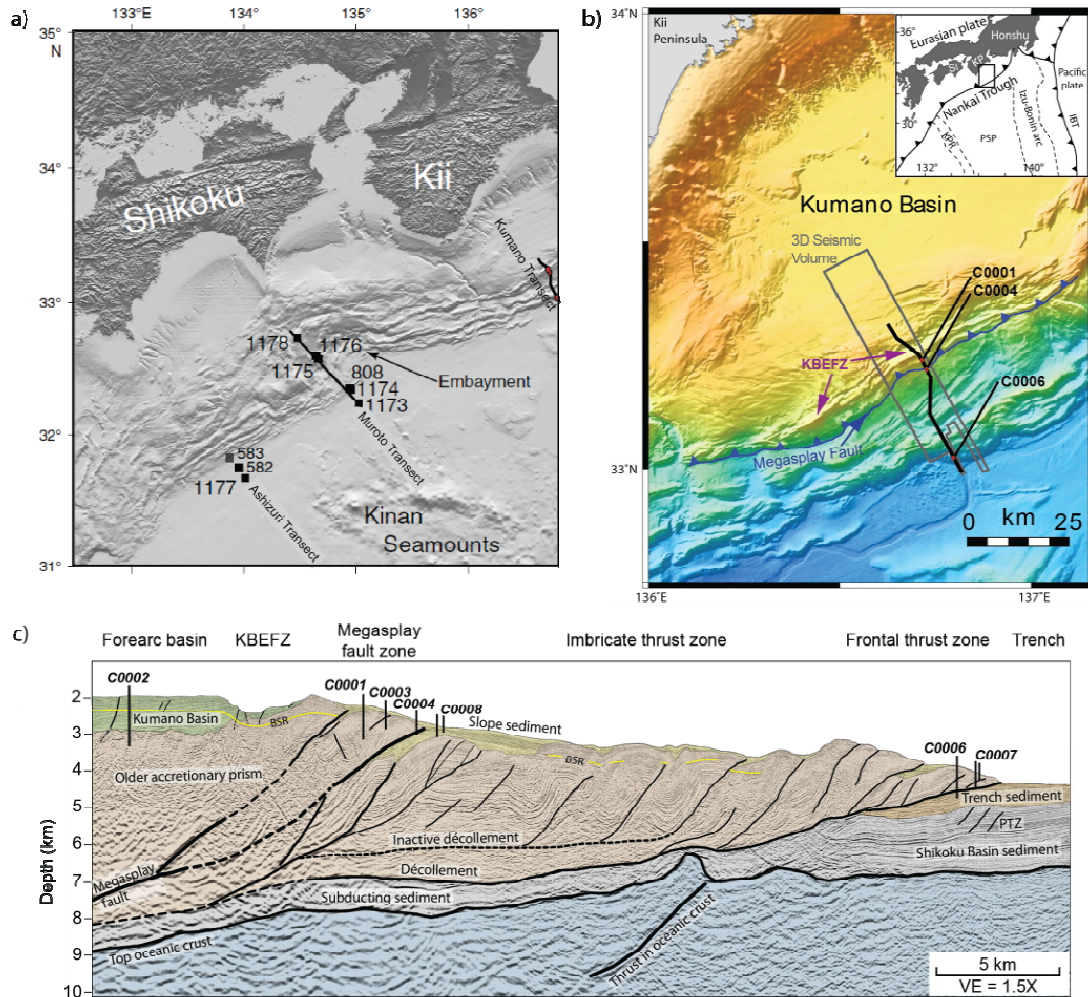


Figure 2.1: Location of study. a) Location of sites drilled during previous ODP Legs 87, 131, 190 and 196 (Ashizuri and Muroto Transects) on a shaded relief map of the Nankai Trough (Hydrographic Department of Japan's topographic data set, 500 m grid interval). Kuma-no Transect sites used in this paper are shown as red circles on composite seismic line at far right. [Modified from *Mikada et al.*, 2005] b) Bathymetry of the Nankai Trough, showing the location of the Kuma-no 3-D seismic volume, megasplay fault and Kuma-no Basin Edge Fault Zone (KBEFZ). Black line is the location of the composite seismic line shown in (c), which passes through or near Sites C0001-C0008. Inset shows the regional setting of the Nankai Trough. PSP = Philippine Sea Plate; KPR = Kyushu-Palau Ridge; IBT = Izu-Bonin Trench; KP = Kii Peninsula, SI = Shikoku Island. [Modified from *G F Moore et al.*, 2007] c) Interpreted composite seismic line extracted from the Kuma-no 3-D seismic volume, with labeled drill sites. Morphotectonic zones are labeled between the two sections. PTZ = protothrust zone, BSR = bottom simulating reflector, VE = vertical exaggeration. [Modified from *G F Moore et al.*, 2009]

## DATA

IODP Expedition 314 occurred in September through November of 2007 [Kinoshita *et al.*, 2008]. Logging while drilling (LWD) data, including gamma ray, sonic velocity and resistivity logs, were acquired at five sites (Figure 2.1c). Density, photoelectric factor (PEF) and neutron porosity logs were also acquired at sites C0001 and C0002. Real time data with lower sampling frequency for these three logs are also available at site C0003, but the full logs were not recovered after loss of the tool string [Kinoshita *et al.*, 2008]. Five different resistivity logs were acquired by LWD, each with a different depth of investigation and sampling interval. As such, the effects of fluid invasion, washouts and variations in composition and bedding structure of the formation differ from log to log. From shallowest to deepest investigation depth these logs are: shallow, medium and deep button resistivities (BS, BM and BD respectively), ring resistivity and resistivity at the bit. To better illustrate the divergence of the shallow and deep button resistivity logs, we calculated a resistivity difference log (BD-BS). An example section of logs with areas of high resistivity difference values is shown in Figure 2.2.

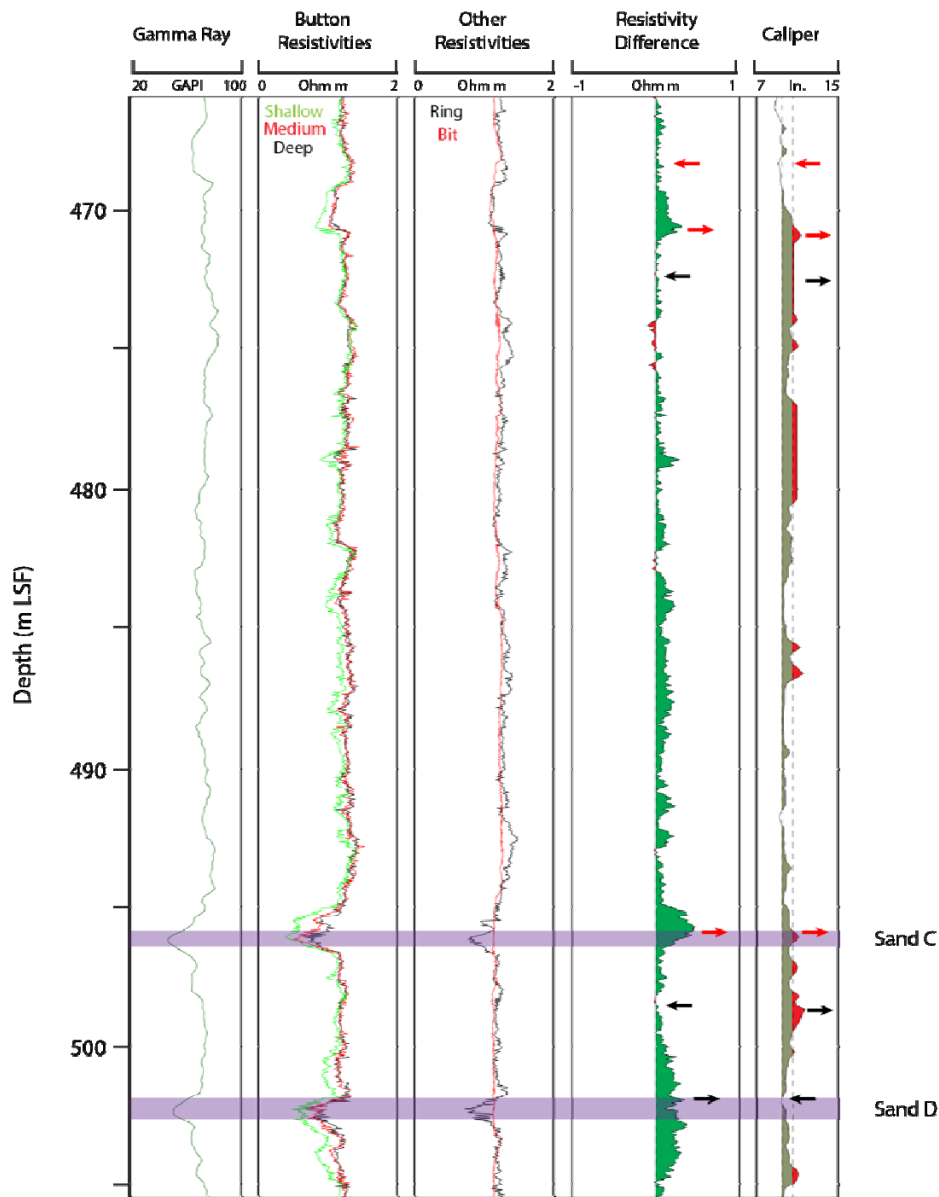


Figure 2.2: Example section of C0001D with resistivity log separation. All resistivity tracks are on a linear scale. The Resistivity Difference log is the calculated difference between shallow and deep button resistivities. The ring resistivity log is similar to the deep button log, but the bit resistivity log has too high of a sampling volume to respond to beds this thin. The caliper log is shaded above 9.5 inches and shaded red above 10.5 inches. Note that sometimes the resistivity difference changes with the caliper log (red arrows) and sometimes it does not (black arrows). The gamma ray log indicates sandy layers at 496 and 502 m LSF (Sands C and D). Sand C is associated with a caliper high and sand D with a caliper low, arguing that borehole width alone does not control the resistivity difference and formation invasion is also occurring.

Such a difference between logs with different depths of investigation can be due either to borehole width or to fluid invasion. Both widening of the borehole and invasion of conductive borehole fluid (seawater) into the formation will cause a resistivity log with shallow depth of penetration to decrease more rapidly than a resistivity log with deeper sampling penetration. The average caliper log (CCAV) indicates the size of the borehole. If the resistivity difference log highs and lows are consistently correlated with the caliper log highs and lows, then the highs in resistivity difference are likely due to washout.

Figure 2.2 shows a section of logs from Expedition 314 where the relationship between caliper and resistivity difference varies. Sometimes washouts (caliper highs) are correlated with more similar resistivity readings and therefore smaller resistivity difference values (example at ~473 m LSF in Figure 2.2). Sometimes washouts are correlated with more divergent resistivity readings and larger resistivity difference values (examples at ~471 and ~496 m LSF in Figure 2.2). This observation implies that differences between the deep and shallow button resistivities are not simply related to washouts, but rather respond to variable fluid invasion as well. In order to focus on possible fluid invasion effects, we focus on points where the caliper is not particularly high (<10.5 in). For example, the average caliper log (CCAV) is at a local minimum in the lowermost sand in Figure 2.2 (Sand D, Hole C0001D), indicating that the difference between the shallow and deep resistivity logs is not due to washout in this sandier interval. Further discussion of the sandy intervals selected for analysis can be found in Sample Selection and Observations section below.

The largest deep-shallow resistivity differences are correlated with low values of the gamma ray log, indicating sandier lithologies. Sands and silts would be expected to have higher porosities and permeabilities than clay-rich units. Indeed, the areas with the highest gamma ray log values, those which are the least sandy, show little and frequently

no separation between the shallow and deep resistivity logs (as in the top portion of Figure 2.2). We therefore use only the sandiest lithologies in our analysis, as these are the layers most likely to allow sufficient invasion by borehole fluids for that phenomenon to be distinguishable from washouts and other effects. For quantitative analysis we pick ten sands from discrete depths (see Sample Selection and Observations section), some inside and some located away from fault zones.

## MODEL

We present a single phase flow model to describe the invasion of the borehole fluid into the bounding formation as a function of time and the driving pressure in the annulus. We then use this model to examine whether resistivity differences observed during drilling can provide information about permeability. The single phase flow assumption is appropriate because we are not examining hydrocarbon-bearing formations and the drilling fluid was seawater. Advection and diffusion equations describe single phase transport, but we neglect the diffusion of salt between the two fluids because advection dominates transport for short time scales (minutes to tens of minutes). The small magnitude of diffusive transport can be illustrated with a calculation of characteristic length,  $L = \sqrt{tD}$ , where  $t$  is the time-scale of interest and  $D$  is the diffusivity of the solute. For a time scale of one hour (3600 s) I use the diffusivity of the chloride ion in water ( $2.03 \times 10^{-5} \text{ cm}^2/\text{s}$ ) to get a characteristic length of 0.270 cm. This length is small compared to the distances of invasion we calculate from the model described below for purely advective transport. See Appendix A for further discussion of the relative magnitudes of advection and diffusion.

To obtain distances of invasion from the resistivity logs, we utilize a model of the resistivity tool response to fluid invasion developed by The University of Texas at

Austin, Research Consortium on Formation Evaluation. We assume a borehole fluid of constant salinity (seawater) displaces a formation fluid of lower salinity. For a given sand, the tool response model allows us to estimate an invasion distance,  $di$ , given the difference between deep and shallow resistivity logs. Our formation invasion model then allows us to estimate that sand's permeability from  $di$  and the associated time after bit (TAB), which is the time elapsed between drill-bit penetration of the formation at a given depth and measurement by the resistivity tool at that same depth.

### Formation Invasion Model

Consider a borehole of radius  $a$  (Figure 2.3a). Assume the surrounding formation is homogenous and isotropic.  $P$  is the pore pressure and  $P^*$  is the pore pressure in excess of hydrostatic,  $P^h$ , ( $P = P^h + P^*$ ). When the well bore is drilled, the annular pressure is greater than the formation pressure ( $P_f$ ) by the amount  $\Delta P$ . The evolution of pressure in the formation caused by this change in pressure at the well bore is described by the consolidation equation:

$$\frac{dP^*}{dt} = C_v \nabla^2 P^* \quad \{1\}$$

where  $C_v = k/m_v \mu$  is the coefficient of consolidation ( $k$  is permeability,  $m_v$  is the coefficient of volume compressibility and  $\mu$  is the viscosity of water).

In cylindrical coordinates, assuming radial symmetry, {1} becomes

$$\frac{dP^*}{dt} = C_v \left( \frac{\partial^2 P^*}{\partial r^2} + \frac{1}{r} \frac{\partial P^*}{\partial r} \right) \quad \{2\}$$

Because hydrostatic pressure is constant in both time and the radial direction, the derivatives of the excess pore pressure are equal to the derivatives of the total pore pressure (within a horizontal plane), allowing us to write [Saito *et al.*] in terms of  $P$  instead of  $P^*$ :

$$\frac{dP}{dt} = C_v \left( \frac{\partial^2 P}{\partial r^2} + \frac{1}{r} \frac{\partial P}{\partial r} \right)$$

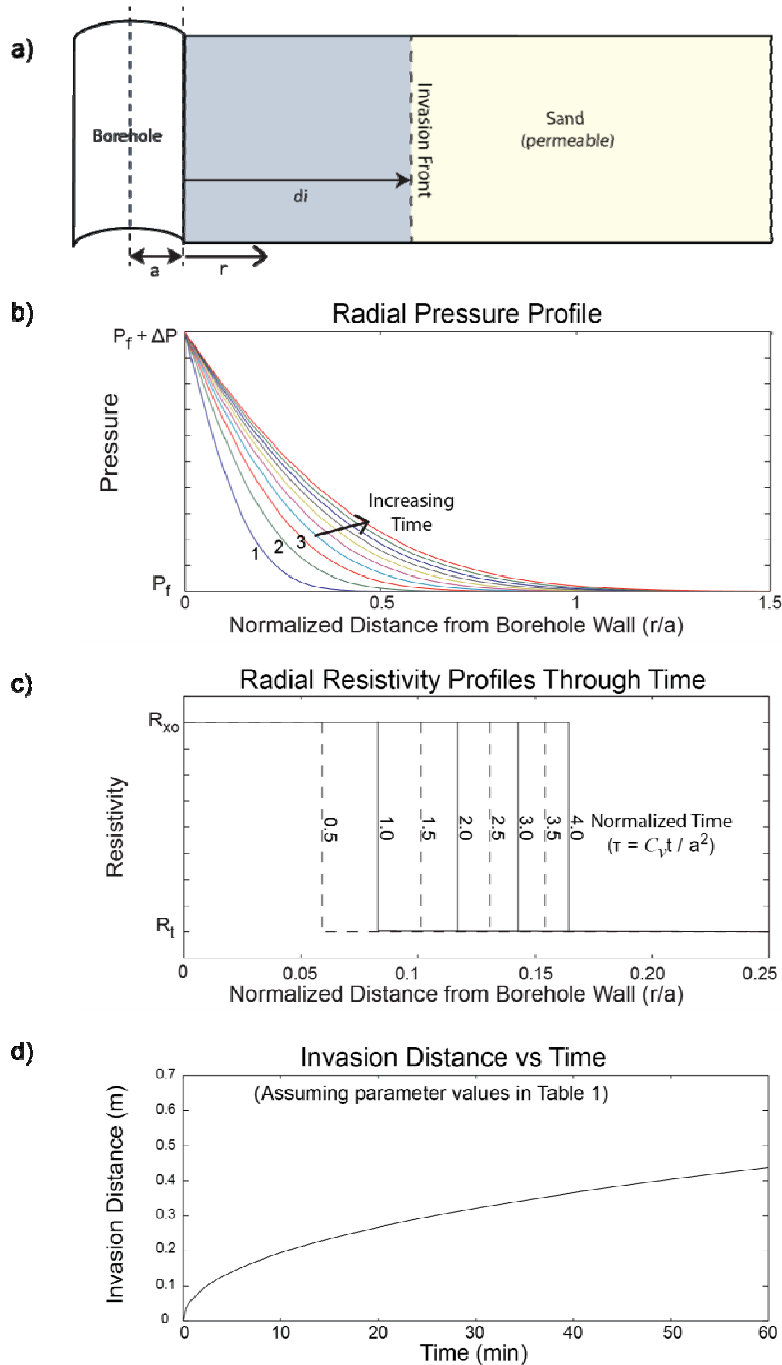


Figure 2.3: Radial formation invasion model. a) Schematic borehole diagram. b) Normalized radial pressure profile. Numbers on curves are values of normalized time,  $\tau = C_v t / a^2$ . c) Resistivity profile through time. Numbers on curves are values of  $\tau = C_v t / a^2$ . d) Distance of invasion as a function of time assuming parameter values in Table 2.1.

We assume the area at  $r>a$  is initially at formation pressure  $P_f$  and the surface at  $r=a$  is at a constant pressure  $P_f + \Delta P$ . Using the solution to the diffusion equation in a region bounded internally by a circular cylinder of radius  $a$  [Carslaw and Jaeger, 1959], we solve for  $P$  in the form of an inverse Laplace Transform:

$$P = P_f + \frac{\Delta P}{2\pi i} \int_{\gamma-i\infty}^{\gamma+i\infty} e^{\sigma t} \frac{K_0\left(\frac{\sigma}{C_v} r\right)}{K_0\left(\frac{\sigma}{C_v} a\right) \sigma} d\sigma \quad \{3\}$$

where  $\sigma$  is the Laplace variable and  $K_0$  is the first order modified Bessel function of the second kind. For small values of time, we utilize the asymptotic series expansion of the Bessel functions and solve the integral.

$$\begin{aligned} P = P_f + \frac{\Delta P \sqrt{a}}{\sqrt{r}} \operatorname{erfc}\left(\frac{r-a}{2\sqrt{C_v t}}\right) \\ + \frac{\Delta P (r-a) \sqrt{C_v t}}{4\sqrt{a r^3}} i \operatorname{erfc}\left(\frac{r-a}{2\sqrt{C_v t}}\right) \\ + \frac{\Delta P (9a^2 - 2ar - 7r^2) C_v t}{32\sqrt{a^3 r^5}} i^2 \operatorname{erfc}\left(\frac{r-a}{2\sqrt{C_v t}}\right) \\ + \dots \end{aligned} \quad \{4\}$$

We include only the first three terms because these dominate the solution for short time intervals. The resulting pressure profile through time is shown in Figure 2.3b.

The advection velocity in the pores depends on the pressure gradient according to Darcy's Law for flux ( $\vec{q}$ ), the volumetric flow rate ( $Q$ ) over an area  $A$ :

$$\vec{q} = \frac{Q}{A} = -\frac{k}{\mu} \nabla P = \vec{v} \varphi \quad \{5\}$$

where  $\varphi$  is porosity and  $\vec{v}$  is the pore velocity of the fluid. In cylindrical coordinates the gradient operator is  $\nabla = \hat{r} \frac{\partial}{\partial r} + \hat{\theta} \frac{1}{r} \frac{\partial}{\partial \theta} + \hat{z} \frac{\partial}{\partial z}$ . Because we are working in

the radial direction we solve for the radial component of  $\vec{v}$ , and need only the radial (first) term of the gradient. Thus we get the ordinary differential equation:

$$|\vec{v}_r| = \frac{dr}{dt} = -\frac{k}{\mu\phi} \frac{dP}{dr} \quad \{6\}$$

Using the three explicit terms in equation {4} for  $P$ , we solve equation {6} numerically in Matlab (code shown in Appendix B). Specifically, we use a particle-tracking method, which integrates the differential equation over time for each time step using the value of  $r$  from the previous time step as the initial condition. For example, we integrate from 0 to  $t_1$  with the initial condition that the salinity front is at the borehole wall ( $r(t=0) = a$ ) to get  $r_1$ , the position of the salinity front at time  $t_1$ . Then we integrate from  $t_1$  to  $t_2$  with the initial condition that  $r = r_1$  to obtain a value for  $r_2$ , and so on. By solving for values of  $r$  over a given range of  $t$ , we can plot the position of the salinity front through time (Figure 2.3c).

Appendix C shows a comparison of the particle tracking solution to a solution based on flux at the borehole wall. The difference between these two solutions is the volume of compression the driving pressure induces in the formation itself, which increases with  $m_v$ . Because volume compressibility is non-zero, we prefer the particle tracking solution that accounts for this compression over the boundary flux solution that does not.

### **Invasion Model Discussion**

Figure 2.3b and 2.3c present dimensionless plots of the radial pressure and resistivity profiles, respectively. To apply our model to samples from the Nankai Trough, we must pick reasonable values for the governing parameters (Table 2.1). Figure 2.3d shows an example plot of invasion distance through time assuming  $k = 10^{-19} \text{ m}^2$  ( $10^{-4}$

mD). By plotting separate curves for several values of  $k$ , we can produce a plot on which invasion distance and TAB in a particular sand can be used to determine the permeability of that sand (see Model Application section in Results and Discussion). Such plots assume constant values for the other model parameters, several of which we discuss below.

Table 2.1: Invasion Model Parameter Values

Symbol	Description	Value(s)	Units	Notes
$C_v$	Coefficient of consolidation	$1 \times 10^{-6}$	$\text{m}^2/\text{s}$	
$k$	Permeability	$10^{-15} - 10^{-11}$	$\text{m}/\text{s}$	
$\gamma_w$	Unit weight of sea water	1.024	$\text{kN}/\text{m}^3$	
$m_v$	Coefficient of volume compressibility	$10^{-6} - 10^{-2}$	$\text{kPa}^{-1}$	Calculated from $k$ , $C_v$ and $\mu$ .
$a$	Radius of borehole	0.2	$\text{m}$	~ 8 inches
$\mu$	Viscosity of water	$1.08 \times 10^{-3}$	$\text{Pa}\cdot\text{s}$	At 20° C
$A$	Area	$2\pi r$		Cylinder with unit height
$\Delta P$	Difference between borehole and formation pressures	500	$\text{kPa}$	

With decreasing porosity during consolidation, both  $k$  and  $m_v$  decrease rapidly, but the ratio  $k/m_v$  (and thus  $C_v$ ) is much less variable [Terzaghi and Peck, 1967]. We therefore pick a value for the coefficient of consolidation and hold it constant while varying permeability. This action is the same as varying  $m_v$  with permeability. Accurate values of  $C_v$  in uncemented silts and sands at depth are difficult to constrain in a laboratory setting due to the poor core recovery in these strata.  $C_v$  has been reported at 2

$\times 10^{-7} \text{ m}^2/\text{s}$  in Ursa Basin siltstones with ~30% clay [Long *et al.*, 2008]. Data Reports from Expeditions 314, 315 and 316 report values of  $C_v$  in shallow (<100 meters below the seafloor as defined by LWD data (m LSF)) samples at  $10^{-7}$  to  $10^{-6} \text{ m}^2$  [Saffer *et al.*, 2010a] and  $10^{-8}$  to  $10^{-5} \text{ m}^2$  [Dugan and Daigle, 2010]. Since our analysis focuses on silty to sandy layers, which would be expected to have an even higher coefficient of consolidation, we use a value of  $C_v = 5 \times 10^{-6}$  in our model.

Another important yet poorly constrained variable is  $\Delta P$ . Because equation {6} depends only on the derivative of  $P^*$ , the initial formation pressure,  $P_f$ , has no direct effect on our modeled speed of invasion (Figure 3). Instead,  $\frac{dP^*}{dr}$ , and therefore  $|\overline{v_r}|$ , are proportional to  $\Delta P$ . Unfortunately, we have no direct measure of  $\Delta P$ . The measured annular pressure (APRS) log values are actually lower than expected hydrostatic pressure in portions of our boreholes and in places increase at a rate slower than the hydrostat (see Appendix D for additional discussion). For the purposes of our model, we assume  $\Delta P$  is ~500 kPa, which is near 10% of the difference between the hydrostat and lithostat at 500m below the seafloor.

## **Tool Response**

Resistivity measurements were made using the Schlumberger geoVISION tool, which is based on resistivity-at-the-bit (RAB) technology [described by Allen *et al.*, 1994]. Each button sensor on the geoVISION tool is associated with a different depth of penetration. Therefore, fluid invasion will affect each reading to a different degree [Allen *et al.*, 1994; Rider, 2000]. The shallow button resistivity will be most influenced by invasion, and may in some cases read nothing but invaded formation. The deep button resistivity, in contrast, should not be affected significantly by invasion on the time scales

relevant to LWD operations (minutes to tens of minutes). The difference between the deep and shallow button resistivities therefore relies heavily on the tool response to the formation resistivity [Allen *et al.*, 1994; Ellis and Singer, 2007; Rider, 2000].

We model the resistivity tool response with the UTAPWeLS software developed by The University of Texas at Austin, Research Consortium on Formation Evaluation. The geoVISION tool response model is currently unavailable, but should be similar to the Schlumberger High-Resolution Laterolog Array (HRLA) tool response. Both tools use an active focusing technique to resolve thin beds [Allen *et al.*, 1994] and have standard borehole effect corrections [Schlumberger, 2009]. Instead of the three buttons present on the geoVISION tool, the HRLA tool uses six focusing modes to yield resistivity measurements at five depths of penetration (R1-5 in Figure 2.4) and within the borehole [Schlumberger, 2000]. Due to the similarities in focusing technique, advertised depths of penetration and borehole effect correction charts, the shape of the HRLA log responses to invasion should be similar to that of the geoVISION log responses.

The tool response model was run on a step-function invasion profile (Figure 2.4a) with invaded and virgin zone resistivities adjusted for each set of comparable sands (Table 2.2). The assumed sand bed in the model was 10 m thick, sufficiently thick to minimize shoulder effects from the surrounding shale beds. Sand beds in our boreholes are generally less than 10 m thick, but Schlumberger corrections should account somewhat for thin bed effects and shoulder effects in the data [Schlumberger, 2000; 2009].

Values of resistivity for the invaded zone ( $R_{xo}$ ) and uninvaded zone ( $R_t$ ) in the model were chosen based on the maximum range of shallow and deep resistivity values measured in the sands at each site. In Table 2.2, the Ideal Value of formation water resistivity ( $R_w$ ) corresponds to a salinity of ~31000 ppm, which is consistent with the

salinities measured in interstitial waters for Site C0001 between 100 and 400 m LSF. The Ideal Value for the invading fluid ( $R_{mf}$ ) corresponds to a salinity of 35000 ppm, roughly that of seawater. Calculation of porosity based on Archie's Law yields values near 36% for the uninvaded zone. The same calculation in the invaded zone yields porosities over 50%. This discrepancy is likely due to standoff in excess of that assumed in the borehole corrections. Corrections for standoff and thin bed effects are included in the environmental corrections automatically applied to the data by Schlumberger. These corrections assume a borehole width. Where our borehole is wider than the assumed value, a section of borehole (effectively 100% porosity) is included with the invaded zone in our shallowest resistivity measurement. Calculation of porosity from resistivity using Archie's law will therefore result in an overestimation of porosity in these intervals.

An example tool response plot is shown in Figure 2.4b. The range of penetration depths for the HRLA tool are similar to the range of depths for the geoVision tool, making R1 and R5 in Figure 2.4b correspond to our shallow and deep button resistivity logs. For silty/sandy intervals with comparable gamma ray log values, caliper log values and fluid contrasts, the separation between the deep and shallow resistivity logs is used to assign a depth of invasion ( $di$ ) to each sample (Table 2.3).

Table 2.2: Tool Response Model Parameters

		Tool Response Model			Ideal values		Archie Porosity (using Ideal Resistivities, $a = S_w = 1$ and $m = 1.95$ )	
Hole	Samples	Tool Standoff (m)	$R_t$ ( $\Omega m$ )	$R_{xo}$ ( $\Omega m$ )	$R_w$ ( $\Omega m$ )	$R_{mf}$ ( $\Omega m$ )	Formation (using $R_f$ )	Invaded Zone (using $R_{mf}$ )
C0001D	Faults A,B, Sands A,B, C, D	0.1	1.5	0.6	0.21	0.19	0.365	0.554
C0004A	Fault C, Sands E, F,G	0.1	1.5	0.5	0.21	0.19	0.364	0.609

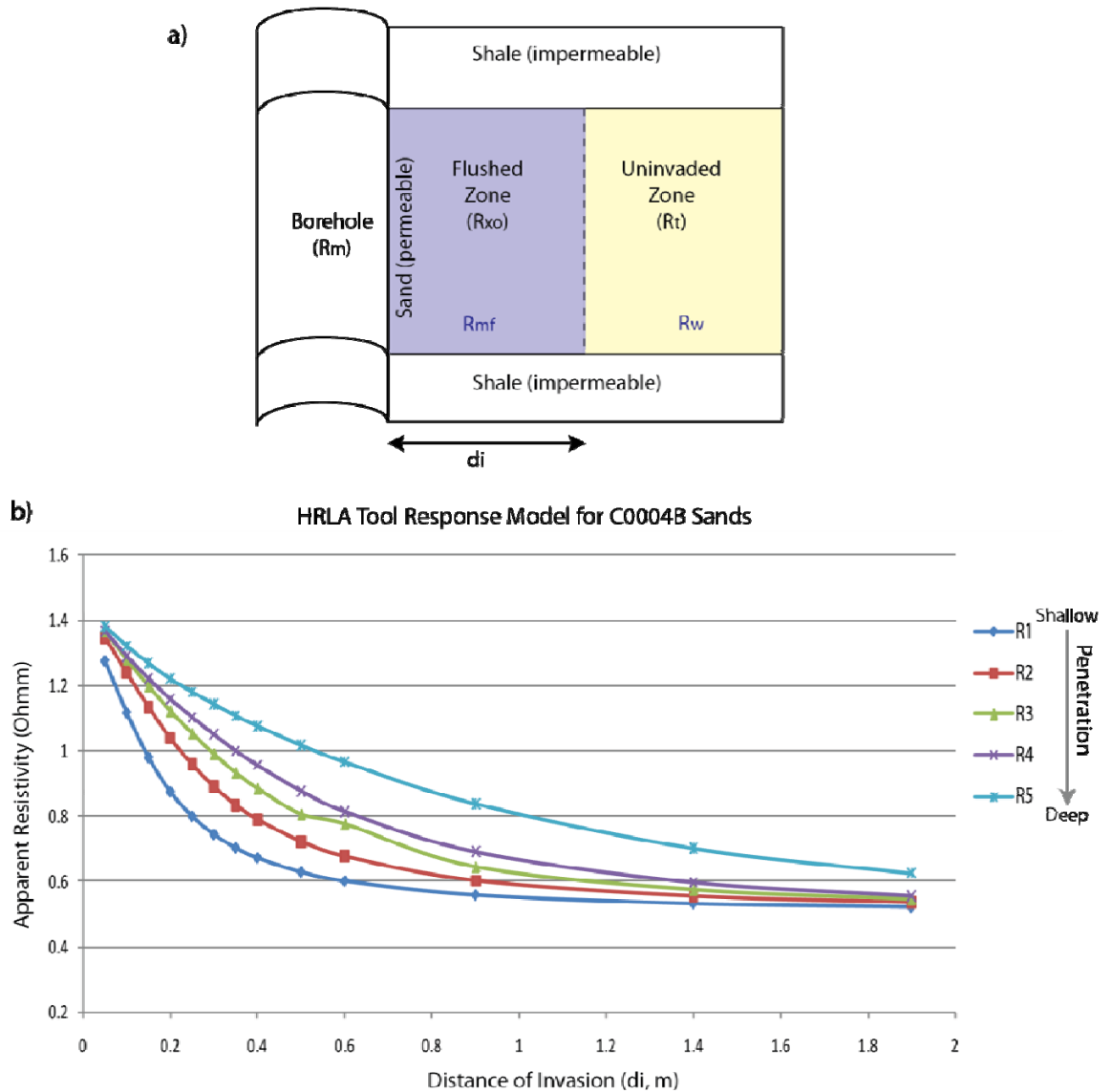


Figure 2.4: Tool response model for the Schlumberger High-Resolution Laterolog Array (HRLA) tool. a) Input scenario.  $R_w$  = Formation water resistivity and  $R_{mf}$  = mud filtrate resistivity, which is assumed to be near  $R_m$ , that of seawater.  $R_{xo}$  and  $R_t$  are the resistivities of the fully invaded and uninvaded formation respectively. b) Tool response in the form of apparent resistivity measured by each focusing mode (R1-5 where R1 is the mode with the shallowest depth of investigation) as a function of distance of invasion ( $d_i$ ).

Table 2.3: Samples used in quantitative analysis

Sample	Hole	Depth (m)	Log Values								Calculated Values		
			Gamma Ray (GAPI)	CCAV (In)	BD ( $\Omega$ m)	BS ( $\Omega$ m)	Sonic ( $\mu$ s/ft)	APRS (kPA)	Temp. ( $^{\circ}$ C)	TAB (min.)	BD - BS ( $\Omega$ m)	Modeled <i>di</i> (m)	Modeled <i>k</i> (mD)
Fault A	C0001D	344	59.3	10.5	1.072	0.816	161.08	25173	17.3	39.87	0.257	0.1535	20
Fault B	C0001D	588	44.8	--	0.810	0.419	169.77	34335	28.0	19.10	0.391	0.3861	80,000
Fault C	C0004B	173	60.6	10.5	1.126	0.713	163.01	27565	10.2	25.25	0.413	0.3736	10,000
Sand A	C0001D	373	57.8	10.2	1.297	1.290	160.36	26016	18.5	7.57	0.007	0.0112	1
Sand B	C0001D	435	35.0	11.9	0.660	0.431	171.82	26007	21.3	5.93	0.229	0.1301	320
Sand C	C0001D	496	49.7	10.9	0.836	0.413	172.68	27245	23.9	44.06	0.423	0.3861	1,000
Sand D	C0001D	502	51.2	9.8	0.857	0.622	158.52	29047	24.2	12.19	0.235	0.1348	70
Sand E	C0004B	134	61.8	10.0	1.285	1.006	163.35	27180	8.4	24.78	0.280	0.1451	30
Sand F	C0004B	161	64.7	10.4	1.356	1.226	160.76	27423	9.7	7.17	0.130	0.0615	12
Sand G	C0004B	166	59.2	11.1	1.268	0.980	166.44	27460	9.9	6.92	0.288	0.1512	400

CCAV, Average Caliper Log; BD, Deep Button Resistivity; BS, Shallow Button Resistivity; APRS, Annular Pressure-While-Drilling Log; TAB, Time After Bit; BD-BS, Difference between the Deep and Shallow Button Resistivity Logs; *di*, Invasion Distance (modeled); *k*, Permeability (modeled).

## **SAMPLE SELECTION AND OBSERVATIONS**

We pick discrete samples from the LWD data at Sites C0001 and C0004 (Table 2.3, locations shown in Figure 2.1b,c) for quantitative analysis. Site C0002 is in the Kumano Basin and would be a good site for invasion analysis in undisturbed turbidite sequences, but the presence of a Bottom Simulating Reflector (BSR) with likelihood of free gas below it and gas hydrates above it indicates the presence of significant non-water phases in the pore space. Our model is a single-phase water model and would be suspect in these sediments. Only real-time data exists for site C0003, where the bottom-hole-assembly was lost, and this real-time data does not include the shallow or medium button resistivities or the caliper log. Thus we cannot apply our method at this site. No density, neutron or PEF data were acquired for sites after C0003, but at Site C0004 the resistivity, gamma ray and caliper logs are sufficient for our analysis. We qualitatively discuss Site C0006 as an example of a borehole where our method will not work due to the nature of the formation rather than the quality of the logs. The correlation between caliper and resistivity difference is strong at this site, as is the correlation between caliper and gamma ray log values, probably both due to the unconsolidated nature of the sandy lithologies.

### **C0001D**

Site C0001 is located at the seaward edge of the outer arc high, where branches of the megasplay fault system approach the surface [*Expedition 314 Scientists*, 2009b] (Figure 2.1c). Hole C0001D reached 974 m LSF (Figure 2.5) and resistivity and gamma ray data exist for the entire hole. However, the adnVISION tool failed below 510 m LSF, making caliper, density, neutron and several data quality logs unavailable below that depth. Without a caliper log determining whether a sand is washed out is difficult. Above

510m LSF, low gamma ray log values are only sometimes associated with higher caliper values, implying that only some sandier layers are associated with washouts. Also, these siltier/sandier layers are only in some cases associated with large differences between the shallow and deep resistivity logs, implying that only some layers are invaded enough to cause this log separation.

Shipboard scientists interpreted the trend of the annular pressure while drilling (APRS) log as normal (hydrostatic) as it increases with depth until ~470 m LSF [Kinoshita *et al.*, 2008], despite sections of the log below the hydrostat (See Appendix D). The rig floor pumping rate is also lower above ~410 m LSF and increases below that depth. Based on these logs, we find that sands from above 470 m are not ideal for our analysis because the borehole pressure is too close to the formation pressure to force fluid invasion rapid enough to be recorded by LWD (short TAB) data. Despite this lower pressure contrast in the shallower portion of Hole C0001D, one sample at 344 m LSF (Fault A in Table 2.3, Figure 2.5), within a fault zone imaged in the 3D seismic volume, shows some separation between resistivity logs. We choose two other sands (Sands A and B in Figure 2.5b) not associated with a fault and located within the zone of pressure nearer hydrostatic to compare with Fault A. Sand A, at 373 m LSF, has nearly the same caliper response as Fault A but shows almost no resistivity log separation. Sand B, at 435 m LSF, has a significantly lower gamma ray value and a higher caliper value than Fault A.

Between 470 and 510 m LSF only two low gamma ray log minimums are found (Sands C and D in Figure 2.2). The seismic images show a fault near 588 m LSF that is also coincident with a sand (Fault B, Figure 5), but several logs, including the caliper, are missing at this depth. Extremely high TAB values and higher values of sonic slowness (lower velocities) characterize this portion of the hole and, in fact, all of logging Unit

IIIA (Figure 2.5a). Despite the lack of a measured caliper, the sand at Fault B is less likely to have been washed out than other sandy units in this area because of a moderate TAB value and a sonic log value near the compaction trend found in the logging units above and below logging Unit IIIA. In zones where borehole washout has occurred, as evidenced by areas of relatively higher caliper log values, the sonic slowness usually increases because of the additional fluid between the tool and the formation. Fault B can therefore be compared with Sands C and D.

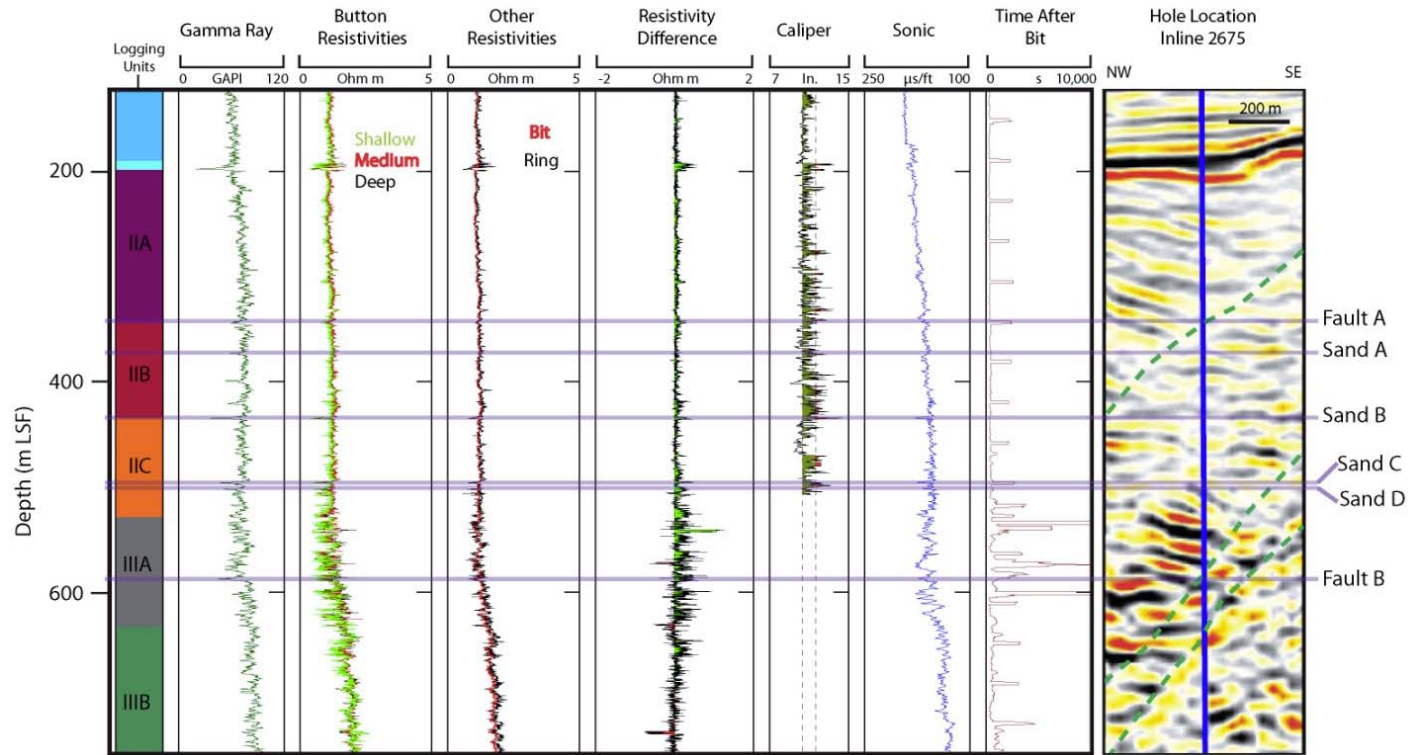


Figure 2.5a: C0001D summary log diagram. Logging units defined by shipboard scientists. Gamma ray log used to identify sandy lithologies. All resistivities are plotted on a linear scale. Button resistivities are the average of the azimuthal resistivity values from any given depth for each button sensor. Ring and Bit resistivities have higher sampling volumes than the button sensors. Resistivity Difference is the deep button resistivity minus the shallow button resistivity, with positive values shaded in green. The caliper log is shown with a baseline of 9.5 inches and a reference line at 10.5 inches. Calipers greater than 9.5 inches are shaded and calipers greater than 10.5 inches are colored red. Sonic log is given in units of slowness. Time After Bit (TAB) log shows regular increases where stand changes occurred and less regular anomalies where drilling operations encountered difficulties, generally in faulted zones. Seismic section from the Kumano 3D seismic volume showing interpreted faults. Samples chosen for analysis marked with purple lines and labeled at right. [Modified from *Expedition 314 Scientists*, 2009b]

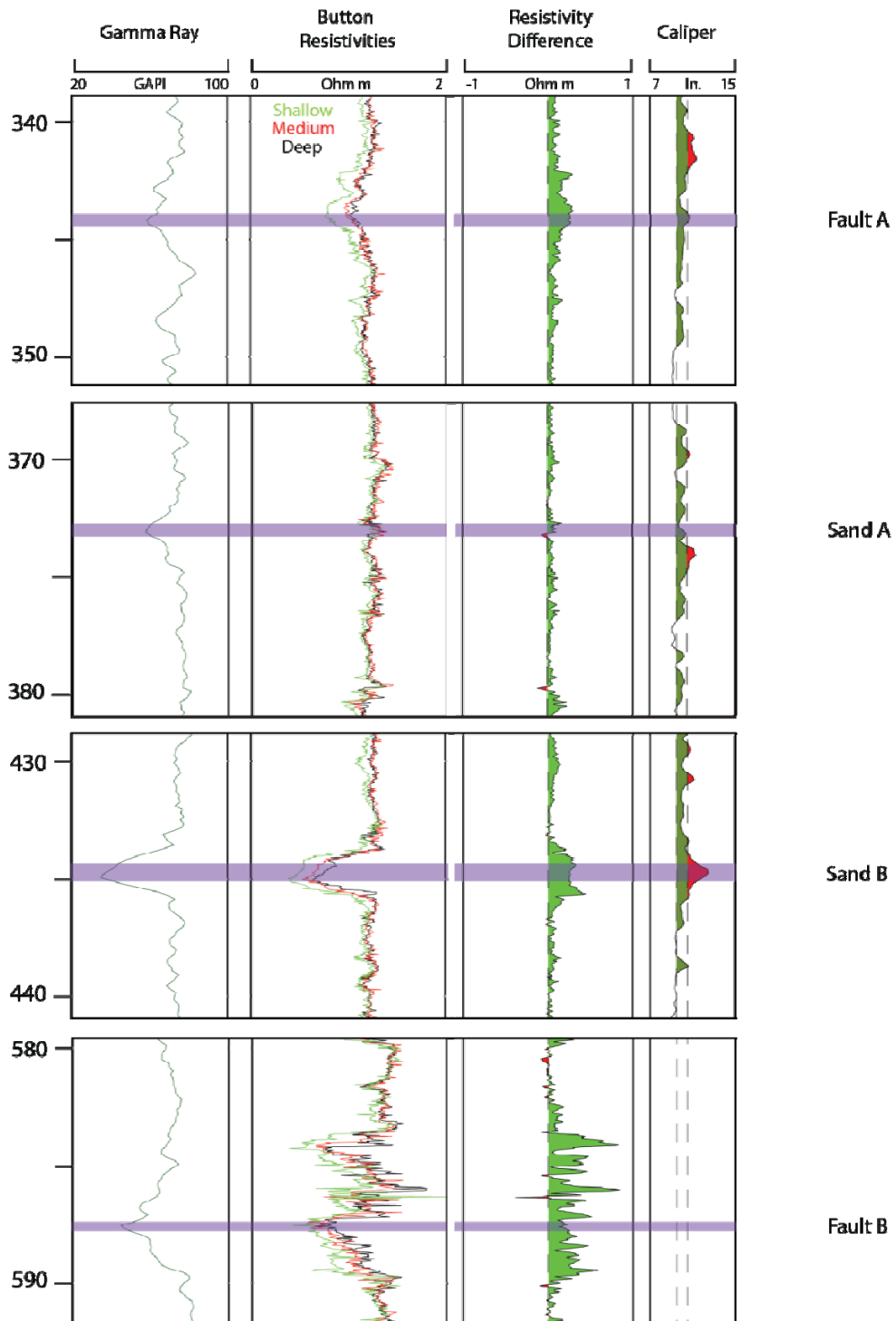


Figure 2.5b: Expanded sections of gamma ray, resistivity and caliper logs around each of the samples highlighted in (a).

## **C0004B**

Site C0004 is located along strike and slightly seaward from Site C0001 [Expedition 314 Scientists, 2009a]. The 400 m deep hole C0004B penetrates slope sediments, the thrust wedge in the hanging wall of the megasplay system and across the shallow portion of a branch of the megasplay into older slope sediments that are now part of the footwall (Figure 2.6). Several faults appear within the thrust wedge section below ~170 m in the seismic data and a strong, fault-related reflector separates the thrust wedge from the underlying slope sediments at ~300m.

Throughout Hole C0004B, the deep resistivity log values are consistently higher than the shallow resistivity log values. The magnitude of the difference between these logs varies between logging units. In the shaly parts of logging Unit I, shallow and deep resistivity values are nearly equal. The difference between the two logs increases through logging Subunit IIA despite gamma ray values which indicate a shale fraction similar to that in Unit I. The resistivity difference remains high throughout logging Unit II, although more variability is noted in the lower portion of Subunit IID. In logging Unit III, the resistivity difference is less than in Unit II, but is still distinctly measureable.

Picking sands to study in this hole proved difficult, as gamma ray values less than 60 GAPI were rarely recorded. We confine sample selection to local minima below 65 GAPI, with the caveat that these 'sands' likely have some clay fraction. In designating samples as Fault or Sand, we rely on the seismic images and onboard structure analysis (Figure 6). Onboard scientists identified eight fractured zones in the resistivity images from Hole C0004B [Expedition 314 Scientists, 2009a]. These zones were characterized by "intense development of fractures (mostly conductive) and wide breakouts and were classified as "major" or "minor" based on their intensity of deformation and

conductivity.” We compared these fractured zones to the formation above and below each zone.

The first significant observation is that several of the zones identified correspond to dramatic increases in the TAB, associated with stand changes. An increase in borehole breakout size would be expected with more time between bit penetration and tool measurement. Also, additional time allows for more invasion into the formation, making areas with long TAB appear more conductive than the formation above or below, particularly in the shallowest button resistivity logs. Because the effects of increased TAB are essentially similar to the parameters used to identify fractured zones, those identified zones with consistently high TAB are not conclusively anomalously fractured (Figure 2.7). Only those fracture zones identified by onboard scientists which do not coincide with zones of high TAB can be conclusively attributed to formation properties, rather than drilling anomalies. We use these zones as well as faults identified on seismic images to classify areas as fractured or not and to choose one sand within a fault zone and three sands not associated with a fault zone for analysis and comparison (Figure 2.6).

The areas of C0004B with increased TAB also show increased separation between the deep and shallow button resistivity logs, consistent with an expected increase in invasion with time since drilling. This correspondence implies that the difference between the shallow and deep resistivity logs is a good proxy for formation invasion.

Three gamma ray minima occur between 160 and 175 m LSF (Figure 2.6a,b). The deepest of these (Fault C) is within both a high TAB section and a fault zone in the seismic image (Figure 2.6). The shallowest (Sand F) has a caliper value similar to that of Fault C. The middle gamma ray minimum (166 m LSF in Figure 2.6b) is included as Sand G to show the effect of higher caliper. Sand E at 134 m LSF is included to expand the depth range of the samples and show the effect of TAB alone (Table 2.3).

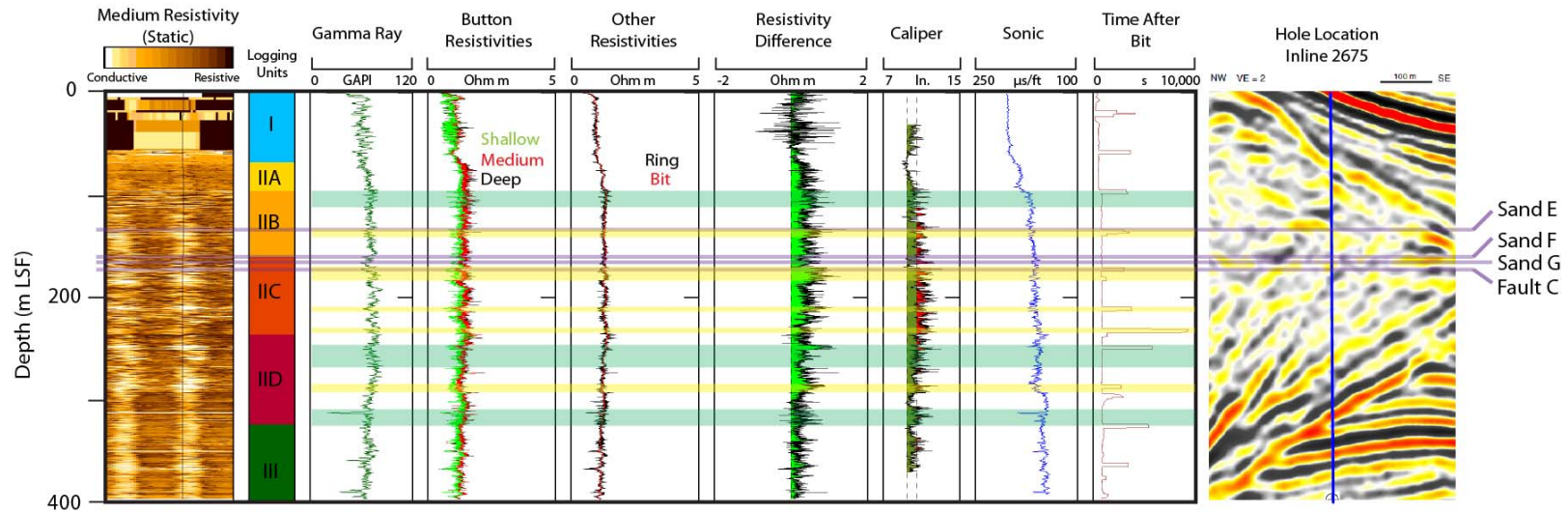


Figure 2.6a: C0004B summary log diagram. See Figure 2.4 for panel descriptions. Samples chosen for analysis marked with purple lines and labeled at right. Fracture zones identified by onboard scientists are highlighted. Yellow zones correspond to TAB anomalies. Green zones are not solely related to TAB anomalies and likely fractured. [Modified from *Expedition 314 Scientists*, 2009a]

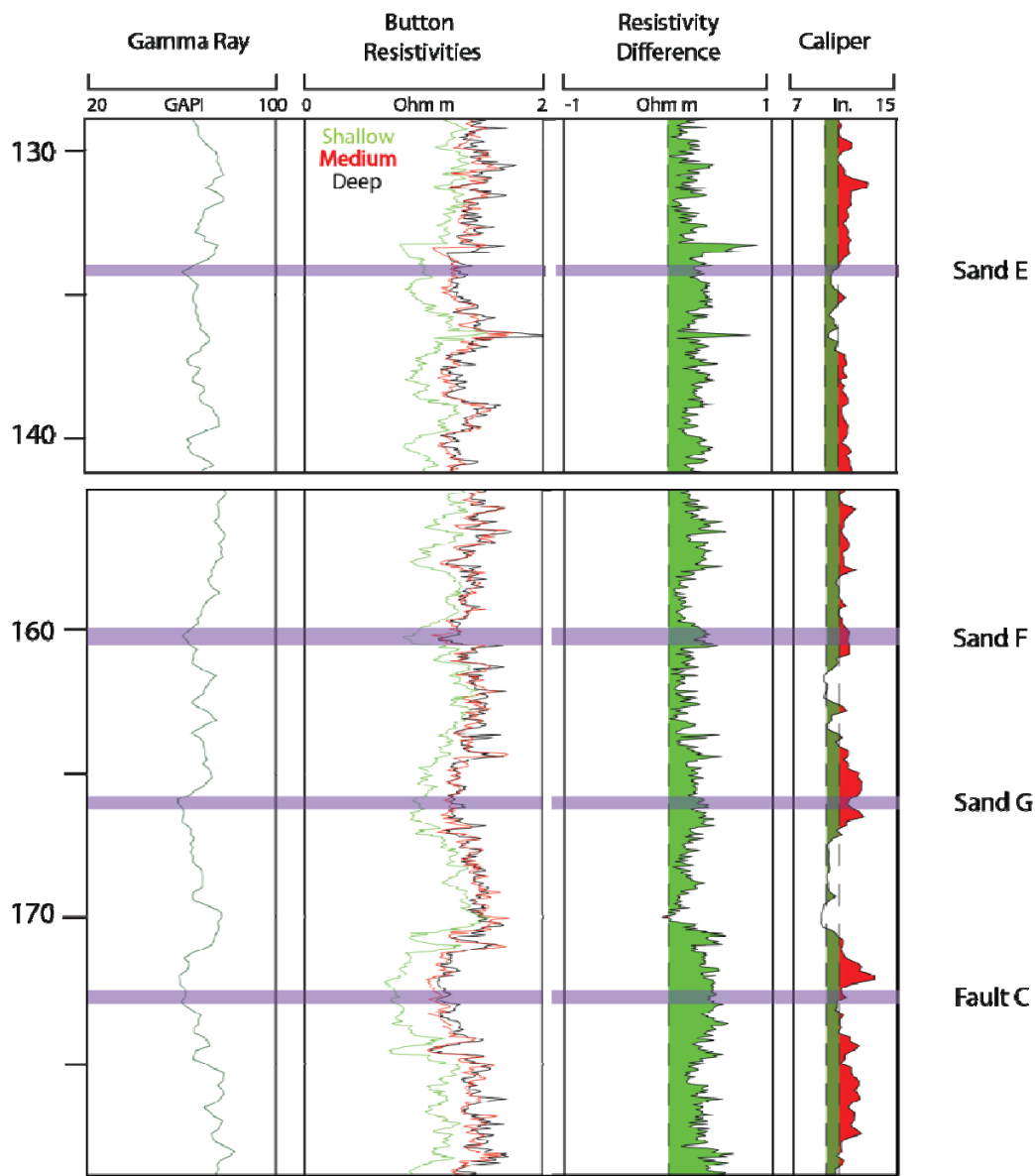


Figure 2.6b: Expanded sections of gamma ray, resistivity and caliper logs around each of the samples marked with purple in (a).

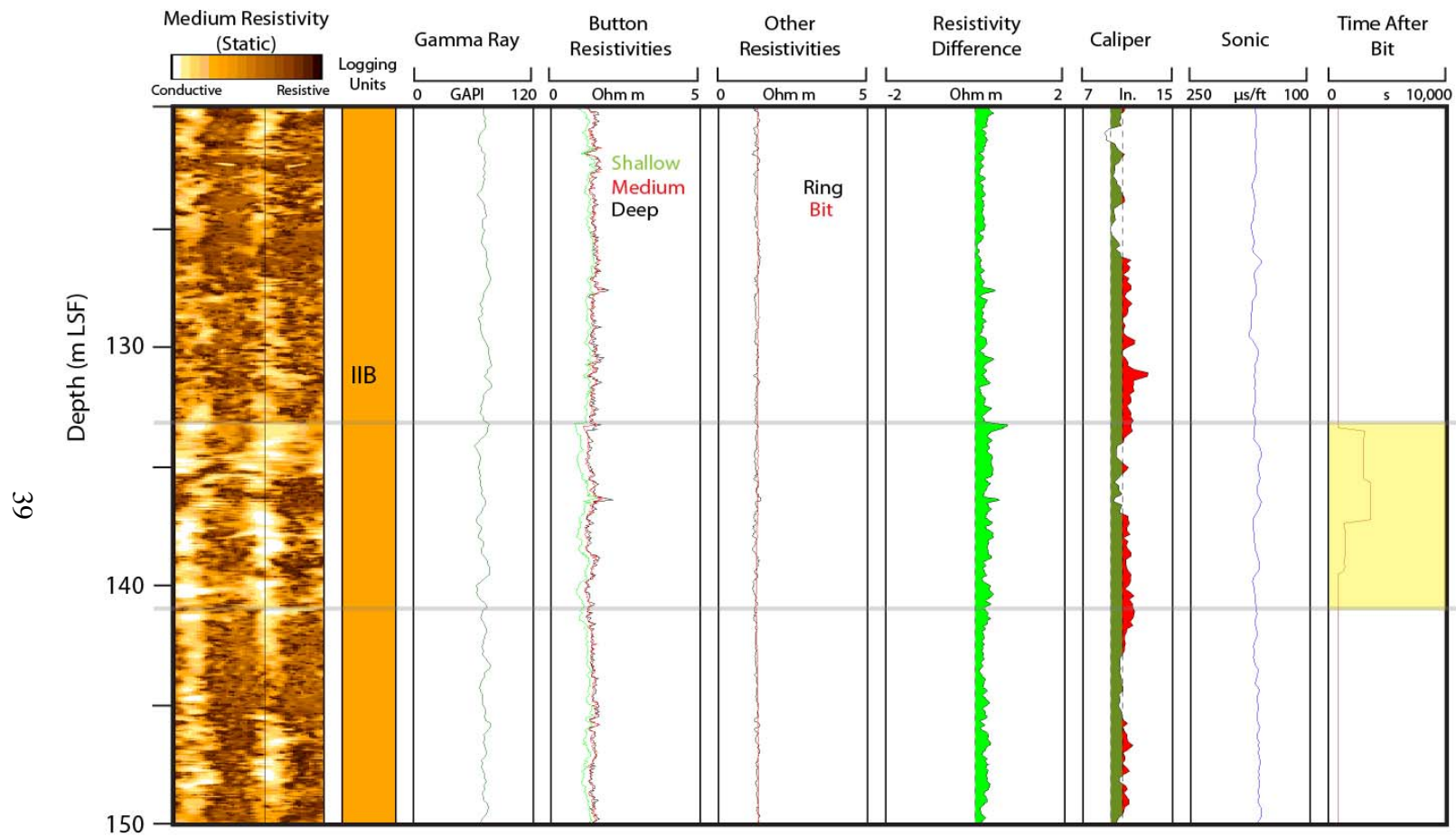


Figure 2.7: Expanded section from C0004B (Figure 2.6). Illustrates the correspondence of a fracture zone picked by onboard scientists (highlighted in yellow), anomalously conductive resistivity image log and high time after bit (TAB).

## **C0006B**

Site C0006 is located at the frontal thrust of the Nankai accretionary prism (Figure 2.1c) [*Expedition 314 Scientists*, 2009c]. Several faults are visible in the seismic image (Figure 2.8), mostly within logging Units II and III. Unit IV consists of trench sediments (identified in Figure 2.1c), which appear as a very sandy section in the gamma ray log. In Hole C0006B, TAB variations seem to have little effect on caliper, gamma ray or resistivity logs. Instead, the caliper values correlate strongly with both the gamma ray and the resistivity difference logs. This correlation implies that the resistivity differences in certain lithologies are a direct result of borehole conditions or are due to a combination of borehole washout and fluid invasion into the formation.

Our practice of choosing discrete samples with low to moderate caliper values also fails in this hole as both the caliper and resistivity difference logs have higher values and more variation in Hole C0006B than at Sites C0001 and C0004. Logging Units I and IV in particular have few caliper values below or near 10 in. Units II and III show the strongest correlation between lithology and caliper. The magnitude of resistivity difference recorded in the thicker sands could not be duplicated by the tool response model without a larger fluid resistivity contrast. Consequently, we pick no samples from Hole C0006B. Instead, we use this hole as a useful example of conditions in which resistivity difference is not correlated with invasion distance and therefore our method cannot be applied. The strong correlation between gamma ray, resistivity difference and caliper logs in Hole C0006B is distinctly different from the behavior of these logs in Holes C0001D and C0004B.

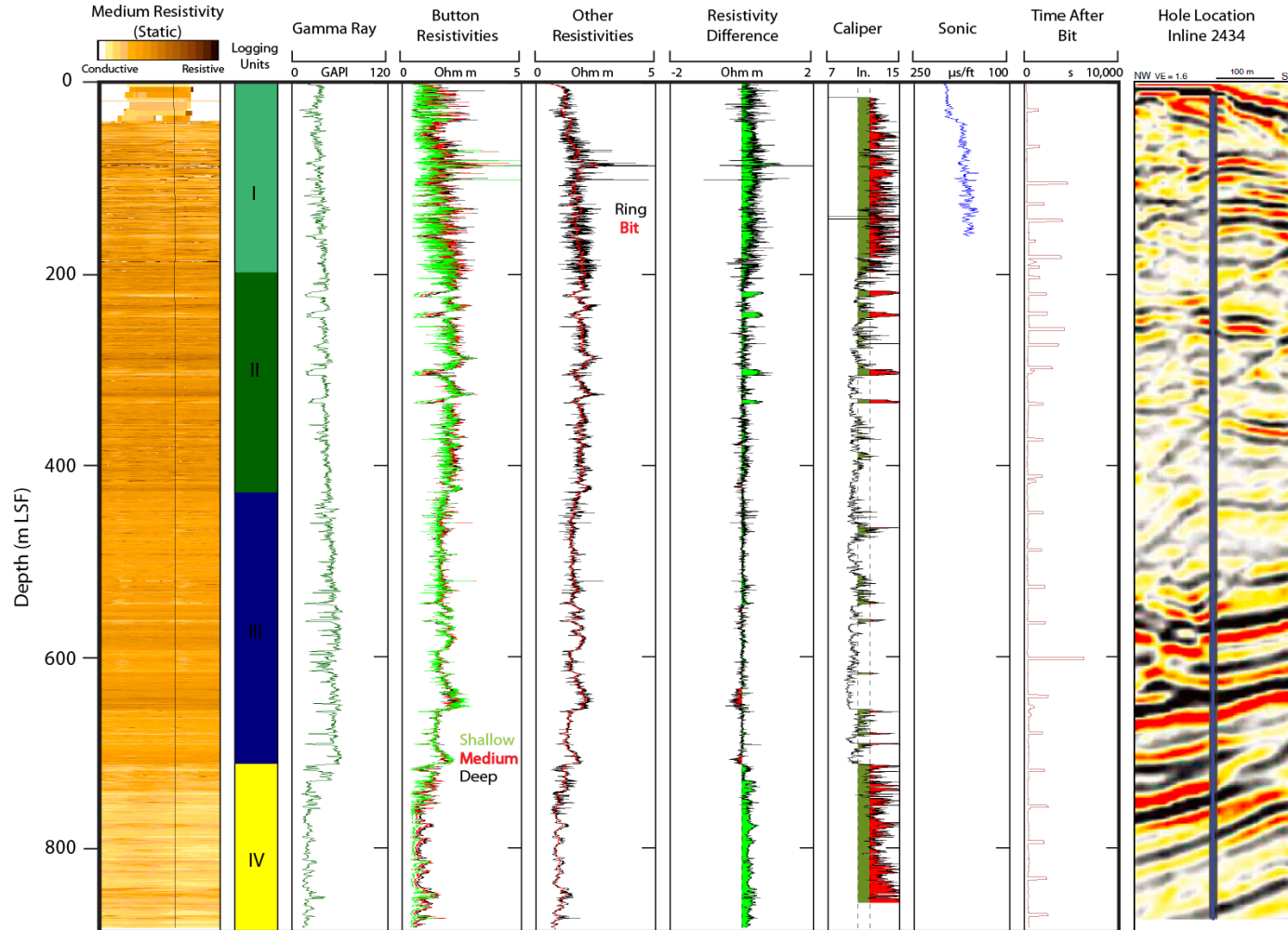


Figure 2.8:  
C0006B summary  
log diagram. See  
Figure 2.4 for  
panel descriptions.  
Units I and IV have  
very high caliper  
values. In Units II  
and III, note clear  
correspondence of  
high resistivity  
differences to both  
low gamma ray  
values and high  
caliper. We present  
this hole as an  
example of  
conditions under  
which our method  
cannot be applied.  
[Expedition 314  
Scientists, 2009c]

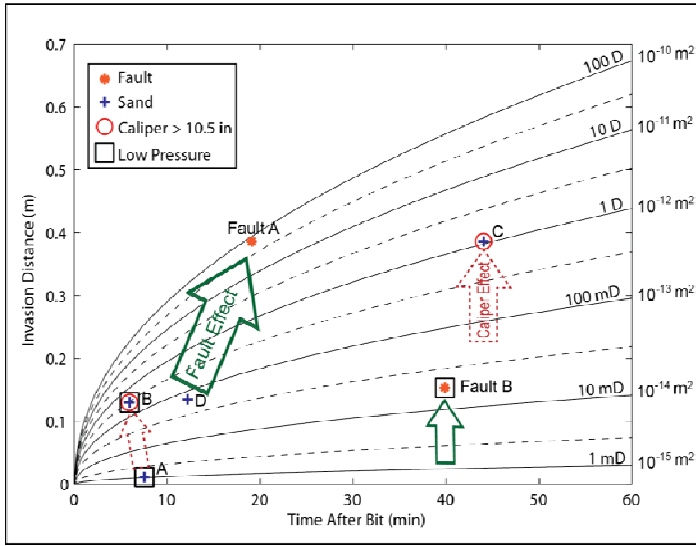
## RESULTS AND DISCUSSION

### Model Application

By inputting a range of permeabilities into our invasion model, we can see how the invasion profile changes with this variable (curves in Figure 2.9). Based on core permeability results (discussed in detail in Absolute Permeability Magnitude section below), we pick a lower bound of  $k = 10\text{-}15 \text{ mD}$  for sandy/silty, high-porosity sediments. By plotting the time elapsed between bit penetration and resistivity measurement (recorded as a time after bit log, TAB) versus invasion distances from the tool response model for each sampled sand (listed in Table 2.3) on the modeled invasion chart, we can estimate a permeability value for each sample (Figure 2.9, last column in Table 2.3). This method allows us to compare samples with different TAB values.

Hole C0001D samples (Figure 2.9a) can be divided into two groups: those drilled with lower borehole pressures (closer to hydrostatic) and those drilled with higher borehole pressures. Different pressure gradients from the borehole into the formation will cause different speeds of invasion. Thus, when discussing samples' relative magnitudes of permeability, samples with lower pressure contrast should not be compared to samples with higher pressure contrast. The lower pressure contrast samples are the shallowest (Fault A, Sand A and Sand B, denoted by boxes in Figure 2.9a) and exhibit consistently lower modeled invasion distance than the deeper, higher pressure contrast samples. Significantly, in both cases, the fault samples correspond to invasion curves with significantly higher permeabilities than the unfaulted sands, with differences of  $\sim 1.5$  and 3 orders of magnitude, respectively.

**C0001D**



**C0004B**

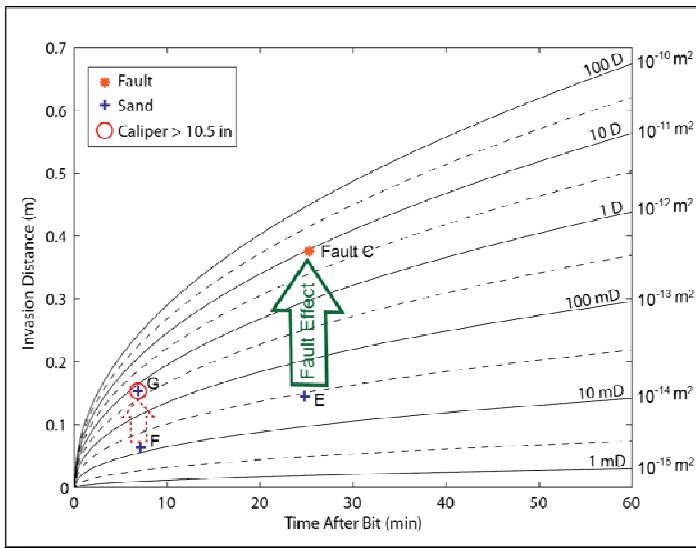


Figure 2.9: Model Results. Time after bit (TAB) vs. invasion distance (from tool response model) for each sample plotted over a chart of modeled invasion profiles for varying permeability. Log and model values for each point are in Table 2.3.

Parameters used to create invasion profile curves shown in Table 2.1. Circles around samples with high caliper values; these samples are likely reading artificially elevated permeabilities due to washouts. a) C0001D samples. Samples in faults correspond to higher permeability curves than sands not in faults. Sands with caliper values > 10.5 inches also correspond to higher permeability curves than sands with lower caliper values. Low pressure samples from shallower depths (denoted by squares) were drilled with a lower rig floor pumping rate and should only be compared with each other. b) C0004B samples. Two sands (E and F) with different TAB correspond to similar permeabilities (30 and 12 mD). Sand G, which has a high caliper value, shows somewhat elevated permeability. Sand from a faulted zone (Fault C) shows a permeability ~2.5 orders of magnitude above sands not in faulted zone.

Hole C0004B samples (Figure 2.9b), which are all comparable in terms of pressure gradient, show a similar relationship between sands in faulted areas and sands outside faulted areas. Sands E and F yield nearly the same permeability result (30 and 10 mD respectively), despite the TAB and caliper disparities. The permeability of fault C is ~2.5 orders of magnitude higher (~10 D) despite having similar TAB to Sand E and similar caliper to Sand F.

Interestingly, the difference between calipers of 10 and 10.4 inches for Sands E and F, respectively, has only a small effect, but the difference between Sand F and Sand G (for which the caliper is 11.1) is ~1.5 orders of magnitude (Figure 2.9b). Sands B and C from Hole C0001D (Figure 2.9a) also illustrate the effect of high caliper values, raising the modeled permeabilities for these samples by 2.5 and 1 orders of magnitude, respectively. We conclude that our method is useable in boreholes with poor calipers, so long as the washouts are not too large (we estimate over 10.5 in) and points with similar caliper values and pressure contrast are compared.

## **General Results**

Propagation and maintenance of elevated pore pressures along faults and within the accretionary wedge as a whole are controlled by the permeabilities of the wedge sediments and of the many faults that cut them. If the process of faulting enhances permeability then faulted zones should allow greater fluid flow than the surrounding sediments would and act as conduits for escaping fluids under pressure. If faulting decreases permeability, faults would act as barriers to flow within the wedge. In both C0001D and C0004B, our method yields higher permeabilities for the samples within a fault than for undisturbed sands. This result is consistent with the idea of faults acting as

fluid conduits and partially controlling the escape paths of fluids from the accretionary wedge.

Several processes associated with faulting are thought to influence permeability, including fracturing, strain dilation, grain alignment, sediment alteration and cementation. In well-lithified formations, faulting is associated with fractures, which affect both porosity and permeability but not always in a manner consistent with the porosity-permeability relationship in the rest of the formation. The formations in our logging data are relatively shallow (less than 600 m below the seafloor) and are consolidated but not fully lithified marine sediments. Some of these sediments may have been brought up to shallower depths by thrust faults, leaving them in an overconsolidated state. Shearing of dense sands and overconsolidated clays causes dilation until overcoming granular interlock [Craig, 2004]. This “strain softening” increases both porosity and permeability. In contrast, loose sands and unconsolidated or normally-consolidated clays will contract as they are sheared, decreasing both porosity and permeability [Craig, 2004]. Regardless of the direction of associated volume change, shearing forces the grains in the formation to become progressively more aligned, allowing more systematic connection of pore spaces and increasing permeability above that expected for a given porosity. We believe this alignment of grains combines with shear dilation and whatever fracturing is possible in rocks this poorly lithified to increase the permeability of the damaged zone near the fault.

Cementation and mineralogical alteration also affect porosity and permeability. However, our comparison of intervals with similar gamma ray values implies similar clay content between samples. The high values of permeability produced by our models are consistent with values measured in shallow core samples (see Absolute Permeability Magnitude section below) and imply that cementation does not have a dramatic effect on

permeability in the areas we have drilled. The process of shearing itself can alter grain size as well. Along a fault plain, large grains may be mechanically pulverized, changing both the porosity and permeability. However, the damaged zone required to produce a fault plane reflector in seismic data is significantly thicker (10's of meters) than the fault plane itself. The sands we analyze within faults are from within the damaged zone and have not been pulverized, as evidenced by values of the gamma ray, ring resistivity and sonic logs consistent with nearby sands outside of the faulted intervals.

Because of the effects of shear strain and mineralogical alteration, anomalous areas may exist within a single formation, particularly within faulted intervals, where the porosity-permeability relationship is significantly different from that relationship in less deformed portions of the formation. Due to the importance of pore pressure in faulting mechanics, intervals of anomalous permeability near faults are of interest. However, the poor recovery of cores in the deformed intervals surrounding major faults, particularly the lack of cores in silty and sandy portions of these intervals, hinders determination of permeabilities in these intervals.

By using logging-while-drilling (LWD) logs to constrain permeability, we have expanded permeability information beyond the finite locations of cores and can hopefully improve the estimates of permeability used in modeling the hydrologic system within accretionary wedges. We have shown that sandy layers within faulted zones do not have the same porosity-permeability relationship as sands not inside of faulted zones. Future application of our model in other boreholes with logging data will further improve these hydrologic models without requiring expensive acquisition of additional cores. Furthermore this method is useable in sandy and/or faulted portions of the formation where core recovery is poor to nonexistent.

## Uncertain Model Parameters

Our model of fluid invasion through advection assumes values for the coefficient of consolidation ( $C_v$ ) and pressure difference ( $\Delta P$ ), neither of which is directly measured in our LWD boreholes. For  $C_v$  we choose a value at the upper end of the range reported in NanTroSEIZE samples from other holes at the same sites (see Invasion Model Discussion section above),  $5 \times 10^{-6}$  m<sup>2</sup>/s. Because the sands we analyze have lower gamma ray values and therefore lower clay content than the samples measured from cores, this higher  $C_v$  value is appropriate.

The value of  $\Delta P$  is less well-constrained than  $C_v$ . We pick a  $\Delta P$  value of 500 kPa, which is near 10% of the difference between the lithostat and the hydrostat at 500 m depth. This value is also consistent with the magnitude of the difference between the hydrostat and the pressure curve expected from rig floor pumping rates (See Appendix D for plot). An order of magnitude increase in  $\Delta P$  (to 5000 kPa) would place it near the difference between the lithostat and the hydrostat at our sample depths. Such high contrast between the borehole and formation pressure is unlikely because any increase in the formation pressure above hydrostatic would place the borehole pressure above lithostatic and impact borehole shape and stability. An order of magnitude decrease in  $\Delta P$  (to 50 kPa) also seems unlikely because the increased pumping rate between 400 and 500 m LSF in Hole C0001D should have increased the pressure by more than 100 kPa, and the borehole before (above) this increase was stable, indicating a positive pressure difference. The only samples which may have a  $\Delta P$  lower than this 100 kPa are those from above the pumping rate increase, the 'lower pressure' samples in C0001D (Fault A and Sands A and B in Table 2.3 and Figure 2.9).

An estimate of  $\Delta P$  that is within an order of magnitude is robust enough for our purpose because our primary focus is on determining relative magnitudes of permeability

in comparable sands. An order of magnitude change in  $\Delta P$  will produce the same invasion distance versus time curve if  $k$  changes by an opposite order of magnitude. In other words, the curve in figure 2.3d was calculated for  $\Delta P = 500$  kPa and  $k = 10^{-19}$  m<sup>2</sup>, but would be exactly the same for  $\Delta P = 50$  kPa and  $k = 10^{-18}$  m<sup>2</sup>. Physically, in order to invade the same distance in the same time with a lower  $\Delta P$ ,  $k$  must increase. Therefore any errors in  $\Delta P$  will affect our results in a systematic manner, which will not hamper comparisons made between multiple sands so long as those sands are at somewhat similar pressure conditions.

### **Absolute Permeability Magnitude**

Due to uncertainties in the parameters discussed above, our model is not expected to yield absolute magnitudes of permeability with complete accuracy. Our analysis and conclusions focus instead on the relative magnitude of permeability modeled in comparable sands. However, the permeabilities we model for our sands ( $10^{-15}$  to  $10^{-10}$  m<sup>2</sup> or 1 to 100,000 mD) are in a range similar to the highest measured permeabilities in analyses of cores from the Nankai Trough.

Site 808 (ODP Leg 131, Muroto Transect, Figure 1a) yielded cores from the outermost accretionary prism with measured horizontal and vertical permeabilities [Taylor and Fisher, 1993]. Saffer and Bekins [1998] model the effect of smectite dehydration and a transient increase in décollement permeability to reproduce the chlorinity profile at Site 808. Their model assumes bulk permeabilities between  $\sim 10^{-17}$  and  $10^{-19}$  m<sup>2</sup>, varying log-linearly with porosity and the décollement permeability increases from  $10^{-16}$  to  $10^{-13}$  m<sup>2</sup> transiently. Cores from Sites 1173 and 1174 (ODP Leg 190) in the proto-thrust zone and incoming sediments had measured permeabilities in the range of  $3.7 \times 10^{-19}$  to  $6.45 \times 10^{-17}$  m<sup>2</sup> (0.00037 to 0.0645 mD) [Gamage and Screaton,

2003]. These mudstones are 2-100 times less permeable than the turbidite-rich units in the lowermost portion of the section measured along the Ashizuri transect to the southwest (Figure 2.1a) [Saffer, 2010]. Modeling by Saffer [2010] shows that the lower permeabilities along the Muroto transect can account for higher pore pressures and thus a lower taper angle than is exhibited by the Ashizuri transect. However, this regional-scale analysis assumes a flow path up to and then along the décollement and neglects the effects of varying permeability in the upper wedge, and thus may not fully characterize fluid escape from the system.

Along the Kumano transect, permeabilities of cores from Sites C0004, C0006, C0007 and C0008 within the accretionary prism (Figure 2.1b,c) have been reported ranging from  $10^{-18}$  to  $4.6 \times 10^{-14} \text{ m}^2$  [Dugan and Daigle, 2010; Rowe et al., 2010; Saffer et al., 2010a]. This range includes higher permeability values than the other two transects despite a lack of cores in the most sandy/silty units. Our model permeabilities in sands are near the upper end of this range, adding to our confidence in our modeling technique.

### **Future Work**

To further test this technique, more samples would be desirable but unfortunately are not available within the Expedition 314 logs. Incorporation of LWD data from Legs 190 and 196, Expeditions 319 and 322 and any future Nankai logging is possible, but analysis of these wireline measurements will require use of a different tool response simulation and longer model times. Over longer model times, the effect of salt diffusion must also be incorporated, as advection slows with time but diffusion does not (see Appendix A). The most significant improvements to the model itself could be made by better constraining the pressures, specifically the difference between borehole and formation pressures at any given point.

## CONCLUSIONS

The effect of borehole fluid invasion can be seen in the difference between shallow and deep resistivity measurements in the IODP Expedition 314 logging-while-drilling (LWD) data, despite the low time after bit (TAB) inherent to LWD measurements. Comparisons between ten sandy layers in boreholes C0001D and C0004B indicate higher permeabilities in sands within faults observed in the seismic data than in sands not within faults.

Our method requires that TAB be known and is somewhat sensitive to caliper values, particularly those greater than 10.5 inches (for the combination of the geoVISION tool and a 8.25 inch bit). Selection of samples with similar caliper and gamma ray log values improves the precision of the relative estimates of permeability. Our method is not suitable for holes with strong correlation between the caliper and resistivity difference, generally associated with washouts of sandy beds.

Table 2.4: Nomenclature and Acronyms

	<b>Description</b>	<b>Units</b>	<b>Dimensions</b>
<i>a</i>	Radius of borehole	m	L
A	Area	m <sup>2</sup>	L <sup>2</sup>
<b>APRS</b>	Average annular pressure from the annular pressure while drilling tool	kPa	$\frac{M}{LT^2}$
<b>BD</b>	Deep Button Resistivity ( $\Omega m$ )	$\Omega m$	$\frac{ML^3}{TC^2}$
<b>BS</b>	Shallow Button Resistivity ( $\Omega m$ )	$\Omega m$	$\frac{ML^3}{T^3C^2}$
<b>CCAV</b>	Caliper (average of the four directional caliper logs)	in.	L
<i>c<sub>v</sub></i>	Coefficient of consolidation	m <sup>2</sup> /s	$\frac{L^2}{T}$
<i>d<sub>i</sub></i>	Distance of invasion, measured from the borehole wall	m	L
k	Permeability	m <sup>2</sup>	L <sup>2</sup>
<b>HRLA</b>	Schlumberger High-Resolution Laterolog Array	-	
<i>m</i>	Archie's cementation exponent	-	
<i>m<sub>v</sub></i>	Coefficient of volume compressibility	kPa <sup>-1</sup>	$\frac{LT^2}{M}$
<i>n</i>	Archie's saturation exponent	-	
<i>P</i>	Pressure	kPa	$\frac{M}{LT^2}$
<i>P*</i>	Excess pore pressure		
<i>P<sub>f</sub></i>	Formation Pressure	kPa	$\frac{M}{LT^2}$
$\Delta P$	Difference between borehole and formation pressures	kPa	$\frac{M}{LT^2}$
$\bar{q}$	Flux	m/s	$\frac{L}{T}$
<i>Q</i>	Volume Discharge	m <sup>3</sup>	L <sup>3</sup>

Table 2.4, continued:

	<b>Description</b>	<b>Units</b>	<b>Dimensions</b>
$R_t$	Formation Resistivity	$\Omega\text{m}$	$\frac{\text{ML}^3}{\text{T}^3\text{C}^2}$
$R_w$	Water Resistivity	$\Omega\text{m}$	$\frac{\text{ML}^3}{\text{T}^3\text{C}^2}$
$R_m$	Mud Resistivity (usually near that of sea water)	$\Omega\text{m}$	$\frac{\text{ML}^3}{\text{T}^3\text{C}^2}$
$R_{xo}$	Resistivity of fully invaded formation	$\Omega\text{m}$	$\frac{\text{ML}^3}{\text{T}^3\text{C}^2}$
$S_w$	Water saturation	-	
<b>TAB</b>	Time After Bit (deep button resistivity)	min.	T
$\vec{v}$	Pore velocity	m/s	$\frac{\text{L}}{\text{T}}$
$\vec{v}_r$	Radial component of pore velocity	m/s	$\frac{\text{L}}{\text{T}}$
$\alpha$	Archie's compaction factor	-	
$\gamma_w$	Unit weight of sea water	$\text{N}/\text{m}^3$	$\frac{\text{M}}{\text{L}^2\text{T}^2}$
$\mu$	Viscosity of water	Pa-s	$\frac{\text{M}}{\text{LT}}$
$\varphi$	porosity	-	

M = mass

L = length

T = time

C = electrical charge

### **Chapter 3: The Kumano Basin Edge Fault Zone as a Potential Strain Partitioning Structure between the Kumano Basin and the Slope of the Nankai Trough Accretionary Prism**

This chapter has been modified from its previous publication:

Martin, K. M., S. P. S. Gulick, N. L. B. Bangs, G. F. Moore, J. Ashi, J. O. Park, S. i. Kuramoto, and A. Taira (2010), Possible Strain Partitioning Structure Between the Kumano Forearc Basin and the Slope of the Nankai Trough Accretionary Prism, *Geochemistry Geophysics Geosystems*, 11(B12), Q0AD02.

Dr. Gulick and Prof. Moore provided feedback and advice on contextualizing my interpretations and preparing the paper for publication. Dr. Bangs introduced me to the dataset and served as my main interface with our Japanese colleagues, Drs. Park, Kuramoto and Taira, who had roles in planning the data acquisition and processing the Kumano 3D seismic dataset (particularly producing the depth-migrated section). Dr. Ashi provided the previously unpublished side-scan sonar data shown in Figure 3.2. All of these coauthors have played a vital role in the production of the 3D seismic dataset and in the interpretation of large-scale structures within it. In this chapter I focus on a previously uninterpreted portion of the dataset where I perform detailed interpretation and structural analysis.

#### **ABSTRACT:**

A 12 km wide, 56 km long, three-dimensional (3-D) seismic volume acquired over the Nankai Trough and Kumano forearc Basin, offshore Japan images the accretionary prism, forearc basin and subducting Philippine Sea Plate. We have analyzed an unusual, trench-parallel depression (a “notch”) along the seaward edge of the forearc Kumano Basin, just landward of the megasplay fault system. This bathymetric feature

varies along strike, from a single, steep-walled, ~3.5 km wide notch in the northeast, to a broader, ~5 km wide zone with several shallower linear depressions in the southwest.

Below the notch we found both vertical faults and faults which dip toward the central axis of the depression. Dipping faults appear to have normal offset, consistent with the extension required to form a bathymetric low. Some of these dipping faults may join the central vertical fault(s) at depth, creating apparent flower structures. Offset on the vertical faults is difficult to determine, but the along-strike geometry of these faults makes predominantly normal or thrust motion unlikely. We conclude, therefore, that the notch feature is the bathymetric expression of a transtensional fault system.

By considering only the along-strike variability of the megasplay fault, we could not explain a transform feature at the scale of the notch. Strike-slip faulting at the seaward edge of forearc basins is also observed in Sumatra and there attributed to strain partitioning due to oblique convergence. The wedge and décollement strength variations which control the location of the forearc basins may therefore play a role in the position where an along-strike component of strain is localized. Although the obliquity of convergence in the Nankai Trough is comparatively small (~15 degrees), we believe it generated the Kumano Basin Edge Fault Zone, which has implications for interpreting local measured stress orientations and suggests potential locations for strain-partitioning-related deformation in other subduction zones.

## **INTRODUCTION:**

In subduction zones characterized by convergence that is oblique to the plate boundary, partitioning of strain between a generally convergent subduction complex and a trench-parallel transform fault or set of faults is commonly observed [Fitch, 1972]. This

partitioning results in a system of faults, typically located near the volcanic arc, which can produce significant strike-slip earthquakes. Examples include the Sumatra fault [Fitch, 1972; Jarrard, 1986] and the Median Tectonic Line in southern Japan [Nishimura and Hashimoto, 2006; Tabai *et al.*, 2002]. The northeastern Caribbean exhibits varying degrees of strain partitioning as the subduction zone curves to the northwest [Manaker *et al.*, 2008]. Obliquity of convergence is at a maximum near Hispaniola and Puerto Rico, where onshore faults accommodate margin parallel motion. Additionally, the Aleutian, Chilean and Peruvian margins exhibit onshore strike-slip faulting consistent with the obliquity of convergence [Jarrard, 1986]. Cascadia also has a number of both onshore and offshore strike-slip faults, but many of these lie within the subducting plate [Goldfinger *et al.*, 1997] and may or may not be a direct result of strain-partitioning. From Japan and Sumatra to Hispaniola and Chile, geohazards of oblique subduction zones therefore include both dip-slip megathrust events with potential, associated tsunami generation and strike-slip “forearc sliver” earthquakes.

Most studies of strain partitioning focus on strike-slip faults near or beneath the volcanic arc, but some margin-parallel motion may occur offshore as well. The West Andaman and Mentawi Fault systems offshore northern and central Sumatra are thought accommodate a significant amount of dextral transform motion [Malod and Kemal, 1996; Samuel and Harbury, 1996]. Strike-slip faults extend offshore from Hispaniola and many of the observed transform faults along the Cascadia margin are in the submarine forearc. Perhaps strike-slip faults caused by strain partitioning in oblique subduction zones can nucleate offshore, in the forearc, as well as along the volcanic arc.

In this study, we focus on the Nankai Trough subduction zone, probably the most studied subduction zone in the world [e.g. Bangs *et al.*, 2004; Gulick *et al.*, 2004; Kinoshita *et al.*, 2009; Mikada *et al.*, 2005; G F Moore *et al.*, 2007; Park *et al.*, 2002;

*Taira et al.*, 1992]. Along this margin, the convergence vector between the Philippine Sea Plate and the Eurasian Plate is ~15 degrees from perpendicular to the trench [*Seno et al.*, 1993], but despite this minimal obliquity, evidence of strain partitioning is still apparent. Japan's Median Tectonic Line is located along the center of the volcanic arc and exhibits right-lateral motion, consistent with the margin parallel component of strain [*Tabai et al.*, 2002], while a subduction megathrust (in combination with the associated megasplay fault) accommodates margin perpendicular strain along the plate boundary [*G F Moore et al.*, 2007; *Nishimura and Hashimoto*, 2006; *Park et al.*, 2002]. Historically, earthquakes on both the strike-slip faults (e.g., Kobe 1995) and the subduction megathrust (1944 and 1946 M~8.0 tsunamigenic events) have caused significant damage [*Dunbar*, 2010].

In an effort to further understand the mechanics and spatial distribution of strain in the Nankai Trough, we have utilized a three-dimensional, multichannel seismic reflection volume acquired over the Nankai Trough accretionary prism, which images a trench-parallel, linear depression (a “notch”) along the edge of the forearc basin [*G F Moore et al.*, 2009]. If this notch is a structural feature, its strike may make it a candidate for strain-partitioning. Our study concentrates on this notch feature in an effort to determine the degree to which strain partitioning may be involved in its formation and the implications for localization of strike-slip faults adjacent to forearc basins in oblique subduction settings. We also discuss the implications of a structure between the forearc Kumano Basin and the forearc slope for studies of the local stress field.

## **NANKAI TROUGH TECTONIC SETTING**

In the Nankai Trough, the Philippine Sea Plate is subducting beneath the Eurasian Plate at ~ 4 cm/yr [*Seno et al.*, 1993] with a convergence vector ~15 degrees from

perpendicular. Convergence obliquity varies with local changes in the strike of the trench, which are fairly common. To the northeast, where the Izu-Bonin arc enters the subduction zone, the trench axis deflects to the north and a complex system of thrusts and dextral strike-slip faults have been observed [*Huchon et al.*, 1998; *Tokuyama et al.*, 1999]. To the southwest, the trench axis bends gradually toward the south, decreasing the obliquity of convergence offshore Kyushu.

Seismic surveys imaging the portion of the margin off the Kii Peninsula show a strong set of reflections branching upward from the main megathrust ~50 km landward of the trench, which is interpreted as a splay of this fault [*G F Moore et al.*, 2007; *Park et al.*, 2002]. Along with several other less-reflective thrust splays, this megasplay cross-cuts older faults interpreted to be part of the imbricate thrusting sequence and is therefore an out-of-sequence thrust (OOST). Inversion of tsunami waveforms caused by the 1944 M~8.1 Tonankai seismic event, which ruptured the megathrust beneath the forearc Kumano Basin, indicates that slip could have occurred on the megasplay fault instead of the plate boundary during this event [*Baba et al.*, 2006]. Seismic slip on a splay fault (steeper than the décollement) could have implications for the magnitude of tsunami generation in seismic events [*G F Moore et al.*, 2007].

Above this imaged megasplay fault system, bathymetric measurements off the Kii Peninsula in the Nankai Trough show a trench-parallel, linear bathymetric low (a “notch”) on the seaward edge of the forearc Kumano Basin. This notch varies in relief and width but extends along strike nearly 100 km (Figure 3.1). This location places the notch feature in the hanging wall of the uppermost mapped fault of the megasplay fault system, just landward of the surface expression of this uppermost fault and almost directly on the slope break.

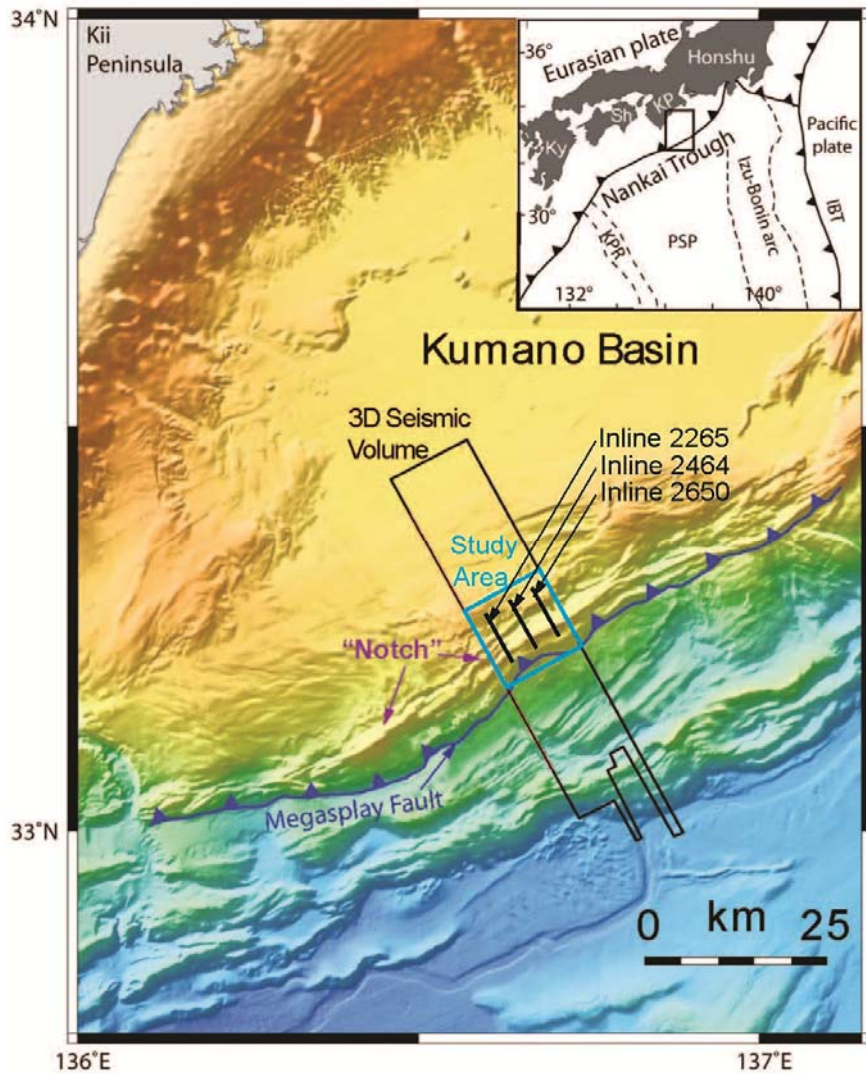


Figure 3.1: Bathymetry of the Nankai Trough, showing the location of the 3-D seismic survey and previously interpreted faults. The notch feature discussed in this paper crosses near the center of the 3-D survey area, striking NE-SW. The portion of the feature imaged by the 3D seismic dataset is 750 m deep and 3 km across in the northeast and splits to the southwest into several parallel ~250 m deep depressions across a zone of deformation approximately 5 km wide. The deepest part of this feature (~1.2 km deep) is found northeast of the study area. The convergence direction between the Philippine Sea Plate and the Eurasian plate is shown at the lower right [Seno *et al.*, 1993]. Inset shows the regional setting of the Nankai Trough. PSP = Philippine Sea Plate; KPR = Kyushu-Palau Ridge; IBT = Izu-Bonin Trench; KP = Kii Peninsula; Sh = Shikoku Island; Ky = Kyushu Island. [Modified from *G F Moore et al.*, 2007]

## DATA:

The Nankai accretionary prism, the forearc Kumano Basin and the subducting Philippine Sea Plate are imaged in a 12 km wide, 56 km long, three-dimensional (3-D) seismic reflection volume acquired offshore the southeastern Kii Peninsula, Japan [*G F Moore et al.*, 2009]. These data were acquired using a commercial seismic vessel towing two airgun source arrays (totaling 3090 cu in) and four 4.5 km long hydrophone streamers. The recorded sonic wave field data were processed using a 3D pre-stack time migration, and later a pre-stack depth migration was performed which more clearly imaged details of faults and small-scale structures [*Uraki et al.*, 2009].

The vertical resolution of the resultant data set is 5-7 meters at the seafloor, 10-20 meters at depths near 1400m (~580 ms) and ranges down to ~100m near the oceanic crust [*G F Moore et al.*, 2009]. The well-imaged area beneath the observed notch feature is relatively shallow, corresponding to vertical resolutions between 5 and 20 meters. We utilize both the time and depth sections in this study, as some features are more distinct in each.

This data volume is an integral part of the Nankai Trough Seismogenic Zone Experiment (NanTroSEIZE), the goal of which is to investigate subduction fault mechanics and seismogenesis [*Ashi et al.*, 2007; *Kinoshita et al.*, 2007]. This integrated imaging, drilling, and monitoring initiative will utilize multiple platforms and expeditions to combine *in situ* measurements, sampling and long-term monitoring of several faults within the Nankai Trough subduction complex. *Moore et al.* [2007] have mapped the megasplay fault system using these same data, as well as a number of 2D seismic lines. Our study utilizes both the 3D seismic data below the notch area and interpretations of megasplay fault geometry performed previously [*Bangs et al.*, 2009; *G F Moore et al.*, 2007; *Pangborn*, 2007].

## **METHODS:**

In this study we performed interpretations of the 3D seismic data in the vicinity of the notch. Our interpretation of these faults included both mapping and classification components. For the mapping portion, we interpreted the laterally extensive faults below the notch (Figures 3.2 and 3.3), as well as the edges of the sediment packages found in the southwest portion of the study area. Given the complexity of the structure, the mapping study was only possible due to the horizontal (along strike) resolution of the 3D data. Faults typically could only be conclusively differentiated from noise or artifacts by considering continuity and similarity of seismic character across multiple inlines.

Our classification focused on determining whether the mapped features are transform, normal or thrust faults. Bases for classification included direction and amount of seafloor offset, dip angle and variations in dip angle, relationship(s) to other features and continuity of characteristics. We suggest that faults which display a lack of continuity or highly variable characteristics such as reflectivity and dip angle are unlikely to play a major role in the deformational history of the notch. We consider continuous along strike faults with consistent characteristics for their regional significance.

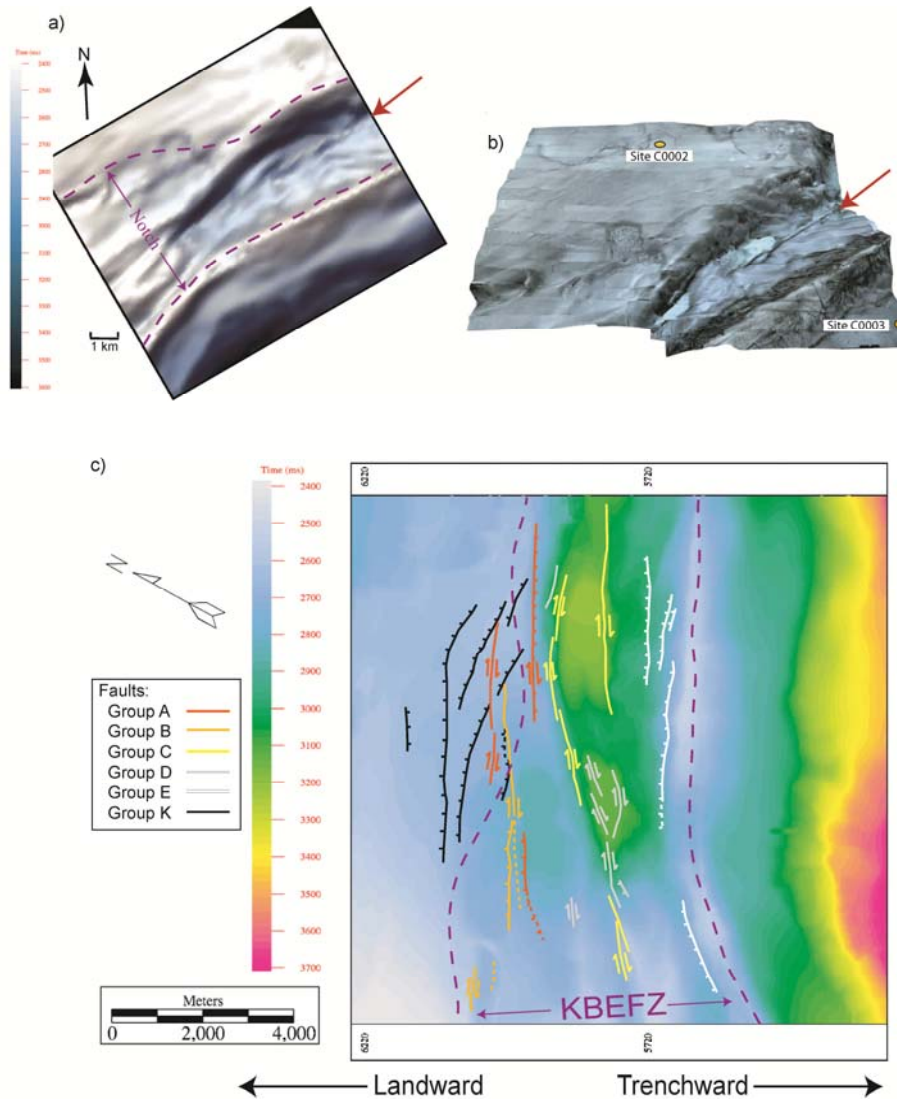


Figure 3.2: Bathymetry Maps. a) Bathymetric map generated from the seafloor reflection picked in the 3D seismic data. The notch is deep and narrow to the northeast and shallower and wider to the southwest. Note the linear feature in the right-hand (NE) portion of the depression (arrow). This feature, more evident in the side-scan sonar image to the right, corresponds to the central fault mapped below the northeastern notch (see Figure 3.3). b) Side-scan sonar image draped over bathymetry; collected by deep-tow side-scan sonar Wadatsumi over the forearc Kumano Basin and forearc slope [Ashi *et al.*, 2007]. Yellow dots indicate proposed NanTroSEIZE sites which have now been drilled (IODP sites C0002 and C0003). c) Bathymetric map showing mapped fault locations. Faults which appear to be transform in nature are shown with an offset direction based on convergence direction. Based on the correspondence between faults and bathymetric features, we introduce the idea that the notch is the surface expression of a Kumano Basin Edge Fault Zone (KBEFZ).

Examination of the data shows a lack of continuous or uniquely identifiable sedimentary packages within the notch (Figure 3.3), which made determination of fault offset difficult. Dipping faults (between 40 and 70 degrees) that reach the seafloor show normal offset with the downthrown side most often oriented towards the center of the notch. Therefore we make the assumption based on degree of dip, this offset and the existence of a significant bathymetric low (0.75 deep in our study area to 1.2 km deep moving northeast along strike) that these dipping faults are primarily extensional. In contrast, features that are primarily vertical (dipping 85 to 90 degrees) or exhibit changes in vergence along strike, we interpret to be dominantly translational. Faults that dip toward an apparently transform feature may be elements of a flower structure.

We find no conclusive evidence of reverse offsets on mapped dipping faults. Without coherent reflectors to correlate across the faults, we rely mostly on seafloor offset and fault dip for our classification of fault motion. The faults with the clearest surface traces are generally vertical or exhibit changes in vergence along strike, precluding a purely reverse sense of motion. However, a component of compression or extension on primarily translational faults is possible.

#### **OBSERVATIONS:**

Within the seismic reflection volume, the shape of the notch varies along strike, from a single, steep-walled, ~3 km wide and ~0.75 km deep depression in the northeast to a broader, ~5 km wide zone with several shallower linear bathymetric lows in the southwest (Figure 3.2). A linear, trench-parallel depression of this magnitude between the slope of the accretionary wedge and the forearc basin is seemingly unique. The Bottom Simulating Reflector (BSR) is strong throughout most of the study area but has distinct

gaps beneath steep seafloor slope breaks, such as the landward (northwestern) edge of the notch. Interpretation below 2000 m sub-seafloor is hampered by poor imaging due to the trough-like topography, strong BSR and likely associated gas deposits, and structural complexities from extensive deformation and fracturing. The splay fault geometry in this poorly-imaged zone is inferred from the updip and downdip mapping [*Bangs et al.*, 2009; *G F Moore et al.*, 2007].

Faults within the Kumano Basin (Table 3.1 and Figure 3.2, group K) generally strike in two directions, ~90 degrees and ~60 degrees east of north, with a few faults bending from one orientation to the other [*Gulick et al.*, 2010]. These faults typically dip 55-60 degrees to the northwest in the portion of the basin nearest the notch. A couple of faults with the more northerly orientation dip to the southeast at an angle near 80 degrees, steeper than their northwest dipping counterparts. To the southeast, near the bathymetric notch discussed in this paper, we find two faults (group A) striking at 60-65 degrees east of north, which dip southeast at a similar angle of 75-80 degrees. Group A faults appear similar in dip and normal offset to the southeast dipping Kumano Basin faults, but offset amount varies along strike or is unclear due to disruption of sediments.

Several packages of sediments within the southwestern notch resemble basin sediments in apparent brightness and seismic contrast. Between these packages the sediments appear disrupted, with no parallel layering and few continuous reflectors. Along the northwest edge of the notch feature, several faults bound the edge of the basin sediments as well as these sediment packages. These faults (group B) exhibit more changes in dip along strike than the faults of group A, as well as some vertical sections. The consistent difference in apparent sediment coherence across group B faults could indicate out-of-plane motion along these faults.

Table 3.1: Mapped faults classified by dip and apparent offset where possible.

SS = strike slip, N = normal, SS/N = transtensional

Group	Fault	Strike	Dip	Fault Type	Description
A	A1	66	-78 to -81	SS/N	Consistent strike and dip with evidence for transform motion
	A2	64	-81	SS/N	
	A3	62	-76	SS/N	
	A4	40 to 58	83	SS/N	
B	B1	60	-68 to 90	SS/N	Variation in dip along strike, bound basin or coherent sediment packages
	B2	62	63	SS/N	
	B3	68	90	SS	
	B4	66	variable	SS	
C	C1	63	-67 to 90	SS	Near vertical. Some switch vergence along strike
	C2a	70	~80	SS	
	C2b	58	86	SS	
	C2c	48	80 to 90	SS	
	C3	41	90	SS	
	C4	52	~90	SS	
D	D1	42	~90	SS	Shorter faults with fewer clear indications of offset direction. Most bend in both strike and dip
	D2	39	variable	SS/N	
	D3	44 to 72	variable	?	
	D4	38 to 55	67 to 90	SS/N	
	D5	34	-56	N?	
	D6	63	80	SS	
	D7a	63	variable	?	
	D7b	63	~90	SS	

Table 3.1, continued:

Group	Fault	Strike	Dip	Fault Type	Description
E	E1	61	~50	N	Normal faults beneath seaward slope, dip NW
	E2	70	58	N	
	E3a	65	43	N	
	E3b	65	43	N	
	E4	40	49	N	
	E5	76	46	N	
K	K1a	62	66	N	Normal faults within the Kumano Basin. Only K6 dips SE
	K1b	75	54	N	
	K2a	88	55	N	
	K2b	68	52	N	
	K3	85	53	N	
	K4	85	57	N	
	K5a	91	58	N	
	K5b	61	59	N	
	K6	61	-79	N	

Within the depression itself, we have mapped several faults (group C) which are generally vertical and sometimes sinuous in depth. Group C faults, though all similar in dip, vary in strike from 42 to 70 degrees east of north. The best example of this group is fault C1, which is also visible in the sidescan sonar and seafloor bathymetry maps (Figure 3.2). This fault strikes at 60 degrees and is near vertical, but rolls over along strike, dipping to the northwest on the northeastern end and the southeast on the southwestern end. Such geometric variation on an active fault can only occur when the sense of motion is translational.

Faults which are difficult to categorize make up group D, which are all beneath the bathymetric depression, mostly toward the center. Several of these faults have variable dips (60-90 degrees) and several bend 30 to 40 degrees in strike direction. Within the group, strikes vary from 35 to 110 degrees east of north. Change in dip associated with a change in strike indicates a compound fault type. The nature of the surrounding faults and the associated seafloor low makes transtension more likely than transpression.

The seaward side of the bathymetric depression is smoother and more consistent than the landward side in both strike and dip. Beneath this slope and in many places defining this slope are a number of normal faults (group E). These faults dip between 43 and 57 degrees to the northwest, shallower than the dips of the normal faults within the Kumano Basin. Horizontal and subhorizontal reflectors indicate more coherent sediment packages beneath this slope than beneath the central notch or the landward slope. However, these packages are not distinctive enough to determine explicit offset amounts across any of the group E faults.

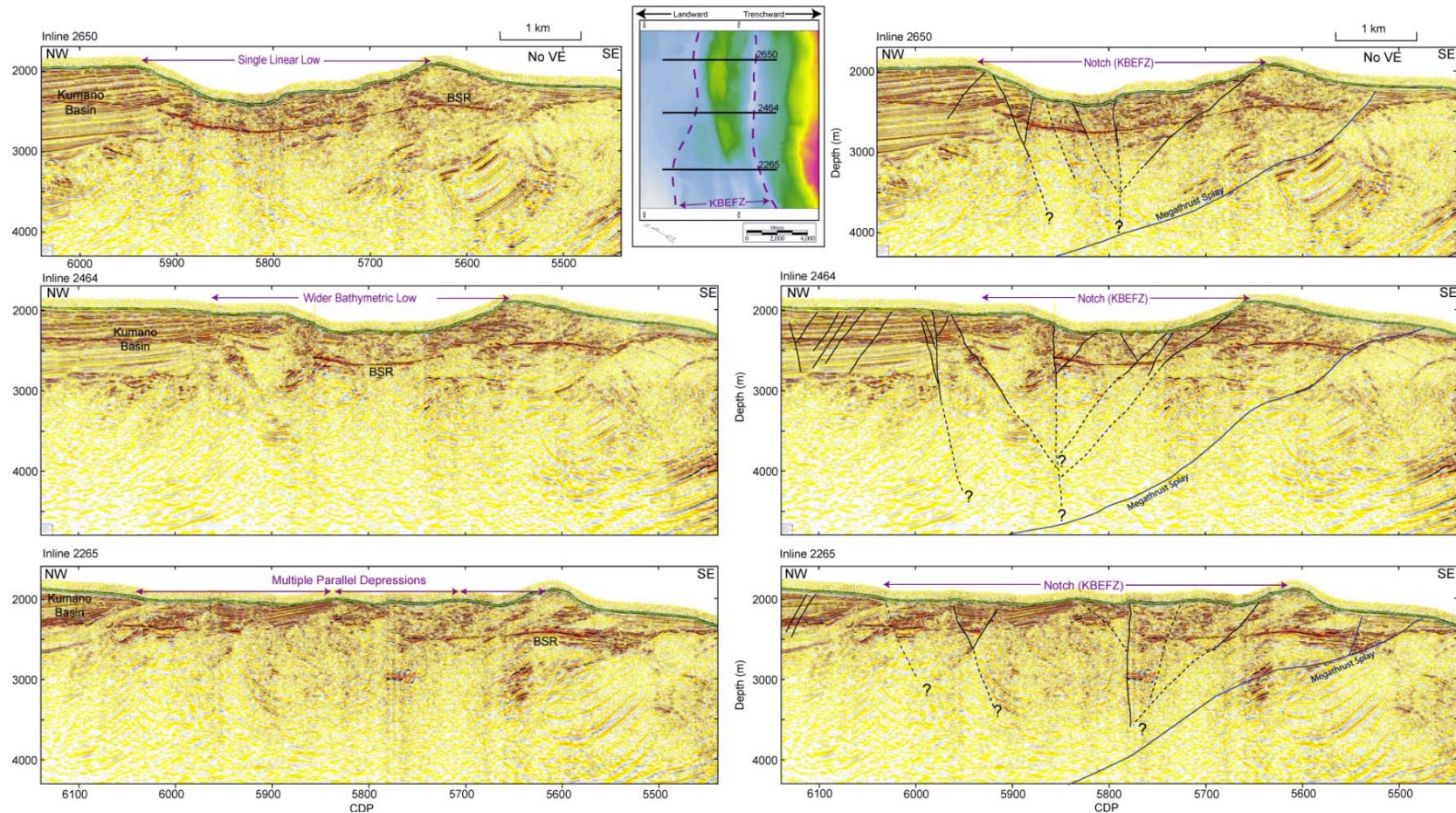


Figure 3.3: (a-c) Cross sections (in depth) of the notch and (d-f) corresponding interpretations. Sections are displayed with no vertical exaggeration. The notch feature is a linear bathymetric low along the edge of the forearc Kumano Basin and in the hanging wall of the uppermost branch of the megasplay fault system [G F Moore *et al.*, 2007]. A bottom-simulating reflector (BSR) is evident in most of the study area.

Figure 3.3 (continued): a) Northeast inline (2650): The notch is narrow (~3 km wide and ~0.75 km deep) with basin sediments truncated by faults bounding the bathymetric low. Faults are mostly steep and occasionally vertical or sinuous, indicating a possible strike-slip nature. The vertical fault at center corresponds to a linear feature in the bathymetry (Figure 3.2). b) Central Inline (2464): The coherent basin sediments begin stepping to the northwest. Steep faulting along the edge of the basin is more laterally continuous than that in the center of the notch. The megathrust splay is deeper here than in the northeast. c) Southwest Inline (2265): Characterized by distinct blocks of sediment where the basin boundary continues to retreat northwest. These sediment blocks may be remnants of basin packages disrupted by faulting. The bathymetric low is wider than that in the northeast and encompasses several shallow depressions. The geometry of the megathrust splay is similar to that in the central part of the study area, placing it deeper than in the northeast.

#### **INTERPRETATIONS:**

From our detailed interpretation of the shallow notch area, we find a number of faults with varying dips and lateral extents. These faults are distinct from the suite of normal faults found in the Kumano Basin sediments to the northwest [Gulick et al., submitted]; most faults below the notch dip more steeply and are notably more variable along strike than the extensional faults which formed in the basin. Fault strikes associated with the depression are consistently more northerly than those of the basin faults. This area is therefore considered to be a distinct zone of faulting along the edge of the forearc basin, which we refer to as the Kumano Basin Edge Fault Zone [KBEFZ; *G F Moore et al.*, 2009].

Faults below the central axis at the bottom of the bathymetric notch are near vertical and sometimes sinuous or upwardly splayed when viewed in cross-section (Figure 3.3). Therefore these faults probably have a significant translational component

of motion. Off-axis faults often dip toward the central axis, but some of these faults show no definitive indication of the sense of slip.

The northeast portion of the study area (Figure 3.3a), where the KBEFZ is narrow and basin sediments are truncated by faults bounding the bathymetric low, exhibits the clearest structure. These faults are mostly steep (dipping greater than 60 degrees) and dip toward a vertical fault at the center of the depression, indicating possible strike-slip deformation. The vertical fault at the center of this possible flower structure, corresponds to a linear feature noted in sidescan sonar data (Figure 3.2b) [Ashi *et al.*, 2007] and visible in the bathymetry (Figure 3.2a,c), reinforcing the interpretation of strike-slip deformation. The two outermost splays of this possible flower structure correspond to the sloped walls of the notch.

The central and southwest portions of the study area exhibit more complexities, as the bathymetric low broadens and splits into several parallel depressions (Figure 3.3c). Shallow, vertical faults are still evident, but are less continuous and not as linear along strike. Shallow packages of sediments, similar in seismic reflection character to those of the adjacent Kumano Basin, are found to the northwest, between several of these faults.

## **DISCUSSION:**

Several origins are feasible for a shelf edge bathymetric low like the notch, including submarine channel incision, surface expression of underlying splay fault geometry, and partitioned margin-parallel strain. Each of these processes would lead to different bathymetric signatures and patterns of subsurface deformation, potentially including gravitational normal faults, fault bend folds and translational faulting. Submarine channel incision is unlikely as an independent cause because of the notch

feature's rough bathymetry, size of the depression, and lack of channel fill through most of our dataset. The correspondence of bathymetric features to subsurface faults instead indicates a structural control. We believe the observed bathymetric notch is most likely the surface expression of KBEFZ. What then controls the formation of the KBEFZ and how important is this fault zone in the mechanics of the system as a whole?

We consider first the possibility that the KBEFZ is simply a system of gravitationally driven faults due to bathymetry. In deepwater anticlines, swarms of normal faults on the scale of 100s of meters have been observed and attributed to gravitational collapse on the flanks of bathymetric highs created by the anticlines [Morley, 2007]. However, this mechanism would require the creation of a significant bathymetric low on the edge of the Kumano Basin through some means independent of the normal faulting. We find no evidence of coherent anticlinal folding in the sediments beneath either side of the notch. Nor is there evidence of uplift along the entire edge of the basin independent of the splay fault which daylights farther seaward. Movement along the splay fault would cause uplift in the entire area, not a narrow ridge and trough. A stronger case can be made for the normal faults that we have mapped being the structural cause of the notch feature rather than a result of it. Also, the mechanism of gravitational normal faulting cannot explain the occurrence of vertical faults at the center of the bathymetric low. These faults are instead consistent with transform motion across our entire study area.

#### **Effect of underlying splay fault:**

The angle of the megasplay fault varies both along strike and down dip. Pangborn (2007) has mapped the uppermost fault segment within the splay fault system beneath our study area. Both this splay and the ones beneath it [G F Moore *et al.*, 2007] exhibit a

corkscrew geometry, twisting down to the southwest as they diverge from one another (Figure 3.4). Thrusting along this spiraling fault during co-seismic or inter-seismic shortening would cause greater uplift to the northeast and relatively less to the southwest, skewing the hanging wall(s) of the fault(s). The faults of the megasplay system all converge to a relatively flat décollement at depth [Pangborn, 2007], and therefore significant differential motion along strike should be limited to the seaward portion of the splays themselves. This geometry could create a left or right lateral sense of motion in the overriding sediments. Normal faulting and deformation as well as slumping oblique to the trench-axis direction are possible.

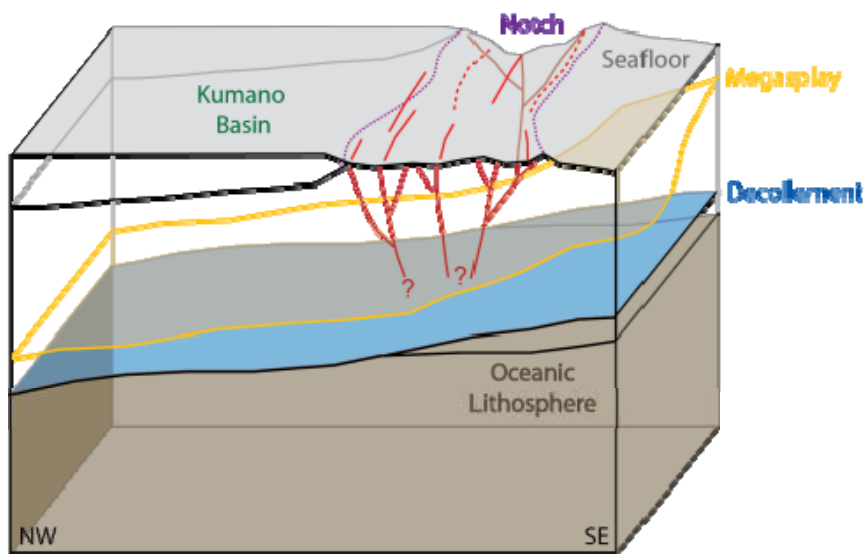


Figure 3.4: Block diagram of KBEFZ (“notch”) and surroundings. Note the corkscrew geometry of the megasplay fault, which twists up to the northeast within the 3d seismic dataset.

Fault-bend folding associated with changes in underlying fault dip with depth could cause a trench-parallel depression, but would not account for the steepness of the sidewalls without much sharper bends in the underlying splay fault. Along-strike variations in the fault bends (such as the 'lateral ramp' observed by *Moore et al.*, 2007) could cause local strike-slip features on a scale similar to the wavelength of the variations. However, this wavelength is only about 8 km within the region imaged by the 3D seismic data set, while the bathymetric notch extends laterally over 100 km at a consistent strike near 235°. We therefore conclude that the linear depression is too extensive to have been caused by variations in the geometry of the underlying splay fault.

While another cause must be found for the notch as a whole, the changes in splay fault geometry on a ~10 km scale may explain similar wavelength variations in the geometry of the notch or complexities in the KBEFZ. The depression extends over 100 km with a consistent strike, but its depth and width are somewhat variable. The portion of the feature imaged by the 3D seismic dataset is 750 m deep and 3 km across in the northeast and splits to the southwest into several parallel ~250 m deep depressions across a zone of deformation approximately 5 km wide. The steepening of the splay fault to the northeast of the imaged section may contribute to the narrowing and deepening of the depression as the fault bend flexes the overlying sediments. Proof or disproof of this contribution is hampered by the lack of deformation rate information available in the seismic data and the disruption of the sedimentary sequences, which makes offset distances impossible to measure.

### **Strain Partitioning:**

The oblique convergence direction, the existence of a major strike-slip fault beneath the arc and the orientation of the KBEFZ parallel to the trench all support the hypothesis of strain partitioning. The location of this potentially structural feature along the seaward edge of the forearc basin is reminiscent of the locations of the Andaman and Mentawi faults (Figure 3.5), although the distance from the trench is only ~30 km instead of 100-200 km as in the case of the strike-slip faults off Sumatra [*Mosher et al.*, 2008]. The Sumatra subduction zone is the type example of strain partitioning in an obliquely convergent setting [*Fitch*, 1972]. Near the island of Sumatra, a convergence vector that ranges between 60 and 87 degrees from perpendicular is accommodated by normal convergence on the megathrust of ~45mm/yr and right lateral strike-slip along the Sumatra fault of 11-48mm/yr [*McCaffrey et al.*, 2000; *Subarya et al.*, 2006]. Significant motion along the trench-parallel, strike-slip Sumatra fault and earthquake slip vectors perpendicular to the trench on the main subduction thrust, are both necessary to accommodate the oblique convergence of the Indian and Eurasian plates. The original model by *Fitch* [1972] called for complete partitioning of trench-parallel and trench-perpendicular strain into separate discrete faults. Subsequent studies along other margins [*McCaffrey*, 1993] suggest that a different partitioned strain regime is possible, in which trench-parallel motion is accommodated by distributed deformation within the forearc instead of by a single strike-slip fault.

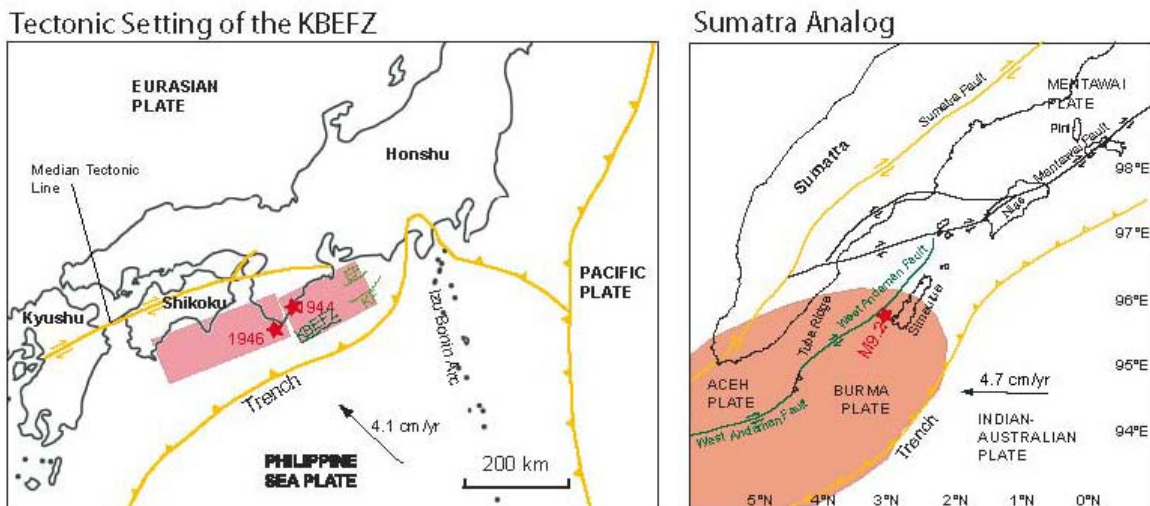


Figure 3.5: Tectonic setting comparison between Nankai and Sumatra. Major earthquake epicenters and approximate rupture areas are in red. In Sumatra [diagram modified from *Mosher et al., 2008*], strike-slip faults are found within the volcanic arc (the Sumatra Fault) and along the seaward edge of the forearc basins (West Andaman and Mentawi Faults). Oblique convergence along the margin is partitioned between these strike-slip faults and the megathrust. In Japan, the Median Tectonic Line (MTL) is a strike-slip fault within the volcanic arc and the KBEFZ is a strike-slip fault along the seaward edge of the forearc basin. The Enshu and Kodaiba Faults (EF and KF respectively) are the main strike-slip faults to the northeast associated with subduction of the Izu-Bonin ridge. Oblique strain is known to be partitioned between the MTL and the megasplay fault system. Could the KBEFZ be further evidence of partitioned strain localizing in the forearc?

Other major, margin-parallel fault systems are apparent within the Sumatra margin, namely the offshore Andaman and Mentawi systems [*Malod and Kemal, 1996; Samuel and Harbury, 1996*]. These faults occur closer to the deformation front, just seaward of a series of forearc basins, but are still landward of most subduction-related compressional features that produce seafloor topography [*Henstock et al., 2006*]. Recent high-resolution seismic reflection data found near-vertical and undulating fault strands on

the seaward edge of the Aceh basin, believed to be strands of the West Andaman fault system [Mosher *et al.*, 2008]. This observation combined with the geometry of Tuba Ridge, believed to be a pop-up structure, suggest that the West Andaman fault is a right-lateral strike-slip fault with a restraining bend at Tuba Ridge. Although the nature of the Mentawi fault system farther south is debated [Diament *et al.*, 1992; Malod and Kemal, 1996], high-resolution seismic data over that area might also suggest strike-slip motion. The existence of both onshore and offshore strike-slip faults implies a more complex system of strain partitioning, where trench-parallel motion can be accommodated in multiple localities within the forearc. Distribution of trench-parallel deformation between several faults both within the forearc and near the arc itself would suggest a regime between the two theoretical end members of purely localized and entirely diffuse strain partitioning.

Considering the convergence vector in Nankai, the trench-parallel component of motion should be right-lateral. Motion along the Median Tectonic Line is known to be right lateral [Nishimura and Hashimoto, 2006], consistent with partitioning of the strain caused by the obliquity of convergence (Figure 3.5). If the KBEFZ is also a right-lateral transform system, it must accommodate some portion of the trench-parallel motion on the margin.

The disruption of sediments in the KBEFZ makes direct observation of offset along most of the faults impossible. Instead we must look to the overall geometry of the feature, which makes a slight bend within the bounds of the data volume. To the southwest, the mapped faults and the axis of the bathymetric low strike ~10 degrees more northerly than those observed in the northeastern portion of the seismic data set. Northeast of the study area, the notch feature broadens and a single axis is difficult to trace. Right-lateral motion parallel to the southern portion of the KBEFZ would make this

bend to the east a releasing bend, explaining our observed increase in extension and prevalence of normal faulting to the northeast.

**Implications:**

The existence of partitioned strain in the Nankai margin is not an altogether unique idea. The collision of the Izu Bonin arc with the subduction zone in the Tokai area results in a complex system of both thrust and strike-slip faults throughout the area [Huchon *et al.*, 1998]. Convergence is distributed seaward as well as landward of the trough, implying overall deformation of the down going Philippine Sea Plate. The complexity of this region makes it difficult to differentiate strain due to strain-partitioning from strain caused by the effects of arc collision. Faults with potential translational components found in eastern Nankai generally die out around  $33^{\circ} 30'$ . The KBEFZ to the southwest, in contrast, provides an example of a single translational fault complex along a more laterally consistent portion of the trench without the added intricacy of faulting associated with an arc collision.

The potential strain partitioning we observe along the edge of the forearc Kumano Basin, is on a much smaller scale than the strain partitioning observed on the Sumatran margin with its greater obliquity. The observed notch feature exhibits greater symmetry in bathymetric relief than the surface expression of the Andaman and/or Mentawi faults. Laterally, the KBEFZ does not extend as far as the Andaman or Mentawi fault systems, implying a smaller scale instance of strain partitioning than previously observed. Southwest of our study area the trench bends immediately to the west and then gradually to the south as it passes Shikoku and Kyushu. A number of studies [Bangs *et al.*, 2006; Gulick *et al.*, 2004] off these islands, including one 3d seismic survey off the Muroto Peninsula on the same scale as our data, show no indication of strike-slip features. We

believe the change in trench strike along this portion of the margin has decreased the obliquity to the point such structures are not required.

We suggest location of the KBEFZ in the hanging wall of the megathrust splay system in Nankai also likely precludes this strike-slip fault from extending to depths similar to those suggested for the Andaman and Mentawi faults [*Malod and Kemal, 1996; Mosher et al., 2008*]. The interaction of the megasplay and the KBEFZ is not well imaged in our data due to problems with resolution at depth below the notch bathymetric feature. If the strike-slip fault(s) cut the megasplay, we could cast doubt on the role of the megasplay in recent seismogenic events. However, given the low magnitude of obliquity, overall translational motion expressed on the KBEFZ and Median Tectonic Line should be dramatically less than the associated compressional motion expressed on the megathrust and megasplay fault. Between this consideration and the scale of the megasplay, which extends to the décollement at depth and covers more of the margin along strike than the KBEFZ, we find it likely that the megasplay accommodates more total motion than the KBEFZ. Therefore our mapped faults probable either sole into or are cut by the megasplay at depth.

The mechanics of strain partitioning in subduction settings are not fully understood. Localization of different components of strain may be the result of variations in coupling between the dipping oceanic slab and the upper plate lithosphere [*Jarrard, 1986; Malod and Kemal, 1996; Manaker et al., 2008*]. Alternatively, variations in material properties within the accretionary prism have been suggested to constrain the updip extent of a seismogenic zone [*Fuller et al., 2006; Wang and Hu, 2006*]. This edge of the seismogenic zone is frequently located at the seaward limit of the forearc basins [*Song and Simons, 2003; Wells et al., 2003*], where the rheology of the accretionary wedge transitions to weaker materials. Such a change in rheology could cause shear strain

to localize on the edge of relatively strong zones, implying a preferential location of strain partitioning structures along the seaward edge of forearc basins. Margin-parallel, strike-slip faults along volcanic arcs are similarly thought to form due to the area's relative crustal weakness, which is caused by thermal softening from the underlying mantle wedge [Fitch, 1972].

With a portion of the megathrust or décollement locked, trench-parallel forces may be released on vertical transform faults in particularly weak zones at stress levels below those required to rupture the décollement [Jarrard, 1986]. With weaker faults accommodating the trench-parallel shear component of strain, the seismogenic portion of the décollement has only the convergent strain to accommodate. This mechanical idea implies that every seismogenic subduction zone with oblique convergence should exhibit some degree of strain partitioning. Thus, an understanding of the particular distribution of partitioned strain is important to the understanding of subduction zone dynamics and our results show a likely candidate for one localization of this strain is along the seaward edge of forearc basins.

IODP Expedition 314 conducted logging-while-drilling operations along a transect within the 3D seismic dataset as part of the NanTroSEIZE project [Kinoshita *et al.*, 2007]. Ongoing analysis of observed fractures and borehole breakouts by members of the science party has constrained the state of stress, which varies markedly on either side of the notch. A distinct change in stress orientation has been noted across the KBEFZ, from the trenchward side which exhibits a maximum principle stress orientation perpendicular to the trench, to the landward side which exhibits a maximum principle stress orientation subparallel to the trench [Kinoshita *et al.*, 2009]. Such a change in stress orientation over only a few kilometers is consistent with crossing a significant fault system. As they are combined with stress states estimated from ongoing core analysis,

these changes in stress orientation will become important to models of prism and basin formation. The presence and geometry of the KBEFZ should be considered as a significant constraint in attempts to model the change in stress state between the basin and the prism slope. In particular, the out-of-plane motion indicated by translational movement along the KBEFZ calls for three-dimensional modeling when attempting to explain the change in stress state between drilling sites.

#### **CONCLUSIONS:**

The geometry of faulting within the KBEFZ implies a dominantly strike-slip deformation regime. Based on an apparent releasing bend, we believe the sense of motion to be right lateral, which is consistent with the direction of obliquity of motion on the margin as a whole and implies that the KBEFZ is accommodating one component of the total strain. Localization of partitioned margin-parallel strain is therefore observed in two places within the Nankai margin: the KBEFZ and the Median Tectonic Line.

The evidence for strain partitioning seaward of the forearc basin in the Kii Peninsula region of Japan as well as previously reported case of Sumatra implies that localization of strike-slip deformation within the forearc is likely to occur in other oblique margins as well. Extreme obliquity, as observed in Sumatra, is apparently not required to create multiple localities of localized, margin-parallel strain. In addition, transform faults that accommodate the margin-parallel component of strain may not require a zone of notable weakness (such as that below the arc) to form. Instead, zones of significant contrast in strength or deformation style within the wedge or along the décollement may allow trench-parallel strain to localize. Whether the forearc basin is stabilized by wedge strength or décollement properties, it does not deform as extensively

internally as the imbricate thrust faulted zones present in outer parts of accretionary prisms. Therefore the strain that could be accommodated diffusely within the span of the basin will instead be localized adjacent to it. Systems created by partitioned strain in convergent margins are thus more complicated than the early models of *Fitch* [1972] and *Jarrard* [1986], with the possibility of several transform faults and shear zones within a single margin that collectively accommodate the margin-parallel component of partitioned strain.

In addition, the existence of a strike-slip feature along the edge of the forearc basin is important for understanding and contextualizing ongoing work in the Nankai subduction zone. The observed stress states in the NanTroSEIZE boreholes give an idea of how the stress field may vary along dip in a convergent margin. Modeling these changes in stress could lead to a better understanding of the changes in rheology and fault frictional properties along dip within both the Nankai region and subduction zones in general. However, attempts to explain the observed stress field changes between the Kumano Basin and the forearc slope should take into account the presence of the Kumano Basin Edge Fault Zone.

## **Chapter 4: The West Andaman Fault as strike-slip, strain-partitioning feature at the edge of the Aceh Basin**

### **ABSTRACT**

Along the Sumatran subduction zone, oblique strain is partitioned between the Sunda megathrust and the strike-slip Sumatran Fault located along the volcanic arc. Additional strike-slip motion may be localized adjacent to the forearc basin system, forming the Mentawai and West Andaman Fault Zones. An alternative interpretation of the West Andaman Fault Zone, as primarily a backthrust, has also been proposed.

We combine profiles from a 2D multichannel seismic (MCS) survey (SUMUT) with previous bathymetry and MCS surveys to characterize the West Andaman Fault Zone adjacent to the Aceh forearc Basin. Pre-stack time migration of SUMUT profiles provides the clearest images to date of this portion of the West Andaman Fault Zone. In these images we interpret inward-dipping fault segments along the West Andaman Fault Zone indicative of a transpressional flower structure. A reflector at the base of the Aceh Basin sediments appears to continue trenchward of the Fault Zone for >15 km and was interpreted previously as a regional-scale Oligocene/early Miocene unconformity. Within the Fault Zone this reflector is disrupted, with some segments raised and some lowered. The geometry of this reflector further seaward is inconsistent with the geometry we would expect if a major backthrust were to daylight at the edge of the basin. Based on this observation and the configuration of faults in a flower structure, we conclude that the West Andaman Fault Zone where imaged is predominantly strike-slip in nature. As such, the West Andaman is likely part of a system of faults including the Sumatra Fault that accommodate the significant shear component of strain in this oblique subduction zone.

Additionally, the location of the West Andaman Fault within the forearc may be controlled by the rheologic contrast between the marginal plateau and the forearc basin.

## INTRODUCTION

The Sumatran subduction zone has been used as the type example of strain partitioning since Fitch [1972] first identified the partitioning of the oblique convergence between slip on the main thrust fault and slip on the strike-slip Sumatran Fault (Figure 4.1). Despite this significance, the Sumatran subduction zone had received somewhat less scientific attention than subduction zones near more developed countries like the United States and Japan until the great (M9.2) Sumatra-Andaman earthquake and resultant Indian Ocean tsunami of December 26, 2004. This disaster forced scientists to recognize the need for study of this margin's structure and dynamics in order to recognize and mitigate future earthquake-related hazards.

To that end, a number of geophysical surveys have been conducted offshore northern Sumatra since the beginning of 2005. High-resolution bathymetry across the trench and forearc were collected as early as January 2005 by the HMS Scott, a British Royal Navy vessel [Henstock *et al.*, 2006]. In May 2005, the Sumatra Earthquake and Tsunami Offshore Survey (SEATOS) utilized this bathymetry to guide acquisition of a high-resolution single-channel seismic survey and remote-operated vehicle observations and sampling [Fisher *et al.*, 2007; Moran and Tappin, 2006; Mosher *et al.*, 2008]. To the south, studies of corals on the forearc islands have revealed information about forearc deformation in the area of the 2005 M8.6 earthquake and the boundary between the 2004 and 2005 events [e.g. Meltzner *et al.*, 2006]. Finally, within the 2004 and 2005 rupture areas, several groups have acquired deep-penetration seismic data from the trench, across

the prism, to the forearc basin [*Berglar et al.*, 2010; *Dean et al.*, 2010; *Gulick et al.*, 2011; *Seeber et al.*, 2007; *Singh et al.*, 2011].

In this study we use such seismic data to focus on the role of the West Andaman Fault (WAF) in the kinematics of the forearc to the west of northern Sumatra. We utilize both new and published seismic data complemented by bathymetry to examine the WAF in three dimensions along the western edge of the Aceh Basin and across the Tuba Ridge. We find that the WAF is a zone of transpressional faulting at the edge of the Aceh basin and the Tuba Ridge is a pop-up structure associated with a leftward step in this right-lateral strike-slip system. Strike-slip offset on the WAF is likely due to partitioned strain from the oblique convergence vector, providing evidence of partitioned strain localized in the forearc, rather than proximal to the arc.

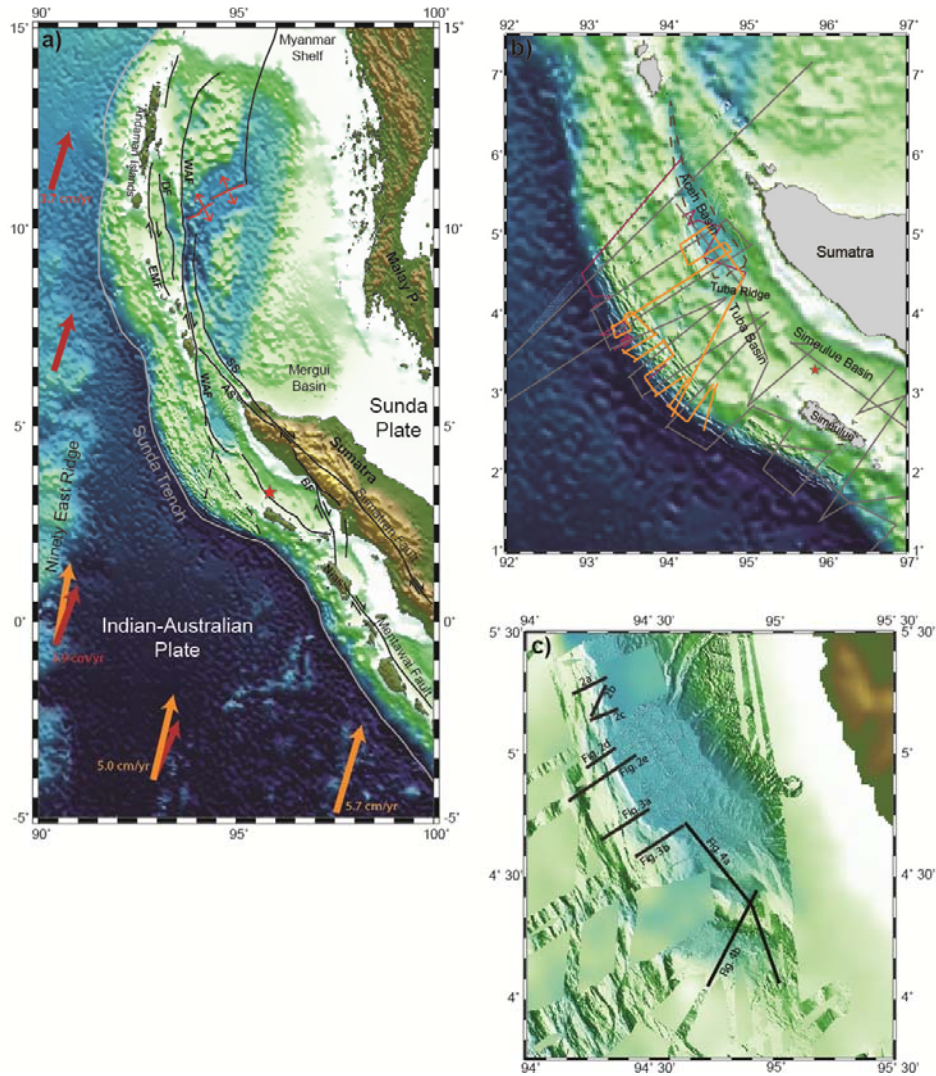


Figure 4.1: Maps of the Sunda Trench and forearc. Red stars are the epicenter of the 2004 Sumatra-Andaman earthquake. a) Regional tectonic setting. The boundary between Australia and India is a diffuse plate boundary between  $\sim 5^{\circ}$  S and  $\sim 8^{\circ}$  N [DeMets et al., 2005]. Plate velocities of Australia (orange arrows) and India (red arrows) relative to Sunda modified from Subarya et al. [2006]. Fault traces modified from Cochran et al., 2010 and McCaffrey et al., 2009: AS, Aceh Strand of the Sumatran Fault; BF, Batee Fault; DF, Diligent Fault; EMF, Eastern Margin Fault; SS, Seulimeum strand of the Sumatran Fault; WAF, West Andaman Fault. b) Map of the forearc offshore northern Sumatra showing the seismic surveys used in our analysis. SEATOS in pink, BGR06 in Gray and SUMUT in orange. c) Bathymetry of the central and southern Aceh Basin with locations of the seismic lines shown in Figures 2-4.

## TECTONIC SETTING

Offshore Sumatra the Indian-Australian Plate is subducting beneath the Eurasian plate at the Sunda Trench; specific kinematics, particularly along strike, are complex (Figure 4.1). Near the island of Java the convergence vector between the two plates is approximately perpendicular to the Trench at ~68 mm per year [DeMets *et al.*, 2010]. Due to the Trench curvature, the convergence becomes increasingly oblique to the north along Sumatra and the Nicobar and Andaman Islands. Offshore northern Sumatra estimates of the convergence vector range between 3.9 and 5.0 cm/year at an angle between 30° and 50° from trench-perpendicular [DeMets *et al.*, 2010; Subarya *et al.*, 2006].

Adding to this subduction complexity, the down-going Indian-Australia Plate is actually three separate plates, the Indian, Capricorn and Australian plates, separated by regions of convergent deformation [DeMets *et al.*, 2005; DeMets *et al.*, 2010]. The deforming region between the Capricorn and Indian plates is subducting in the region of northern Sumatra. Some deformation in the downgoing plate takes the form of left-lateral strike slip motion on north-northeast oriented near-vertical faults, thought to be fracture zones reactivated by northwest-southeast compression [Graindorge *et al.*, 2008; Rajendran *et al.*, 2011]. The convergence between the two down-going plates leads to as much as a centimeter per year of the uncertainty in the convergence vector at the Sunda Trench [McCaffrey, 2009].

The Eurasian Plate is also not one rigid body. The island of Sumatra is actually at the southwestern edge of the Sundaland Plate, which is moving approximately east at between a few millimeters and a centimeter per year relative to Eurasia [Simons *et al.*, 2007]. Therefore the subduction vector between the downgoing plate(s) and the Sundaland Plate is somewhat less than would be measured relative to Eurasia.

The strike-slip Sumatran Fault, which runs down the middle of the island of Sumatra, following the trend of volcanic arc (Figure 4.1a), separates the forearc to the west from the rest of the Sundaland Plate to the east [Simons *et al.*, 2007]. Fitch [1972] first noted that the motion on the Sumatran Fault is right-lateral, consistent with the obliquity of convergence along the margin, and hypothesized that the oblique convergence was being partitioned between the plate boundary thrust and the strike-slip Sumatran Fault. The section of the forearc between these two faults is a forearc sliver or sliver plate [e.g. Fitch, 1972; Jarrard, 1986]. This forearc sliver is essentially dragged along strike relative to the overriding plate, while the downgoing plate subducts beneath it. As a result, the motion on the plate boundary thrust, as shown by earthquake mechanisms beneath the forearc, is generally perpendicular to the trench [e.g. McCaffrey, 1991].

The forearc sliver offshore Sumatra exhibits additional internal deformation. Increasing motion to the north on the Sumatran Fault associated with increasing obliquity, requires stretching of the forearc along strike [McCaffrey, 1991; 2009]. Arc-parallel faults have also been observed separating the outer high from the forearc trough and the forearc basins [Diament *et al.*, 1992; Malod and Kemal, 1996; Samuel and Harbury, 1996]. From south of Sumatra to south of Nias, the Mentawai Fault is one of these arc-parallel features in the forearc (Figure 4.1a). The sense of motion on the Mentawai Fault has been debated for some time using various forms of geophysical data. Karig *et al.* [1979] interpreted it as a flexural bulge or backthrust, but Diament *et al.* [1992] suggested instead active strike-slip motion along the Mentawai, connecting with the Batee Fault north of Nias. Malod and Kemal [1996] found the Mentawai to be linear with apparent flower structures in places, implying that it is a strike-slip fault that has also accommodated some shortening. However, recent deep-penetration multichannel

seismic and OBS survey data have been used to imply that the Mentawai Fault is a large-scale backthrust associated with a continental backstop beneath the forearc basins [Singh *et al.*, 2010].

Farther north, in the Aceh region of the Sumatran forearc, the West Andaman Fault separates the outer arc high from the Aceh Basin (Figure 4.1a,b). This fault extends northwards past the eastern side of Great Nicobar Island ( $\sim 7^\circ$  N) where it is joined by the Aceh strand of the Sumatran Fault [Cochran, 2010]. North of this intersection, the West Andaman Fault is the most prominent morphologic feature in the Andaman Sea, running linearly along the eastern edge of several forearc basins and dividing the region into a shallower forearc and a deeper backarc region. This position is reminiscent of the Sumatran Fault to the south, but without the well-developed island arc. Like the Sumatran Fault, the northern portion of the West Andaman Fault is thought to be strike-slip in nature [e.g. Cochran, 2010; Curray, 2005]. Our focus is on the southern portion of the West Andaman Fault, where it strikes obliquely to the volcanic arc and trends to the west (seaward) of the Aceh forearc basin. In this area, like the Mentawai Fault, the West Andaman Fault has been classified alternately as strike-slip [e.g. Berglar *et al.*, 2010; Seeber *et al.*, 2007] or thrust [Chauhan *et al.*, 2009; Singh *et al.*, 2011]. The goal of this study is to discern which of these competing hypotheses is supported by a series of multichannel and single channel seismic profiles and an integrated grid of multibeam bathymetry data.

## STUDY AREA/PREVIOUS WORK

### Aceh Basin

The Aceh Basin is the northernmost and deepest of several distinct basins that make up a forearc trough between the forearc high and continental slope offshore Sumatra (Figure 4.1a). This Basin is roughly triangular in shape, narrowing to the north, and bounded by the West Andaman Fault to the west. To the east, the Basin is bounded by the inner slope and the island of Sumatra, except in the section offshore the northern tip of Sumatra, where the Basin is bounded by the Sumatran Fault zone [Berglar *et al.*, 2010]. The seafloor within the Aceh Basin is roughly 2700m below sea level and remarkably flat, usually dipping between 0 and 0.25 degrees to the southwest [Seeber *et al.*, 2007]. The deepest portions of the basin floor and the thickest basin sediments are to the west-southwest and lie within the highest slip region of the 2004 Great Andaman Earthquake [Ishii *et al.*, 2005].

Within the Aceh Basin, Berglar *et al.* [2010] define two major unconformities (Figure 4.2a). The basal unconformity (Labeled A1 in Figures 4.2-4.6), also recognized by Seeber *et al.* [2007] and Mosher *et al.* [2008], is at the base of the well-stratified sediments and is of regional extent. Berglar *et al.* interpret this unconformity as having formed due to uplift and erosion of the forearc area off Sumatra and associate it with a similar unconformity found in all forearc basins offshore Sumatra. In the nearby Simeulue Basin and other basins to the south, drilling places the age of this unconformity as base Neogene [Beaudry and Moore, 1985; Karig *et al.*, 1979; Karig *et al.*, 1980; van der Werff, 1996]. Seeber *et al.* compare the Aceh Basin structure with that of the Sunda forearc offshore southern Sumatra to conclude that the basal unconformity (acoustic basement in single channel seismic profiles) beneath the Aceh Basin is likely to be pre-

orogenic and therefore older than the syn-tectonic terrane southwest of the West Andaman Fault.

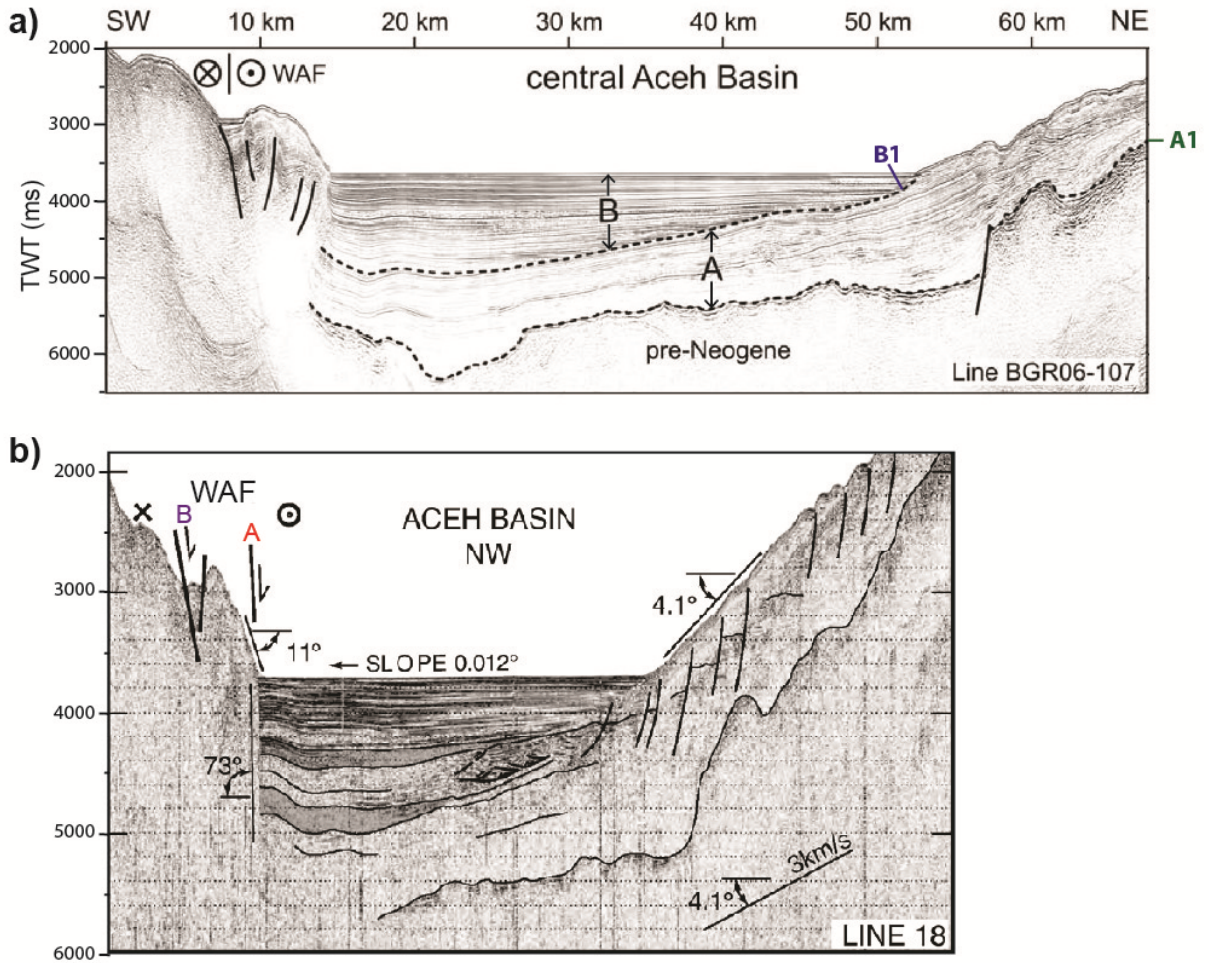


Figure 4.2: Previous interpretations of the Aceh Basin. West Andaman Fault Zone (WAF). a) BGR06-107, modified from Berglar et al. [2010]. b) Profile 18 from Seeber et al. [2007]

The second unconformity (B1 in Figures 4.2-4.5) identified by Berglar et al. is an angular unconformity that separates two well-layered sedimentary sequences, designated A and B. Deformation of basin sediments increases with depth, with evidence of faulting largely confined to the deeper packages (Sequence A) [Berglar et al., 2010; Mosher et al., 2008; Seeber et al., 2007]. Sequence A is relatively more transparent than the overlying Sequence B (Figure 4.2a), though this contrast may be due in part to less acoustic energy penetrating below Sequence B rather than a simple decrease in acoustic impedance [Mosher et al., 2008].

Moore et al. [1982] found that the lack of major fan deposits, flatness of the basin seafloor and configuration of acoustically layered deposits suggested that deposition has occurred through turbidity currents and earthquake-induced sedimentation events, including both turbidity currents and other types of mass transport deposits. Single channel seismic has since shown mass transport deposits from the eastern side of the basin both in the north [Mosher et al., 2008] and in the south [Seeber et al., 2007]. Seeber et al. particularly note normal faults on the eastern slope dipping into the Basin (Figure 4.2b). Slides several hundred meters thick occur in the upper portion of Sequence A in the northeastern part of the basin (Unit 3 in Mosher et al.). The overlying mass transport deposits comprising the overlying Sequence B (Unit 4 in Mosher et al.) are significantly thinner, from less than 100m thick down to the limit of seismic resolution.

### **West Andaman Fault**

Seeber et al. [2007] used a single channel seismic survey to analyze an ~20 km section of the WAF zone just south of 5° N (example line in Figure 4.2b). They identified two branches of the WAF in this area: a near-vertical fault at the basin edge (designated Fault A1 in Table 4.1) and a flower structure (Group B) comprised of several fault traces beneath the narrow linear basin 6-7 km to the southwest of the Aceh Basin. Fault A1 was

interpreted as predominately strike slip, with some dip-slip motion compatible with subsidence of the forearc trough. The faults of the flower structure (Group B) join up at a depth of ~2km in this area and at the seafloor north of 5° N. Seeber et al. hypothesize that the two branches converge at depth in this region, but bifurcate to the south, with the western branch extending south-southeast oblique to the trench.

Table 4.1: Calculated dips of interpreted faults in Figures 4.3-4.6.

Group (#)	Survey	Line	Dip	Group (#)	Survey	Line	Dip
A (1)	SUMUT	03	61 ° W	D	SUMUT	03	8 ° W
A (1)	BGR06	107	44 ° W	D	SUMUT	03	18 ° W
A (1)	BGR06	107	53 ° W	D	SUMUT	03	17 ° W
A (1)	SUMUT	05	59 ° W	D	SUMUT	03	25 ° W
B	SUMUT	03	77 ° E	D	BGR06	107	12 ° W
B	BGR06	107	32 ° E	D	BGR06	107	15 ° W
B	SUMUT	05	52 ° E	D	BGR06	107	8 ° W
B	SUMUT	07	24 ° E	D	BGR06	107	12 ° W
C	SUMUT	03	74 ° E	D	SUMUT	05	25 ° W
C	BGR06	107	82 ° W	D	SUMUT	05	14 ° W
C	BGR06	107	77 ° E	D	SUMUT	07	30 ° W
C	SUMUT	05	74 ° E	D	SUMUT	07	21 ° W
C	SUMUT	05	75 ° W	E	SUMUT	03	43 ° E
C	SUMUT	05	88 ° E	E	SUMUT	03	41 ° E
C	SUMUT	05	89 ° E	E	BGR06	107	20 ° E
C	SUMUT	07	25 ° E	E	BGR06	107	44 ° E
C	SUMUT	07	44 ° E	T (1)	SUMUT	01	34 ° SW
C	SUMUT	07	55 ° E	T (2)	SUMUT	01	66 ° NE
				T (3)	SUMUT	01	70 ° NE
				T (1)	BGR06	144	32 ° SW
				T (2)	BGR06	143	72 ° NE
				T (3)	BGR06	143	48 ° NE

Berglar et al. [2010], utilized deeper-penetration multi-channel seismic data to study the forearc basin area from 2 to 7° N. They identify the WAF as a linear feature coincident with the edge of the Aceh Basin, consisting of one main fault strand surrounded by several subordinate fault strands imaged mainly as anticlines (Figure 4.2a). These subordinate strands branch off both into the forearc basin and the forearc high. The main strand identified by Berglar et al. underlies the narrow linear basin described by Seeber et al., and is labeled in our figures as Group B. Both Berglar et al. and Seeber et al. interpret a strand of the WAF trending more to the south on the west side of the Tuba Basin, although in Berglar et al. this feature strikes south-southwest in contrast to Seeber et al. who interpret the trend as south-southeast. Both trends are shown as dashed lines to the west of the Tuba Basin in Figure 4.1a.

### **Tuba Ridge and Tuba Basin**

Berglar et al. [2010] also present seismic images of the Tuba Ridge and Tuba Basin. The Tuba Ridge (Figure 4.1b,c) is an anticlinal feature cut by relatively steep faults that separates the Aceh Basin from the Tuba Basin. No horizons are reliably traceable across this Ridge, but Berglar et al. use the seismic character of the sediments to correlate units within the Tuba Basin with those in the Aceh Basin, extending both regional unconformities (A1 and B1) into the Tuba Basin. The Tuba Ridge connects the WAF to the north with a fault to the southeast that runs along the basinward side of Simeulue (Figure 4.1a). The Ridge is interpreted as a pop up structure associated with a leftward step in a right-lateral strike-slip system [Berglar et al., 2010; Mosher et al., 2008].

## DATA

In this study we combine data from several previous bathymetry and seismic surveys with the SUMUT multi-channel seismic (MCS) survey acquired on cruise SO-198b (Figure 4.1b). The SUMUT 2D seismic survey is comprised of 1,250 km of multichannel seismic data acquired aboard the R/V Sonne in the summer of 2008 (Figure 4.1b). The source array consisted of 12 G-guns with a total volume of 5,420 cu. in. A 2.4 km hydrophone streamer with 192 channels recorded 16 s of the reflected subsurface arrivals with a 2 ms sampling interval.

Pre-stack processing included resampling to 4 ms, exclusion of channel 192 due to tail buoy noise, minimum phase trapezoidal band pass filter (3-6-60-80 Hz) and amplitude recovery ( $1/t^2$ ). We applied a multichannel predictive deconvolution with a 300ms operator based on a 3 s design window starting just below the seafloor. Shot gathers revealed significant swell noise which translated to intermittent high amplitude noise in the CDP gathers. We therefore applied time-frequency noise suppression before velocity analysis and a normal moveout correction. We then used a median stack with a 20% trim rate to minimize the effect of remaining swell noise followed by a Kirchhoff time-space migration. The resultant subsurface images were published in part by Gulick et al. [2011], who discussed the influence of thick, lithified, incoming sediments on the structure of the accretionary prism and the updip propagation of megathrust earthquake rupture. Additional details about this processing flow can be found in Appendix E.

We used these images to map horizons in the forearc basin and to select areas of faulting along the edge of the basin for further processing. Sections of lines SUMUT-01, -03, -05 and -07 where they cross the West Andaman Fault at the edge of the Aceh forearc basin (Figure 4.1c) were processed with the same pre-stack job flow as the full

survey (described above), but without amplitude recovery or normal moveout correction. We then performed a 2D Kirchhoff pre-stack time migration, calculating p-wave travel times by second order curve fitting using the velocity section picked in the initial round of processing above. We used residual moveout analysis to refine the velocity section before producing the final migrated sections presented in Figures 4.4-4.6. Additional details of the pre-stack time migration processing flow can be found in Appendix F.

This pre-stack time migration of SUMUT profiles provides the clearest images to date of the portion of the West Andaman Fault Zone along the central and southern Aceh Basin. We map the faults of the West Andaman Fault Zone in these images based on discontinuities in sedimentary horizons and occasional fault plane reflectors. The more steeply-dipping faults ( $>45^\circ$ ) do not exhibit fault plane reflections, but disrupt shallow sedimentary horizons and often offset the seafloor. Faults with shallower dips have been identified mostly from negative polarity fault plane reflections.

We also performed pre-stack depth migrations on select lines, but these images are not as clear as the time migrated sections. Outside of the basin, our velocity model is not well constrained, preventing significant improvements in the depth migrated section. Comparisons of select time and depth migrated sections are in Appendix G. We use the depth sections in these comparison figures to verify angles measured on the time migrated sections.

Complementing the SUMUT survey, we have two other seismic data sets. The BGR06 lines (grey lines in Figure 4.1b) are a subset of the multichannel seismic data acquired on the two SEACAUSE cruises aboard the RV Sonne in 2006, which were previously presented by Berglar et al. [2010]. The SEATOS single channel seismic lines (pink lines in Figure 4.1b) include six crossings of the seaward edge of the Aceh Basin [Moran and Tappin, 2006; Mosher et al., 2008]. We use these two surveys to correlate

fault and horizon interpretation between the SUMUT lines and extend our interpretation to the north and south.

A combined bathymetry grid (Figure 4.1c) allows us to extend our interpretation in three dimensions between our 2D seismic lines and to positively correlate from line to line faults that outcrop to the seafloor. This grid consists of the bathymetry collected during the SUMUT survey, combined with the grid from the German/Indonesian SEACAUSE and SUMATRA cruises [Berglar *et al.*, 2010; Franke *et al.*, 2008; Krabbenhoeft *et al.*, 2010] and a high resolution grid acquired by the HMS Scott in 2005 [Henstock *et al.*, 2006].

## **STRUCTURAL ANALYSIS**

Our analysis builds directly on the work of Seeber *et al.* [2007], Berglar *et al.* [2010], and Mosher *et al.* [2008]. We maintain and elaborate on the classification of sequences proposed by Berglar *et al.* (Figure 4.2a) and expand on the classification of faults in Seeber *et al.* (Figure 4.2b).

### **Aceh Basin**

The parallel-continuous reflectors of the Aceh Basin sediments allow us to see offsets related to the West Andaman Fault Zone (Figures 4.2-4.5). Interpreting these horizons within the basin provides the only relative timing constraints available from line to line. Our interpretation of the basin is preliminary and aimed primarily at providing these constraints. The SUMUT survey complements existing lines, making detailed interpretation and isopach maps possible, but that analysis is beyond the scope of this study.

### ***Basal Unconformity***

Coherent Aceh basin sediments extend ~2s two-way travel time below the seafloor in the north and thicken southward to ~3s just north of the Tuba Ridge. We define a distinct, regional unconformity (Surface A1) with undulating topography as the lower extent of these Aceh Basin-fill sediments. This angular unconformity is too deep to be imaged in some single channel lines (Figure 4.3), but appears in all multi-channel data (Figures 4.4-4.6) below the layered basin fill and produces a reflector with high-amplitude and lower frequency content which is recognized as acoustic basement by both Seeber et al. [2007] and Berglar et al. [2010] (Figure 4.2). Because no drilling has yet been done in the Aceh Basin, we lack direct evidence for the age of this basal unconformity, but Berglar et al. correlate this unconformity with a regional unconformity found in all forearc basins along the Sumatran Trench that has been dated as Oligocene to early Miocene in age (base Neogene).

Consistent with previous interpretations of the high amplitude reflector associated with this unconformity and the variable relief of the mapped surface, we suggest that it was indeed formed by uplift and subsequent erosion of the forearc area. However, our data show layered reflectors with varying degrees of deformation below the basal unconformity (for example, see the bottom right corner of Figure 4.4a), which prevent us from definitively identifying it as the base of all basin-fill sediments. By flattening this surface, we determine that the underlying reflectors form packages which are nearly parallel to the mapped unconformity in the central and eastern portions of the basin, raising the possibility that the sediments below this unconformity also formed in a basin of significant extent, similar to the current Aceh Basin. We therefore consider the basal unconformity to be the base of the modern Aceh Basin and leave the nature of underlying sediments for future consideration.

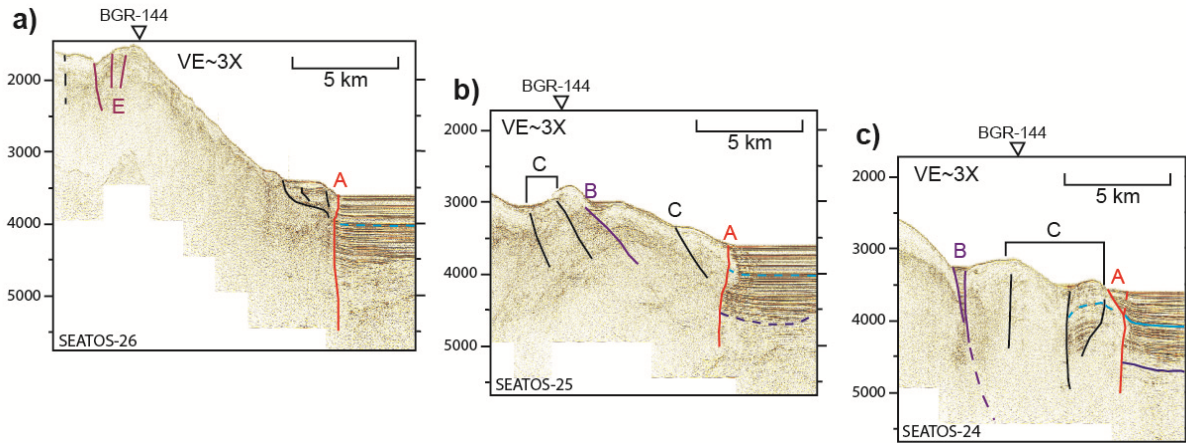


Figure 4.3: SEATOS lines crossing WAF in the northern part of the study area. Interpreted Sequence boundaries, marker horizons and faults, particularly steep basin-edge fault traces (Group A). Locations shown in Figure 1c. Line crossings indicated at the top of sections. a) SEATOS-26: Dipping Group E faults separated by a steep slope with possible slumps. b) SEATOS-25: Dipping Group B and C faults interspersed with anticlinal folds in former basin sediments. Surfaces B1 and B2 interpreted based on similarity of basin sediment reflectors to those in SEATOS-24 (c). c) SEATOS-24: Surfaces B1 and B2 show anticlinal folding in WAF (interpreted from line crossings between SEATOS, SUMUT and BGR surveys).

### ***Major Sequence Boundary***

Above the basal unconformity Berglar et al. [2010] identified two well-layered sedimentary sequences, designated A and B, divided by an angular unconformity (Surface B1 in Figure 4.2a). This unconformity corresponds to a prominent onlap surface identified by Mosher et al. [2008]. We map this angular unconformity across most of the basin. Overlying sediments onlap to the south and west, visible in both strike and dip lines. Although it is distinctly unconformable in the east (Figure 4.2a), this surface appears conformable on dip-lines in much of the central and western Basin (Figures 4.2-4.5). Unlike the basal unconformity, which deepens to the southwest, Surface B1 deepens

to the northwest of our study area (compare Figures 4.4 and 4.5). This pattern is consistent with a northward-migrating trend of subsidence over time [Berglar *et al.*, 2010].

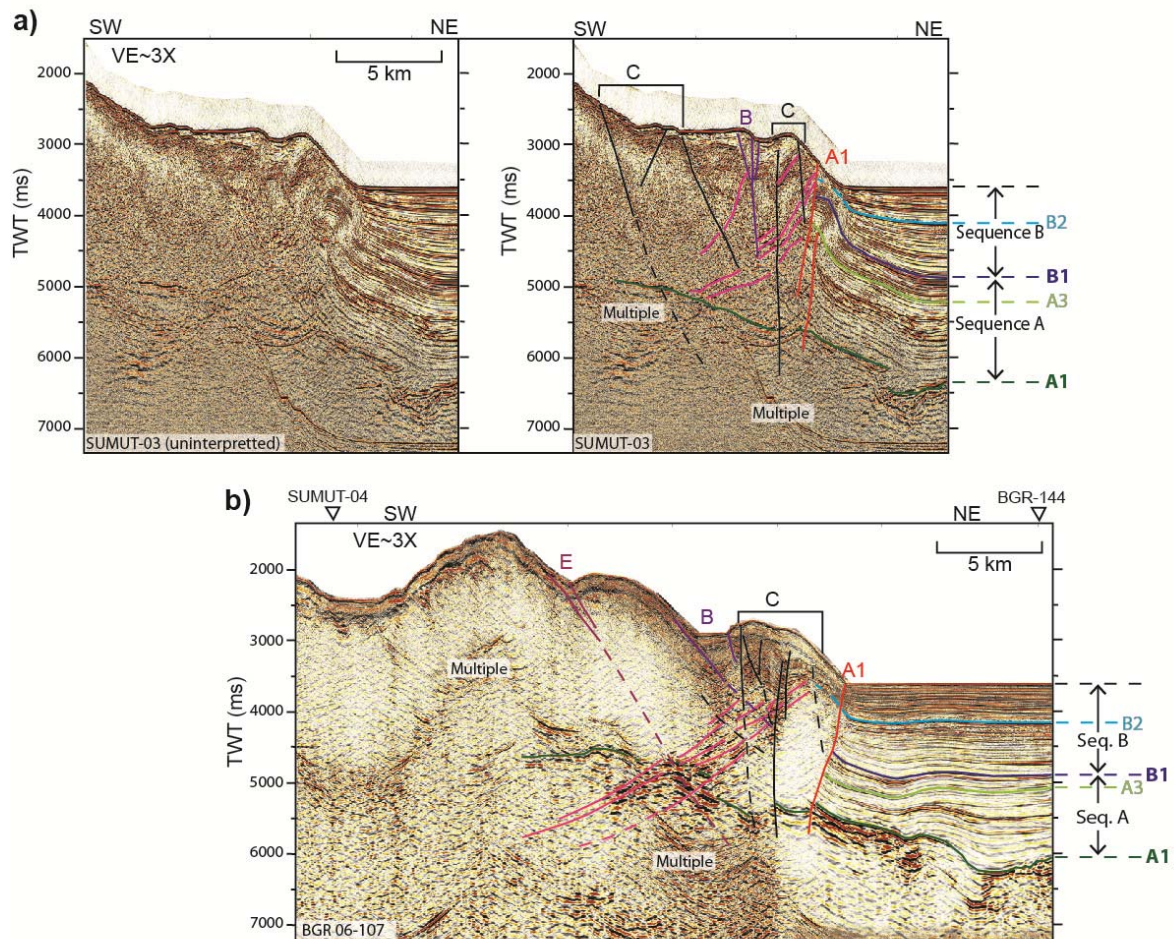


Figure 4.4: Multichannel seismic lines crossing the WAF in the northern part of the study area. a) Pre-stack migrated MCS section of SUMUT-03: uninterpreted on the left and interpreted on the right. Apparent flower structure (Groups A, B and C faults) cuts shallower-dipping thrust faults (Group D, shown in pink). b) Section of MCS line BGR06-107: [Berglar *et al.*, 2010], with additional interpretation. Features are similar to those interpreted on SUMUT-03, with the addition of Group E faults imaged to the west.

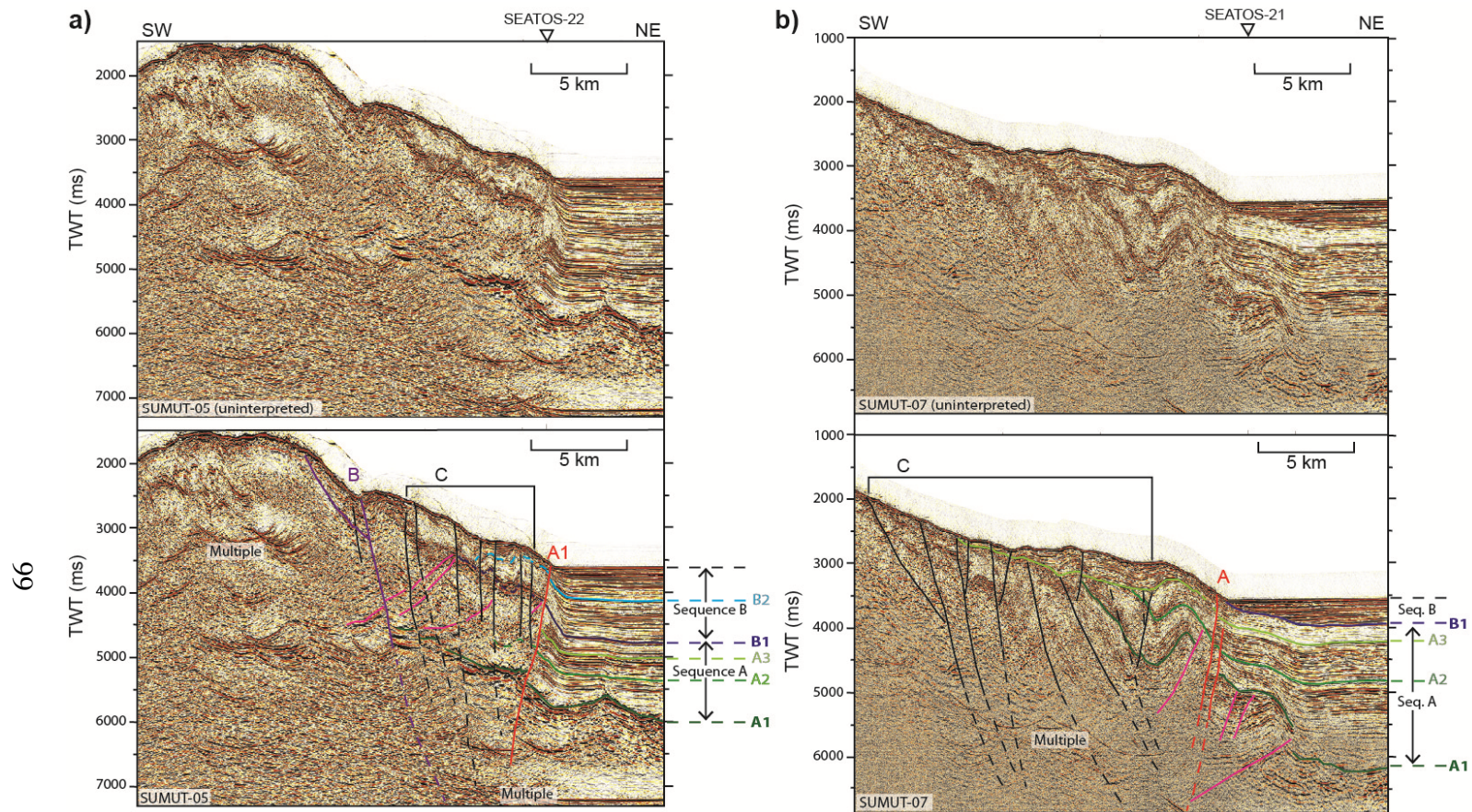


Figure 4.5: Seismic lines in the southern part of the Aceh Basin area. Uninterpreted sections above, interpreted sections below show Sequence boundaries, marker horizons and faults. Locations shown in Figure 1c. Line crossings indicated at the top of sections. VE~3X. a) Pre-stack migrated section of SUMUT-05: Group A, B and C faults form a flower structure offsetting Group D thrusts. b) Pre-stack migrated section of SUMUT-07: Wider zone of basin edge deformation than to the north. Steeply-dipping faults form an apparent flower structure, whereas thrust faults offset only the oldest basin sediments.

## *Sequence A*

Sequence A is the lower section of the Aceh Basin, between Surfaces A1 and B1 in the multichannel seismic images [Berglar *et al.*, 2010]. This Sequence corresponds to Units 2 and 3 as identified by Mosher *et al.* [2008]. Sequence A has a maximum thickness of 4 s TWT in the south, near Tuba Ridge (Figure 4.6), and thins to 1.4 s TWT in the north where it dips slightly trenchward (Figure 4.4a). In the south, Sequence A dips generally to the north but is characterized by several kilometer-scale anticlines, the largest of which is roughly 40 km long and strikes roughly east-west near the Tuba Ridge (Figure 4.6a). The lower portion of Sequence A (Unit 2 in Mosher *et al.*) is generally transparent on the single channel seismic lines (Figure 4.3a,b,c), but the multichannel lines (SUMUT and BGR surveys) show parallel reflectors within this unit. These reflectors onlap the uneven Surface A1 and are interrupted by Surface A1 highs (Figures 4.4 and 4.5).

The upper portion of Sequence A corresponds to Unit 3 in the interpretation of Mosher *et al.* [2008]. In the area of SUMUT-05 (Figure 4.5a) and SEATOS-22 (not pictured), this Unit is characterized by westward-dipping, gently folded beds and listric faults that sole into layer-parallel structures. In the north, the eastern end of SUMUT-03 (east of Figure 4.4a) confirms the interpretation by Seeber *et al.* [2007] of thrust faults and layer duplication near the downdip end of slides associated with up-dip normal faults (Figure 4.2b). The complexity within this portion of Sequence A makes tracing any unconformities or marker horizons across the entire Aceh Basin difficult. We identify two marker horizons, A2 and A3, within Sequence A in our figures (4.3-4.6). A2 is only mappable in the southern portion of the Basin, as it is disrupted by the complexities associated with the mass transport deposits in the north and east. A3 defines the bottom of a relatively translucent zone immediately below the sequence boundary B1, and is

mapped to most multichannel seismic lines (the SUMUT and BGR surveys, select portions shown in Figures 4.3-4.6).

To the south, as Surface A1 deepens and surface B1 shallows until it daylights just south of line SUMUT-07 (Figure 4.5b), Sequence A thickens. In this area, numerous normal faults are visible dipping roughly to the north in the sediments of Sequence A which are most visible on dip line BGR06-144 (Figure 4.6a). These normal faults terminate below Surface B1 and the seafloor, consistent with an older phase of basin subsidence.

### ***Sequence B***

Sequence B is horizontally layered and consistently brighter than sequence A. The maximum thickness of Sequence B is ~1.3 s TWT and occurs in the central portion of the Aceh Basin, (imaged in SUMUT-03, Figure 4.4a) which we interpret to be the main depocenter of Sequence B. This sequence is characterized by high-amplitude coherent reflections interspersed with thin (<50ms) chaotic beds some of which pinch out to the northeast. These reflections have been interpreted as turbidites interspersed with beds formed by thicker mass transport deposits, possibly associated with earthquake events [Mosher *et al.*, 2008; Seeber *et al.*, 2007]. The variation in extent of the mass transport deposits which make up this sequence make identification of basin-wide marker horizons difficult. We have identified at least one through-going surface within this sequence, which provides a marker horizon within the northern part of the study area (B2 in Figures 4.3-4.5).

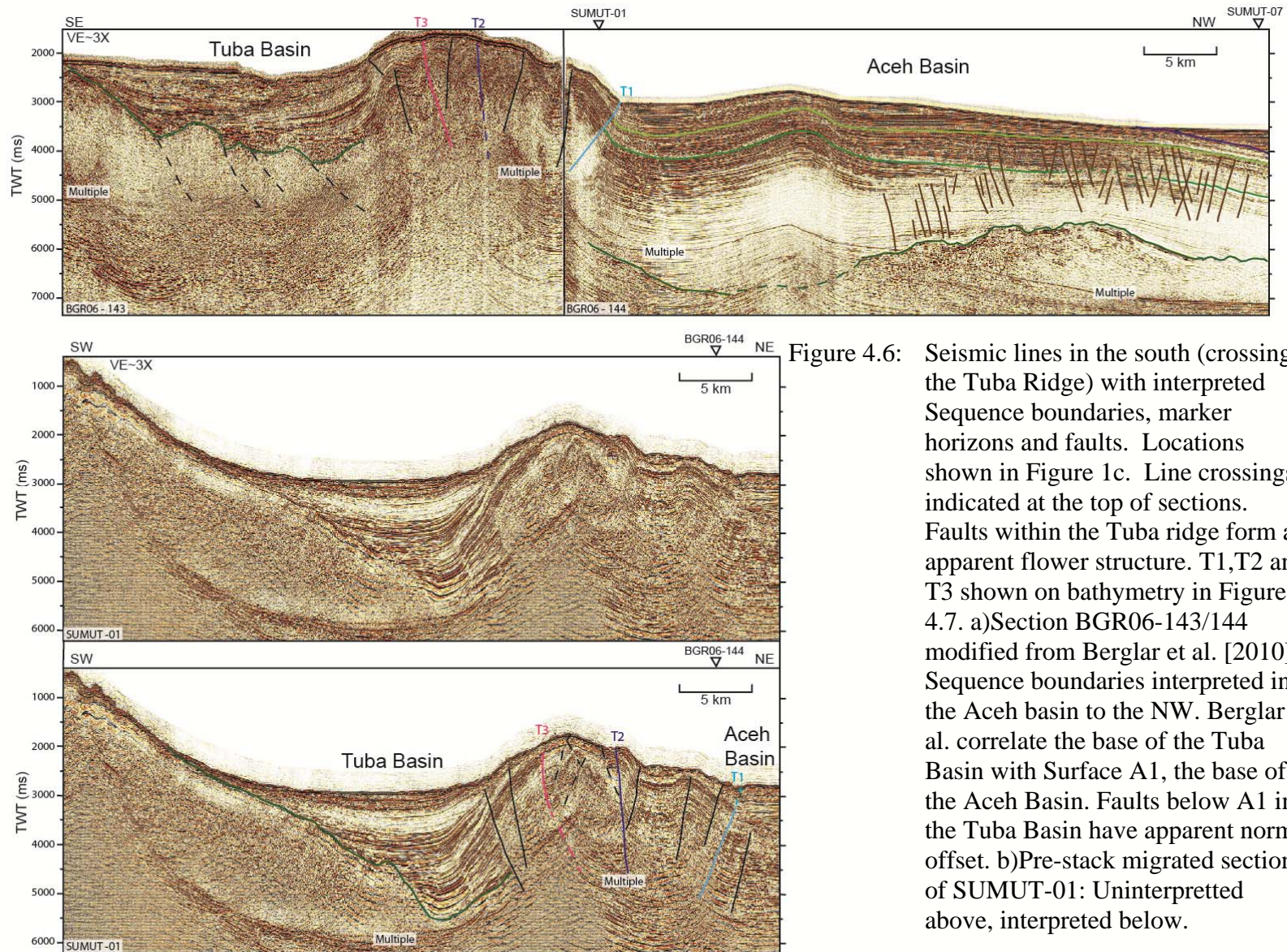


Figure 4.6: Seismic lines in the south (crossing the Tuba Ridge) with interpreted Sequence boundaries, marker horizons and faults. Locations shown in Figure 1c. Line crossings indicated at the top of sections. Faults within the Tuba ridge form an apparent flower structure. T1, T2 and T3 shown on bathymetry in Figure 4.7. a) Section BGR06-143/144 modified from Berglar et al. [2010]: Sequence boundaries interpreted in the Aceh basin to the NW. Berglar et al. correlate the base of the Tuba Basin with Surface A1, the base of the Aceh Basin. Faults below A1 in the Tuba Basin have apparent normal offset. b) Pre-stack migrated section of SUMUT-01: Uninterpreted above, interpreted below.

## **West Andaman fault**

We begin our analysis with the faults interpreted by Seeber et al. [2007]. Both Fault A1 and Group B can be traced along the seafloor in our bathymetry data (Figures 4.1c and 4.7a), diverging to the south-southeast and converging to the north-northwest, just south of SEATOS-24 (Figure 4.3c). Where the two merge, the deformation associated with the edge of the basin steps eastward. A small anticlinal ridge associated with this deformation is visible in the bathymetry, roughly parallel to the surface trace of Fault A1. We include the faults bounding this ridge in Group A, the designation for basin-edge fault traces. Group A faults dip trenchward (west) in our images (Figure 4.3-4.5), in contrast to the interpretation of single-channel seismic lines by Seeber et al., which had the basin-edge fault dipping toward the basin (east). Our interpretation implies that Group A faults are transpressional rather than transtensional, accommodating uplift within the zone encompassing the WAF rather than subsidence of the Aceh Basin.

The single-channel SEATOS lines (Figure 4.3a,b,c) image only the top 1 second or so, but the faults of Group B are still discernable dipping to the east. Additional faults between Groups A and B appear similar in geometry to group B faults and are included in Group C. The shallower apparent dip of the faults in SEATOS-25 (Figure 4.3b) is likely due to the oblique line-crossing of the fault.

On line SUMUT-03 (Figure 4.4a), we also find the two fault branches (A and B) and several steeper (dipping 70-80°) faults between them (Group C). Group A dips to the west and Group B dips to the east, while group C faults generally dip east, steepening as they approach the edge of the basin. The geometry of these additional faults is consistent with the idea of all the faults in this area converging at depth, forming one larger flower structure. In addition to these faults, we identify another set of faults dipping more

shallowly (8-35°W) in contrast to the Group A, B and C faults (60-80°), which we classify as Group D.

Line BGR06-107 (Figure 4.4b) is a multichannel seismic line through the region discussed by Seeber et al. Group B faults dip more shallowly (30-60°) here than in lines SUMUT-03 and SEATOS-24. Berglar et al. identified several additional fault traces on this line between the two main branches of the WAF. We classify these more vertical faults as Group C, but the interaction between Groups B and C is ambiguous in this image. Further examination of BGR06-107 reveals the presence of several Group D faults in addition to the Group A, B and C faults identified by Berglar et al. These Group D faults do not offset the seafloor and appear to be cut by faults in Groups A, B and C.

A third fault trace is visible in the bathymetry to the west of those related to Groups A and B, striking nearly north-south (Figure 4.1c and 4.7a). This trace is also characterized by a narrow linear basin, similar to that associated with Group B. SUMUT-03 (west of Figure 4.4a), BGR06-107 (Figure 4.4b) and SEATOS-26 (Figure 4.3a) all cross this third fault trace. The faults associated with this surface trace in the seismic lines make up Group E. Similar to Group B, Group E faults steepen to the north as they approach the other main fault traces along the edge of the Basin.

Moving south-southeast along the edge of the basin, we have several lines south of the single channel survey in Seeber et al. [2007]. SUMUT-05 and -07 are shown in Figure 4.5. At SUMUT-05 (Figure 4.5a), the faults of Groups A and B bound an uplifted and disrupted area 10km wide. Basin reflectors within Sequence B converge to the west near A1, implying the presence of growth strata associated with vertical offset on fault A1. The faults within the deformed area are steeper (70-89°, usually to the east) than Groups A and B and disrupt the basin sediments and the seafloor. Based on their dip and situation between Groups A and B, we classify these faults as Group C.

Across the deformed area, both Surfaces A and B can be traced roughly parallel to the seafloor, up to the west. Between these surfaces we find, shallow-dipping (10-30°), landward vergent, negative polarity reflectors. These reflectors appear to be disrupted by Group A, B and C faults and are classified as Group D.

Just south of SUMUT-05 (Figure 4.5a) the deformation front extends progressively basinward from the trend (26° west of north) of the basin edge north of SUMUT-05. SUMUT-07 (Figure 4.5b) crosses this wider area of deformation. Group B faults visible in the original processed data dip to the east and resemble Group B in SUMUT-05, but are to the west of our pre-stack section shown in Figure 4.5a. Faults resembling Group A are found along the Basin edge, dip ~60°W and obviously control this boundary, but are not contiguous with fault A1 to the north.

Near these basin edge faults in SUMUT-07 (Figure 4.5b), several faults dip more shallowly to the west and are included in Group D. The deepest of these (dipping 21°W) appears to be a thrust offsetting Surface A1. Up-warping of the deepest Sequence A sediments near the tip of this fault and shortening above A1 in the hanging wall indicates this fault was active in the earliest stages of basin infill. Just to the east, another fault (dipping 30°W) offsets sediments above A1, but not above the marker horizon A2. Most of Sequence A appears to have been folded and then cut by an unconformity we correlate with the horizon A3. This unconformity and the sediments above it are also folded, though to a lesser extent than the rest of Sequence A, indicating a second phase of shortening. Rough correspondence of the highs and lows of A3 with the highs and lows in the overlying seafloor indicate this shortening is likely related to the ongoing faulting in this area.

To the west of the Sequence A folds, sedimentary units are not distinguishable. In this area, we identify a number of faults offsetting the seafloor with apparent dips

between 25 and 60° to the east, most nearer to 50°. These faults are classified as Group C because they offset the seafloor, dip consistently with Group C faults to the north and converge with depth.

### **Tuba Ridge**

The Tuba Ridge is a zone of compressional uplift separating the Aceh Basin from the smaller Tuba basin [Berglar *et al.*, 2010]. SUMUT-01 intersects BGR06-143/144 just to the northeast of the Tuba Ridge (Figure 4.6). The faults interpreted within the Tuba Ridge on these two lines make up Group T. These faults dip toward the center of the anticlinal ridge with the faults in the center having the steepest apparent dip. Because both seismic lines cross the Ridge at oblique angles, the true dip on these faults is somewhat steeper than the reported apparent dips. Offset sediments and seafloor indicate thrust motion on most of the Group T faults. We trace several Group T faults (T1, T2 and T3) between the two seismic lines in the bathymetry data. Due to their influence on seafloor geometry, we consider these three faults to be currently the most active and include the seafloor traces of these faults in our regional interpretation (Figure 4.6a).

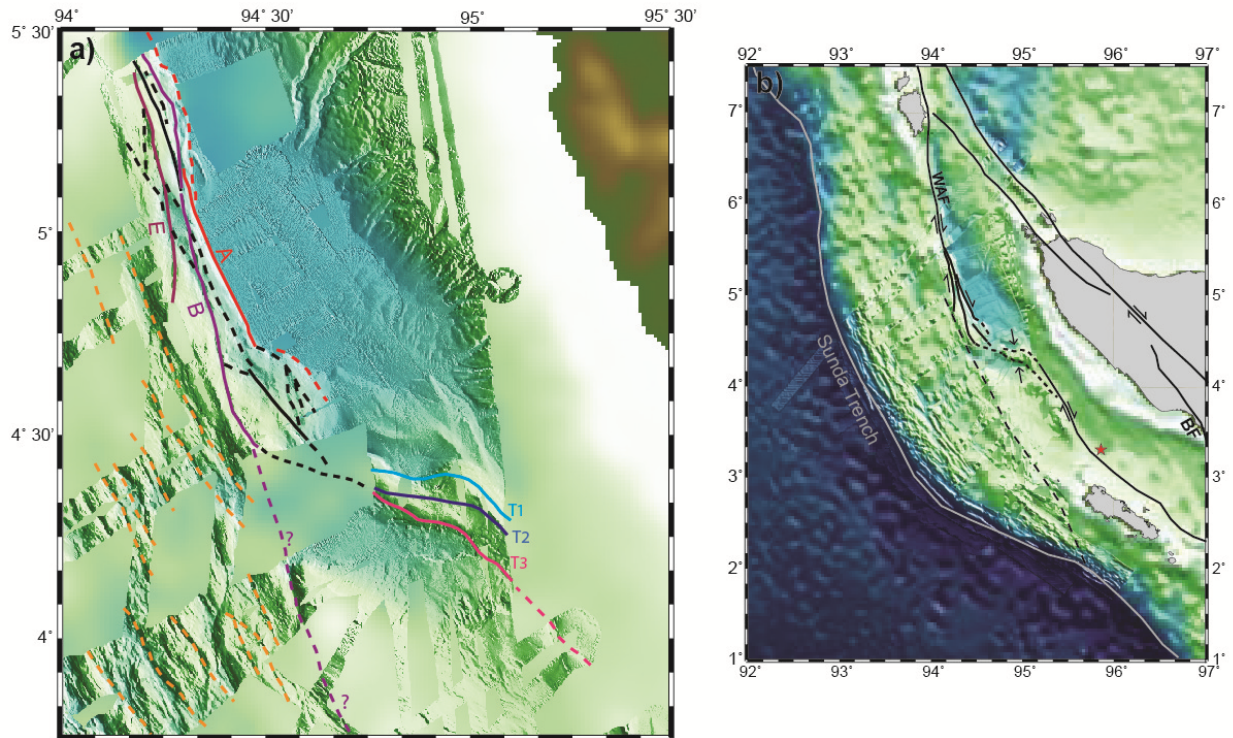


Figure 4.7: Maps of tectonic interpretation. a) Interpreted bathymetry in the Aceh Basin area. Seafloor traces of interpreted fault Groups A, B, E and T labeled. Black lines are Group C fault traces (Group D does not reach the seafloor). Orange dashed lines are traces of apparent plateau faults in the bathymetry data. Strike-slip West Andaman Fault may bifurcate near the intersection with the Tuba Ridge [Seeber *et al.*, 2007]. The possible SSE-striking branch is indicated by dashed purple line. The other branch curves to the east, forming the pop-up structure of the Tuba Ridge. b) Interpretation from (a) shown in a regional context. Sense of motion indicated by arrows. Red star is epicenter of the 2004 Sumatra-Andaman earthquake.

## DISCUSSION

### West Andaman Fault

The seafloor traces of Groups A, B and E, as well as select Group C faults are shown in Figure 4.7a. Along the edge of the central Aceh Basin, Group C faults consistently dip more steeply than Group B faults, forming an apparent flower structure that is bounded by Groups A and B. Offsets of the seafloor and major sequence boundaries imply a positive sense of motion on these flower structure faults with the exception of Group B faults, which bound a narrow basin. Anticlinal folding along the edge of the basin and growth strata in the youngest basin sediments near Group A faults are also consistent with compression across the WAF zone since the onset of Sequence B deposition. The presence of apparent flower structures in cross-section implies significant translational motion along strike on the WAF.

The strike of the Group C faults traceable in bathymetry is more similar to Group A than Group B. Group A strikes roughly parallel to main strand of the Sumatran Fault ( $\sim 26^\circ$  west of north), while Groups B and E strike closer to north-south ( $\sim 13^\circ$  and  $\sim 5^\circ$  west of north respectively). This strike is consistent with the western branch of the WAF thought by Seeber et al. to contribute to along-strike lengthening of the forearc as it cuts obliquely across the plateau. The continuation of this fault across the plateau was interpreted by Seeber et al. [2007] from a shutter ridge and apparent pullapart in bathymetry data south of  $4^\circ 30'$  N. Our bathymetry data in this area is patchy, and our lack of seismic lines crossing this branch along the western edge of the Tuba Basin prevents us from confirming strike-slip offset on fault traces in this area.

Berglar et al. [2010] also interpreted a strike-slip fault cutting the outer arc high after splitting off of the main WAF at the northern end of the Tuba Ridge. If a right-

lateral strike-slip fault branch does extend to the south from this position, it either strikes south-southeast, as the dashed line in Figure 4.7 (denoted by '?') or parallel to the plateau faults, whose traces are dashed in orange in Figure 4.7. We find no seafloor features in our bathymetry consistent with a through-going fault striking south-southwest.

Anticlines visible in our bathymetry and described in detail by Berglar et al. [2010] are associated with the WAF and the edge of the basin in the north. More anticlines curve around from the strike of the WAF to parallel to the Tuba Ridge in the southern portion of the basin. North-south compression across the Tuba Ridge, which appears to be an anticlinal ridge and a pop-up flower structure, is consistent with the compression expected of a left-hand step in a right lateral flower structure. The pull-apart associated with Group B faults and the anticlines and thrust offset associated with Groups A, C, and T implies that the pure shear direction is between the two strikes of Groups A and B ( $26^\circ$  and  $13^\circ$  west of north).

### **Thrust Faults**

In both the BGR and SUMUT surveys, we find several fault plane reflectors (Group D in Figures 4.4-4.6) with shallower dips of  $8-30^\circ$  away from the basin. Group D faults do not offset the seafloor and are cut by the faults in Groups B and C. In the southern Aceh Basin, Group D faults are associated with compressional deformation of the oldest basin sediments, indicating thrust motion on these faults. If the shallower dip of Group D throughout the study area is construed as additional evidence for thrust motion on these faults, then these faults are likely associated with the uplift of the forearc plateau.

The occurrence of these thrust faults could be associated with either the backthrust proposed by Chauhan et al. [2009] or the duplexing proposed as a mechanism

for plateau formation by Fisher et al. [2007]. Shallower dips (8-12°) on group D faults at their deeper end (to the west, ~2s below the seafloor) seem to argue against penetration of these faults to the plate boundary at depth, but our lack of imaging below the multiple prevents us from directly ruling out a steepening of these faults into a large-scale backthrust. However, we argue against a plate-boundary-scale backthrust based on the geometry of the basal unconformity (A1) as it crosses the WAF zone and extends trenchward for >15 km. Within the WAF zone, this reflector is disrupted, with some segments raised and some lowered, consistent with strike-slip motion distributed on the flower structure. Beneath the marginal plateau west of the WAF, the reflector is coherent and either flat or basinward dipping, similar to its geometry beneath the Aceh Basin. A regional backthrust with significant motion would offset this reflector such that the section beneath the plateau should be uplifted and tilted trenchward relative to the section beneath the Basin. We observe no such offset seaward of the deformed zone directly beneath the West Andaman Fault Zone and the observed tilting is entirely basinward, strengthening our conclusion that no large-scale backthrust penetrates to the plate boundary along this section of the Aceh Basin.

Whatever the large-scale process we associate with the Group D thrust faults, it is no longer actively driving uplift along them. Later basin sediments are not affected by these faults and the thrust faults themselves are cut by the flower structure of the WAF. Therefore, a backthrust with deep penetration or any other landward-vergent thrusting potentially associated with plateau formation is not currently active along the edge of the central and southern Aceh Basin and significant coseismic thrust motion offsetting the seafloor during the 2004 event is unlikely in this area.

## Quantifying Slip

In central Sumatra (near the equator), GPS and earthquake slip vectors suggest that about two-thirds of the margin parallel component of plate motion is accommodated on the Sumatran Fault system and the remaining one-third occurs offshore, likely on the megathrust [McCaffrey *et al.*, 2000]. Estimated slip rates on the Sumatran Fault vary a great deal, but are generally thought to increase from south to north [McCaffrey, 2009; Sieh and Natawidjaja, 2000]. Based on a uniform stretching rate in the forearc, McCaffrey [1991] predicted variation in the slip on the Sumatran fault from  $\sim 6 \text{ mm yr}^{-1}$  near the Sunda Strait to  $\sim 25 \text{ mm yr}^{-1}$  near the equator and  $\sim 50 \text{ mm yr}^{-1}$  in the Andaman Sea. Curray [2005] estimates the total opening rate in the Andaman Sea at  $\sim 38 \text{ mm yr}^{-1}$  based on magnetic anomalies. Thus slip on the northernmost end of the Sumatran Fault is likely greater than  $25 \text{ mm yr}^{-1}$ , but less than the  $\sim 50 \text{ mm yr}^{-1}$  estimated by McCaffrey [McCaffrey, 1991].

The uncertainty in the amount of slip on the Sumatran Fault in Northern Sumatra and the associated faults offshore to the north makes estimating of the amount of margin-parallel strain accommodated in the forearc difficult. Adding to the complexity of this determination is the deformation within the downgoing plate. Left lateral earthquake mechanisms associated with roughly north-south striking faults have been observed within the downgoing plate, generally between 5 and 10 degrees N [Rajendran *et al.*, 2011], but additional north-south oriented fractures indicate that this style of deformation may extend south beyond the equator [Delescluse and Chamotrooke, 2007]. The left-lateral sense of motion on these faults is consistent with the convergence between the Australian and Indian plates [Delescluse and Chamotrooke, 2007; DeMets *et al.*, 2010]. Within this section of the margin, it is impossible to precisely know the downgoing plate

vector at the trench, except that it is somewhere between the vectors associated with the Indian and Australian plates.

Without a good estimate of the amount of margin parallel strain required by the plate convergence vector but not accommodated by the Sumatran Fault, we do not know the maximum strain rate on the West Andaman Fault. In our study area we have not conclusively correlated any offset structures across the entire fault zone. Such an analysis is hampered by a lack of knowledge about the history of the forearc plateau and the complexity of the flower structure faults themselves. Even with offset structures, the lack of timing constraints in and around the Aceh Basin would keep us from assigning a rate to the motion.

### **Implications**

Even without knowing the strain rate along the WAF, we can still assert that the sense of motion on this fault is right-lateral transpression. This motion and the strike of the main fault strand (Group A faults) are consistent with the WAF accommodating a small portion of the partitioned trench-parallel strain on this margin. Localization of partitioned shear strain along the seaward edge of a forearc basin has been observed previously, for example, the Kumano Basin Edge Fault Zone (KBEFZ) in the Nankai Trough, Japan [Martin *et al.*, 2010] and the Hawley Ridge Shear Zone (HRSZ) in the Aleutian forearc [Ryan and Scholl, 1989]. In the case of the KBEFZ, the observed transtensional faults occur between the megasplay thrust system and the Kumano forearc Basin, about 30 km from the trench. This position is at the transition between the actively deforming outer wedge and the more stable inner wedge [Kimura *et al.*, 2007].

In the Aleutian forearc, the HRSZ truncates the seaward flank of the Atka forearc Basin and shears the southern portion of the Hawley Ridge, which is an antiformal

structure associated with the outer arc high [Ryan and Scholl, 1989]. The HRSZ varies along strike between transpressional uplifts and transtensional depressions, depending on the strike of the individual fault traces within the shear zone [Dobson *et al.*, 1996]. Although the HRSZ sometimes bounds the seaward edge of the forearc basin and sometimes the seaward edge of the outer arc high, it lies consistently just landward of the active accretionary prism, ~30 km from the trench. This position is coincident with the seaward extent of the arc basement rocks, which are seen to underlie both the Atka Basin and the Hawley Ridge in multichannel seismic lines [Ryan and Scholl, 1989]. The HRSZ, like the KBEFZ, therefore lies at the landward edge of the actively deforming outer wedge.

Offshore northern Sumatra, the WAF occurs at the boundary between the marginal plateau and the Aceh forearc Basin, which is also a significant boundary in the forearc. In the cases of the KBEFZ, the HRSZ and the WAF, rheological boundaries within the forearc appear to control where shear strain is localized, indicating that future work in forearcs should focus on such boundaries for possible identification of additional strike-slip motion within the forearc.

## CONCLUSIONS

We combine pre-stack images of the West Andaman Fault Zone (WAF) from the deep-penetration, multichannel SUMUT seismic lines with previous seismic and bathymetric surveys of the central and southern Aceh Basin region in order to ascertain the sense of motion along this Fault Zone. An apparent pop-up flower structure is seen in cross-sections of the main WAF along the western side of the Aceh Basin and within the Tuba Ridge, indicating a significant component of translational motion as well as compression. The interpretation of the Tuba Ridge as a pop-up structure is consistent

with its position at a leftward step in a right-lateral strike-slip system. We conclude that the WAF along the edge of the central and southern Aceh basin is transpressional.

We identify previously uninterpreted thrust faults within the area of the WAF. These thrust faults do not penetrate to the seafloor and are offset by the faults of the active flower structure, indicating that the thrusts themselves are not currently active. We find no evidence of a modern backthrust in our data, which argues against significant coseismic uplift on such a feature during the 2004 Sumatra-Andaman earthquake. Instead, the edge of the modern Aceh Basin is controlled by transpression on the predominantly strike-slip WAF. Quantifying slip on the WAF is difficult due to uncertainties in the regional motion vector amplitudes and the lack of timing constraints in the Aceh Basin.

## Chapter 5: Conclusions

In Chapter 2, we model the process of formation invasion and utilize NanTroSEIZE logging-while-drilling resistivity data to ascertain the relative magnitudes of permeability in sandy beds. Traditional permeability measurements are performed on cores [e.g. *Dugan and Daigle, 2010; Saffer et al., 2010a; Sreaton et al., 1990*], which yield an inherently sparse and biased dataset. Core recovery in sands and faulted zones is generally poor, preventing direct measurement of permeability in the zones where permeability is thought to be the greatest. We still use a few cores to constrain model parameters such as pore water salinity, but our method allows us to estimate permeability in sands anywhere that we have logging-while-drilling data, even in zones with no core recovery.

Our results show that sands within faulted zones are 1-3 orders of magnitude more permeable than sands not in faulted zones. This conclusion is consistent with the idea of faults acting as fluid conduits in an accretionary prism [e.g. *Saffer and Bekins, 1998*]. Knowing how faults affect permeability and fluid flow is important for improving our understanding of the mechanics of accretionary wedges as a whole and plate boundary thrusts in particular [e.g. *Dahlen et al., 1984; Davis et al., 1983; Neuzil, 1995; Saffer, 2010*].

In chapters 3 and 4, we demonstrate the presence of strike-slip faults in the forearcs of Japan and Sumatra. Both the Kumano Basin Edge Fault Zone (KBEFZ) in the Nankai Trough Subduction Zone and the West Andaman Fault Zone (WAF) in the Sumatran Subduction Zone are characterized by inward-dipping, steep faults in cross-section that we interpret as flower structures and linear seafloor expressions typical of strike-slip faults. Based on the observed pattern of faulting, both in cross-section and

along the seafloor, we conclude that the KBEFZ is transtensional and the WAF is transpressional. In both cases, the direction of translational motion is consistent with the direction of overall convergence obliquity and therefore also consistent with the direction of partitioned shear strain.

Fitch [1972] hypothesized that major strain partitioning faults in oblique subduction zones, such as the Sumatran Fault, were located near the volcanic arc because the arc represented a zone of weakness in the overriding plate. However, the occurrence of trench-parallel faults with volcanic arcs are found in only a few locations [McCaffrey, 2009]. Some finite element models [e.g. McCaffrey *et al.*, 2000] suggest that the location of strike-slip faults in these settings is instead controlled by downdip shear stress. However, our results show partitioned shear strain localizing both near the arc and within the forearc in these two subduction zones (Figure 5.1).

The KBEFZ lies between the Kumano forearc Basin and the surface traces of the megasplay fault system, placing it between a relatively stable inner wedge and an actively deforming outer wedge (Figure 5.1b) [Kimura *et al.*, 2007; Wang and Hu, 2006]. The WAF lies between the Aceh forearc Basin and the marginal plateau, which appears to have slipped seismogenically during the 2004 Sumatra-Andaman great earthquake [Ammon *et al.*, 2005; Gulick *et al.*, 2011; Ishii *et al.*, 2005]. Therefore, both the KBEFZ and the WAF lie at significant rheological boundaries in the forearc. This coincidence may indicate that such rheological boundaries are conducive to the localization of lateral shear strain. Further study should include other margins as well as additional finite element modeling to investigate the hypothesis that partitioned shear strain preferentially localizes along rheological boundaries.

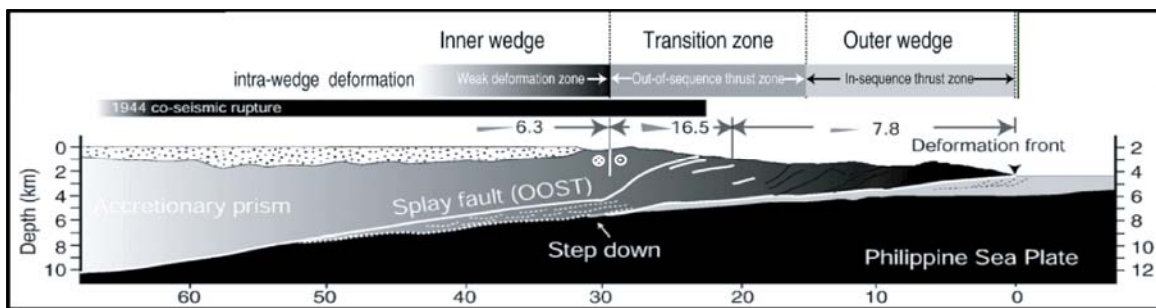
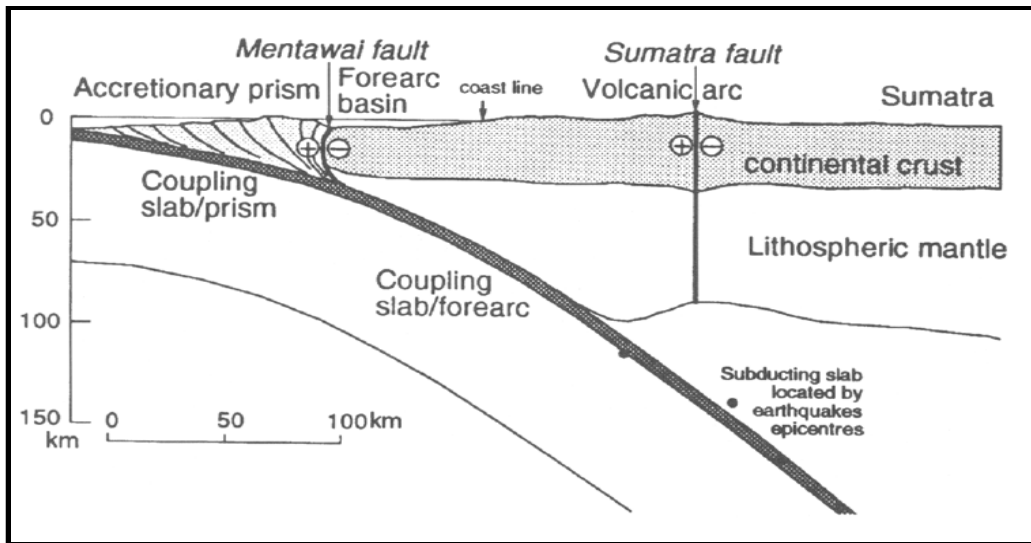


Figure 5.1: Cross sections of subduction zones showing partitioned strain in the forearc.  
 a) Sumatran Subduction Zone [Malod and Kemal, 1996]: Shows the position of the Mentawai Fault near central Sumatra, which is equivalent to the position of the WAF in the north. b) Nankai Trough Subduction Zone: Shows location of the strike-slip KBEFZ between the Inner and Outer Wedge [Modified from Kimura *et al.*, 2007].

Another implication of strike-slip faulting in the forearc is the influence such a feature has on seismic hazards. We do not know how deep the WAF fault penetrates into the crust or the strain rate on this fault. If both depth and strain rate are large enough, the WAF would be potentially seismogenic. If the WAF accommodates a significant amount of trench-parallel motion, it could reduce the amount of motion on the Sumatran Fault,

decreasing the size of strike-slip earthquakes directly beneath the island. Or, if the WAF is accommodating shear strain that cannot be accommodated by the Sumatran Fault, the motion on the WAF allows fuller partitioning of the oblique convergence vector, making the motion on the plate boundary fault closer to pure thrust.

The studies presented in this dissertation utilize data on a broad range of scales, from resistivity logs that can sense centimeters of fluid invasion beyond a borehole wall to 2d and 3d seismic data that cover 10s of kilometers. In order to understand the mechanics of accretionary wedges and evaluate the hazards associated with plate boundary thrusts in accretionary subduction zones, incorporation of data from this wide range of scales is imperative. International, collaborative, long-term projects like NanTroSEIZE facilitate investigations of these margins from the pore-scale to the plate-tectonic scale and even temporally through geophysical observations [*Kinoshita et al.*, 2009; *Saffer et al.*].

## Appendices

### APPENDIX A: ADVECTION VS. DIFFUSION IN NON-DIMENSIONAL ANALYSIS

The following was developed using Bird et al. [2007] and Weisstein [2007].

Two dimensionless groups exist which could describe the relative importance of advection and diffusion in a mass transport problem: the Sherwood Number ( $Sh$ ) and the Péclet Number ( $Pe$ ). The Sherwood Number is the mass transfer equivalent of the Nusselt Number used in heat flow analysis, which shows the ratio of convective mass transport to diffusive mass transport between the wall and the bulk fluid. The value is the product of the mass transfer coefficient ( $K$ ) and the characteristic length ( $L$ , e.g. the pipe diameter) divided by the diffusion coefficient ( $D$ ) of the migrating species:

$$Sh = \frac{KL}{D}$$

To calculate the Sherwood Number in our fluid invasion system, we would need to calculate the mass transfer coefficient ( $K$ ) and the calculated value would only be useable near the boundary of the system (the borehole wall).

We prefer to use the Péclet Number, which is the ratio of the rate of advection of driven by flow, to the rate of diffusion driven by an appropriate gradient. In species or mass diffusion the Péclet Number is the product of the characteristic length ( $L$ ) and the advection velocity ( $v$ ) divided by the diffusion coefficient ( $D$ ):

$$Pe = \frac{Lv}{D}$$

This value can be used across the entire system, not just at a boundary, and we need not calculate any parameters beyond those already used in the models presented in this paper.

To estimate the range of possible Péclet Number values in our system, we use the invasion distance versus time curves calculated with the MatLab code in Appendix A (using equations {4} and {6} and Table 2.1). We approximate the velocity at any time  $t$  as the average velocity from the start of invasion until time  $t$  ( $v = d_i/t$ ) and assume a characteristic length equal to the depth of invasion ( $d_i$ ).

$$Pe = \frac{d_i^2}{tD}$$

For the diffusion coefficient, we choose the diffusivity of the  $\text{Cl}^-$  ion ( $2.03 \times 10^{-5} \text{ cm}^2/\text{s}$ ), which is greater than that of  $\text{Na}^+$  and similar to  $\text{K}^+$  and  $\text{I}^-$ .

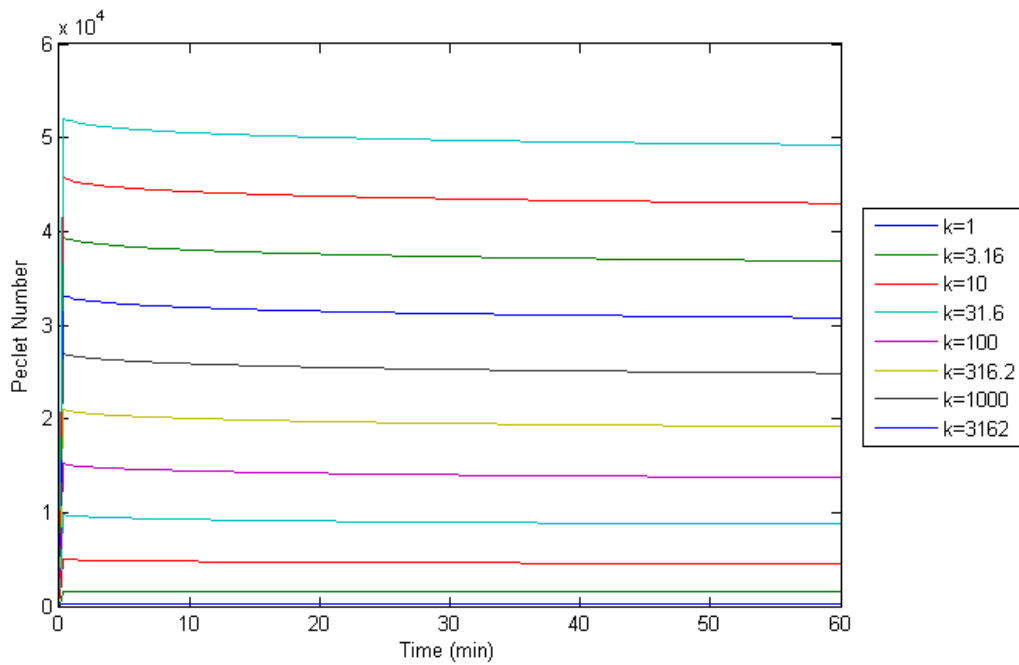


Figure A.1: Peclet Number vs Time for a range of formation permeabilities

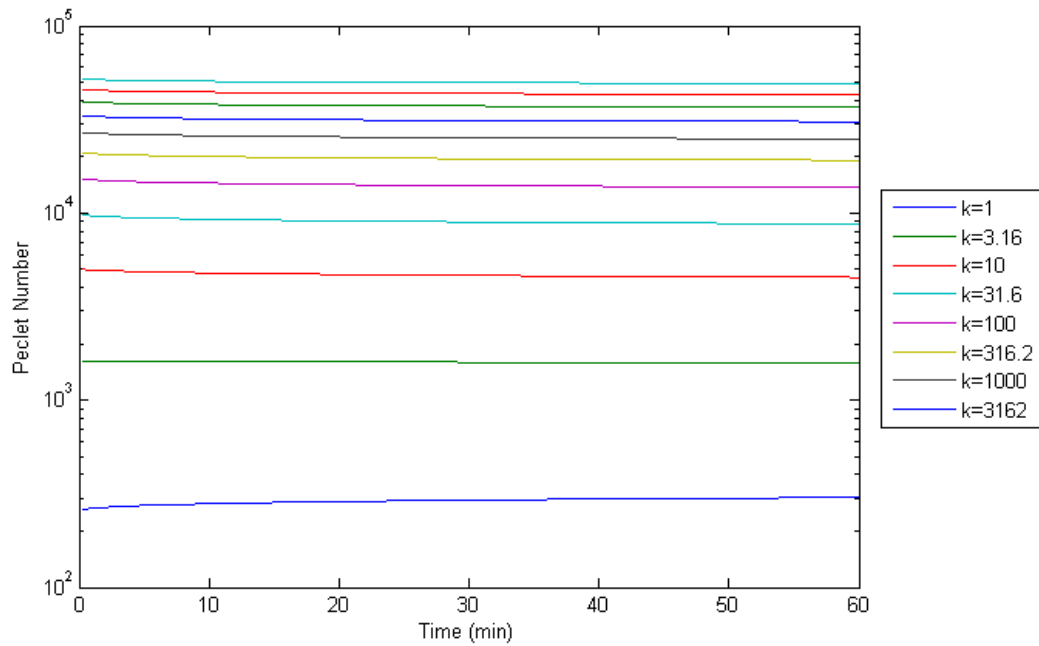


Figure A.2: Same as Figure A.1 on a semilog plot

Our Péclet Number is dependent on permeability because the advection velocity is dependent on permeability as expressed by Darcy's law (Equation {2.5}). The value ranges from 260 to 49000. A large Péclet Number indicates the dominance of advection over diffusion in this system. The square root of this value (which ranges from 16 - 221) is roughly the ratio of the distance traveled due to advection over the distance traveled due to diffusion. These results indicate that advective transport is greater than diffusion by over an order of magnitude at minimum and sometimes by more than four orders of magnitude. This result supports the omission of diffusive transport from our model .

## APPENDIX B: FLUID INVASION MODEL CODE

### Carslaw\_k.m

```
clear
global mu rho g Cv k P1 P0 a phi
%constants
a=0.2; % radius of the borehole
mu=1.08e-3; % viscosity at 20C (Paxs)
phi=.4; % porosity (fraction)
rho=1024; % water density
g=9.8;
B=4*10^-10; % compressibility of water (m2/N)
% Cv=k/(mv*rho); % coeff. of consolidation (m2/s)
Cv=10^-6;
% Pressure difference = 10% (Lithostatic -hydrostatic)
D=500; % depth (m)
P1=(2100+D)*g*rho; % hydrostatic
P0=P1+500000;
x=zeros(200,4);

for c=1:1:9 % varying permeability
    k=10^(0.5+c*0.5)*10^-16;
    opt = odeset('RelTol',1e-10,'AbsTol',1e-10);
    [t,r] = ode23s(@ODERhs,linspace(.00001,60*60,200),[.2],opt);
    x(:,c)=r;
end

V=pi*x.^2-pi*a*a;

% data points for plot (from chapter 2, table 2)
dataT1f=[2392;1146];
dataT1s=[453;356;2643;732];
dataT4s=[430,415,1515];
dataT1f=dataT1f/60;
dataT4s=dataT4s/60;
dataT1s=dataT1s/60;
dataR1f=[.1535;.3861];
dataR1s=[0;.1301;.3861;.1348];
dataR4s=[.0615;.1512;.3736];
```

figure

```

plot(t/60,V)
hold on
plot(dataT1f, dataR1f,'r+')
plot(dataT1s,dataR1s,'b+')
xlabel('Time (min)')
ylabel('Invaded Area (m2)')
legend('k=1','k=3.16','k=10','k=31.6','k=100','k=316.2','k=1000','k=3162','k=10000');

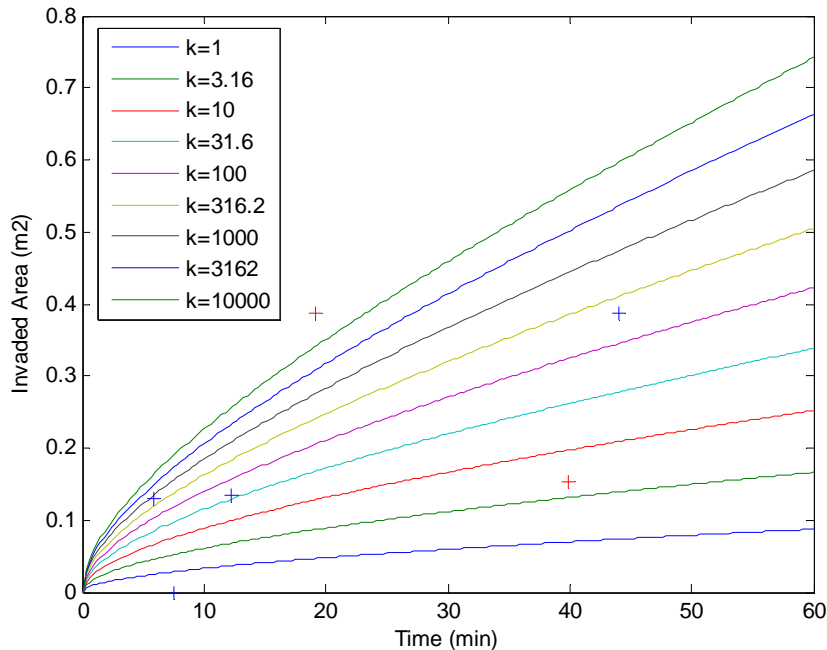
```

### ODErhs

```

function [ rhs ] = ODErhs2(t,r)
global k mu phi
h=.000000001;
rhs = -2*k*pi*0.2*(Psol(0.2+h,t)-Psol(0.2,t))/(mu*phi*h);
end
Psol2
function [ P ] = Psol2(r)
%P solution from Carslaw
global P0 P1 a Cv c
t=c;
P=((a./r).^(1/2).*erfc((r-a)/(2*sqrt(Cv*t)))...
-Cv*t*(9*a^2-2*a*r-7*r.^2)./(32*a^1.5*r.^2.5).*erfc((r-a)/(2*sqrt(Cv*t))))*(P0-P1);
end

```



## APPENDIX C: BOUNDARY FLUX METHOD FOR FLUID INVASION MODEL

In addition to the particle tracking solution we use in the main text, we also computed an invasion model using a boundary flux solution. Knowing the pressure gradient at the borehole wall, we can compute the flux through this boundary and convert that to a distance of invasion by using that flux volume to fill the cylindrical pore space. Below is the code for this solution, followed by the code we used to compare the boundary flux solution with the particle tracking solution.

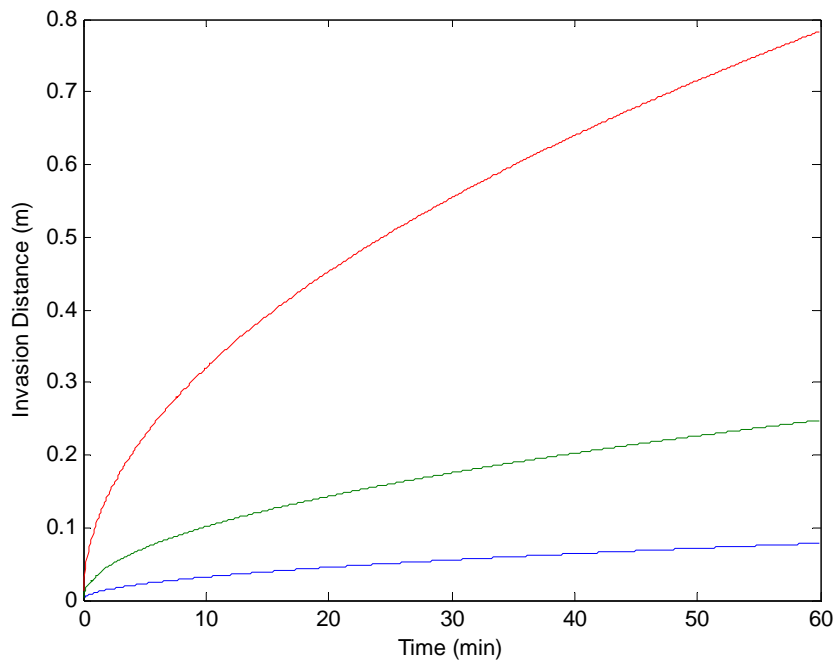
### Boundary\_flux.m

```
%flux at x=0 as a function of time in one dimension
clear
%constants
mu=1.08e-3; %viscosity at 20C (Paxs)
phi=.4; %porosity (fraction)
rho=1024; %water density
g=9.8;
%B=4*10^-10; %compressibility of water (m2/N)
%mv= %stiffness coeff.
%Cv=k/(mv*rho); %coeff. of consolidation (m2/s)
Cv=10^-6;
k=10^-15;

%Pressure difference = 10% (Lithostatic -hydrostatic)
D=500; %depth (m)
P1=(2100+D)*g*rho; %hydrostatic
P0=P1+500000;

for c=1:1:3 %varying permeability
    k=10^(0.5+c*0.5)*10^-16;
    t=[1:5:3600];
    Qi=2*k*(P0-P1)*sqrt(t)/(mu*phi*sqrt(Cv*pi));
    Q(:,c)=Qi;
end

figure
plot(t/60,Q);
xlabel('Time (min)')
ylabel('Invasion Distance (m)')
```



### stiffness\_test.m

%Calculate the difference btw boundary flux and particle tracking sol'n

% varying k (same as varying mv)

clear

global mu rho g Cv k P1 P0 a phi

%permeability range

k1=10^-18;

nk=7;

%% Constants

a=0.2; % radius of the borehole

mu=1.08e-3; % viscosity at 20C (Paxs)

%mu=2.822e-4; % viscosity at 100C (Paxs)

phi=.4; %porosity (fraction)

rho=1024; % water density

g=9.8;

%B=4\*10^-10; %compressibility of water (m2/N)

%mv= %stiffness coeff.

%Cv=k/(mv\*rho); %coeff. of consolidation (m2/s)

Cv=10^-6;

```

%Pressure difference = 10% (Lithostatic -hydrostatic)
D=500; %depth (m)
P1=(2100+D)*g*rho; %hydrostatic
%P0=P1+(D*g*(2300-rho)*0.1);
P0=P1+500000;

%% Carslaw solution
x=zeros(200,3);
for c=1:1:nk %varying permeability
    k=10^(0.5+c*0.5)*(k1/10);
    opt = odeset('RelTol',1e-10,'AbsTol',1e-10);
    [t,r] = ode23s(@ODERhs,linspace(.00001,60*60,200),[.2],opt);
    x(:,c)=r;
    c
end

Carslaw_V=pi*x.^2-pi*a*a;

figure
subplot(3,1,1)
plot(t/60,Carslaw_V)
title('Particle Tracking Solution')
xlabel('Time (min)')
ylabel('Vparticle (m3)')
legend('k=.001','k=.00316','k=.01','k=.0316','k=.1','k=.316','k=1.0')%,'k=3.16','k=10.0');

%% Boundary Flux solution
clear r x t c v

V=zeros(200,3);
r=a;
for c=1:1:nk %varying permeability
    k=10^(0.5+c*0.5)*(k1/10);
    opt = odeset('RelTol',1e-10,'AbsTol',1e-10);
    [t,v] = ode23s(@ODERhs2,linspace(.00001,60*60,200),0,opt);
    V_flux(:,c)=v;
    c
end

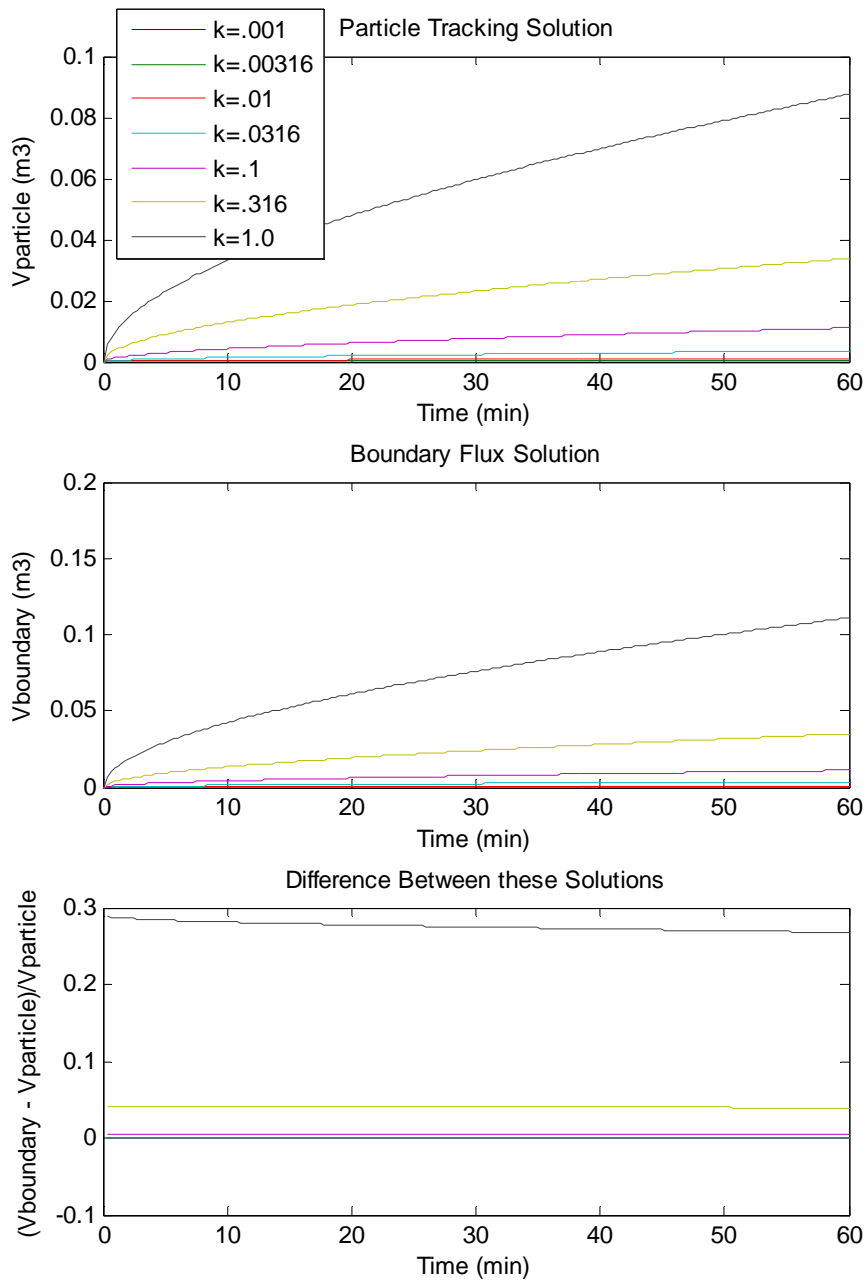
x=sqrt(a*a+V/pi);

subplot(3,1,2)

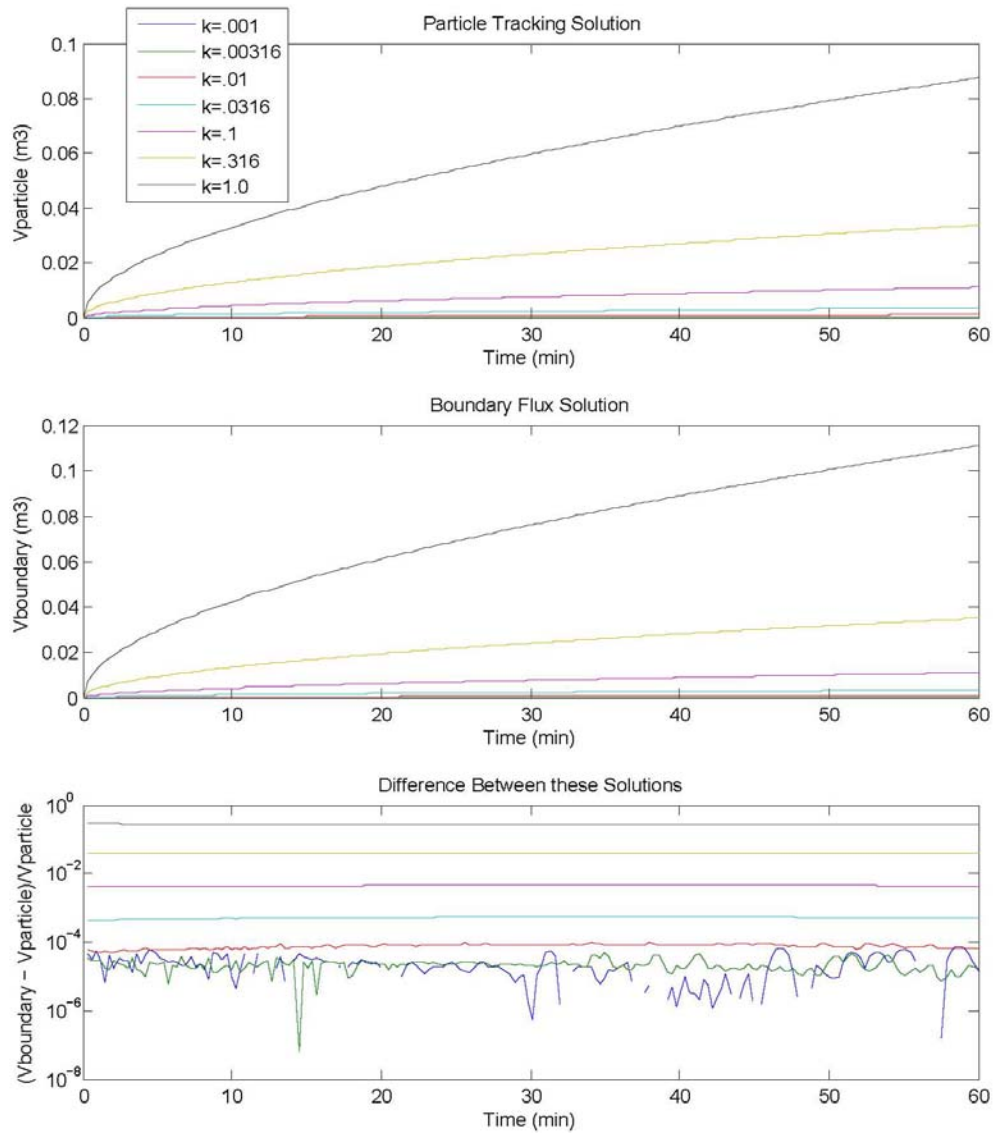
```

```
plot(t/60,V_flux)
title('Boundary Flux Solution')
xlabel('Time (min)')
ylabel('Vboundary (m3)')
%legend('k=1','k=3.16','k=10','k=31.6','k=100','k=316.2','k=1000','k=3162','k=10000');

%% Difference btw methods
Vdiff=(V_flux-Carlaw_V)./Carlaw_V;
subplot(3,1,3)
plot(t/60,Vdiff)
title('Difference Between these Solutions')
xlabel('Time (min)')
ylabel('(Vboundary - Vparticle)/Vparticle')
```



We can see that the two solutions do not yield the same results. The plot below is the same as the plot above, with the difference between the two solutions shown on a log scale.



The difference between the two solutions is caused by compression of the matrix due to an increase in pressure. The boundary flux solution does not account for this compression, while the particle tracking solution does. So assuming a constant  $C_v$ , the larger the value of  $k$ , the larger the value of volume compressibility ( $mv$ ), and the greater the difference between the particle tracking and boundary flux solutions.

#### APPENDIX D: PRESSURE ASSUMPTIONS FOR FLUID INVASION MODEL

The distance of invasion for a given permeability and time after bit depends on pressure, specifically the pressure differential between the borehole and the formation. Without leakoff tests, we think the best way to estimate this pressure difference is by comparing the annular pressure log (APRS on the APWD tool) to calculated hydrostatic pressure.

Problem: The hydrostatic pressure calculated is often higher than the APRS log. If this is true, the formation water should flow into the borehole and the hole itself should be quite unstable. In C0006A, the APRS log is below hydrostatic in most of the borehole (Figure D.1)

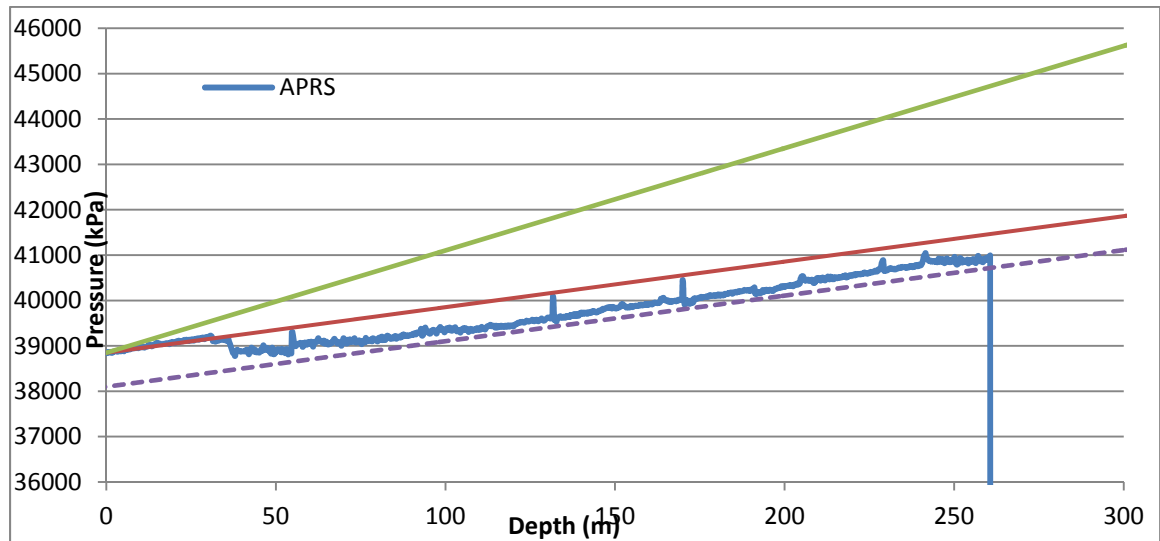


Figure D.1: Pressure plot from C0006B. The hydrostat (red) is calculated using a water density of 1.024 g/cc and the lithostat (green) using 2.3 g/cc. Both are assumed equal to the APRS log value at the seafloor (to eliminate any issues with how water depth was measured and temperature throughout the water column).

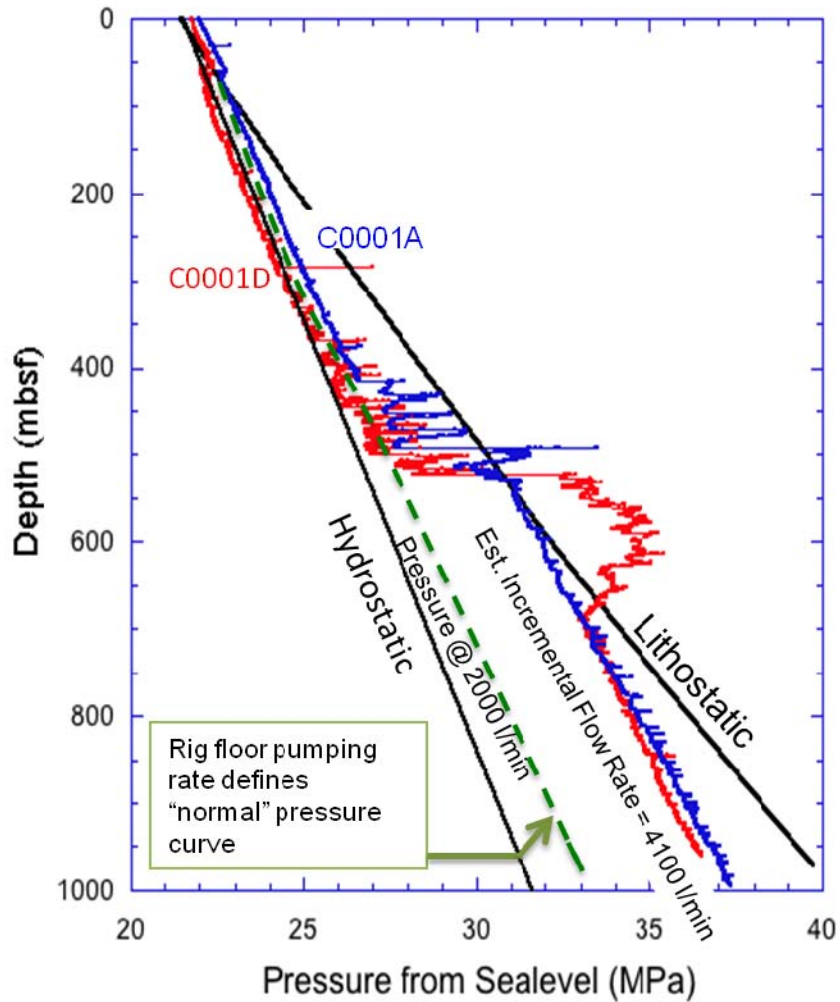


Figure D.2: Pressure plot for C0001. C0001A is the pilot hole and C0001D was logged by the LWD string. Rig floor pumping rate is from hole C001D. Figure courtesy of Casey Moore.

In hole C0001D the APRS log reads below hydrostatic near the top of the hole (Figure D.2). I did some calculations for C0001D as well:

Seafloor depth at C0001D is 2198m.

$$\rho \cdot g \cdot h = 1.024 \cdot 9.8 \cdot 2198 = 22057 \text{ kPa}$$

but the APRS (annular pressure from the PWD tool) at the seafloor is 21780 kPa.

The water density required to get the APRS pressure at the seafloor is:

$\rho_{\text{calc}} = 21780 / (2198 * 9.8) = 1.01112 \text{ g/cc}$ , which is very low.

If I calculate a hydrostat for each of these water densities, I get values higher than the APRS log down to ~500 ft (which is where we raised the circulating pressure because of drilling conditions).

For example, at 435m:

$$\rho * g * h = (2198 + 435) * 9.8 * 1.024 = 26423 \text{ kPa}$$

$$\rho_{\text{calc}} * g * h = (2198 + 435) * 9.8 * 1.011 = 26087 \text{ kPa}$$

Calculating from the seafloor (assuming the hydrostat equals the APRS reading at the seafloor):

$$P_{\text{sf}} + \rho * g * dH = 21780 + 1.024 * 9.8 * 435 = 26145 \text{ kPa}$$

$$P_{\text{sf}} + \rho_{\text{calc}} * g * dH = 21780 + 1.011 * 9.8 * 435 = 26090 \text{ kPa}$$

All of these results are greater than the APRS log value of 26007 kPa.

The result of the above pressure analysis is that we do not trust the APRS reading as an accurate pressure log within the borehole. The formation pressure is even more poorly constrained, though we assume it must be somewhere between the hydrostat and the lithostat. Based on this assumption and the need for the borehole pressure to be sufficiently higher than the formation pressure to maintain borehole stability, we know that the difference between the two ( $\Delta P$ ) is positive and, at our sample depths, probably greater than 50 kPa and less than 5000 kPa. We chose 500 kPa as approximately 10% of the difference between the lithostat and hydrostat at 500 m depth. Any errors caused by this assumption will be systematic in our results, changing modeled permeability in the opposite direction, but by the same order of magnitude as  $\Delta P$ . Because we are comparing permeabilities for relative magnitudes, this systematic error should have minimal effects on our results.

## **APPENDIX E: SUMUT SURVEY PROCESSING FLOW**

All SUMUT lines were processed as follows. Plots of this version of the data were presented in Gulick et al. [2011] and Martin et al. [2011].

Read in shots from SEG-D file

Define geometry

Export shot times from focus and calculate ship's position at each time from 1-second navigation data

Find average shot spacing by utilizing Open Office

Define station locations every 1.25m along a line

Call PATTERN to define receiver locations relative to shots

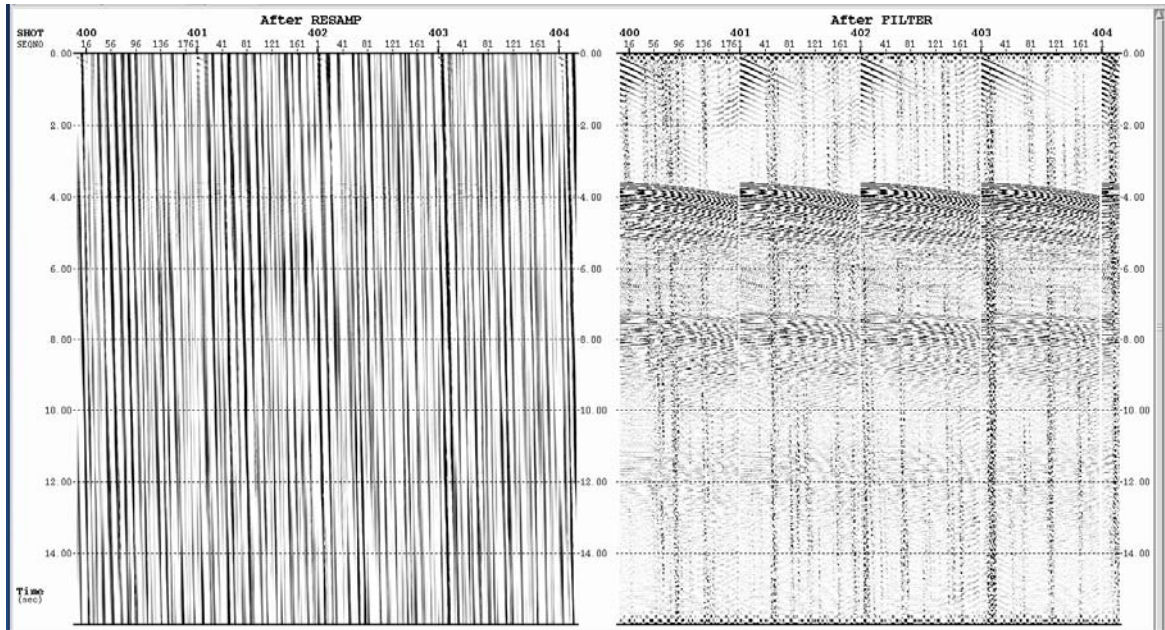
Call SOURCE

Define first shot location such that far offset receiver is at station 1

Set shot spacing to even number of stations

Desample: 4ms

Bandpass filter: 3-6-60-80 Hz minimum phase

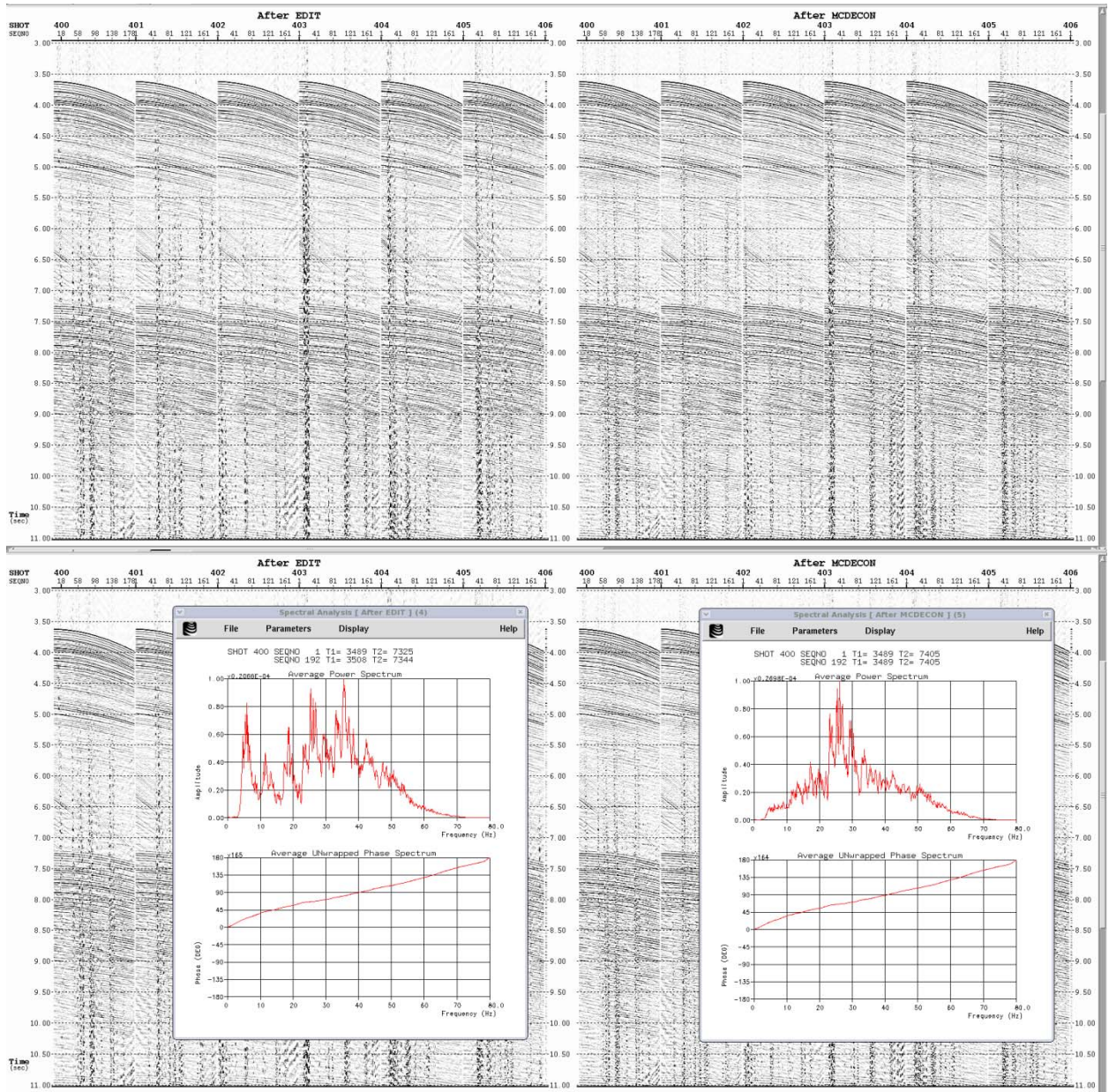


(Note that some swell noise remains after bandpass filter.)

Amplitude recovery: module GAIN, time<sup>2</sup>

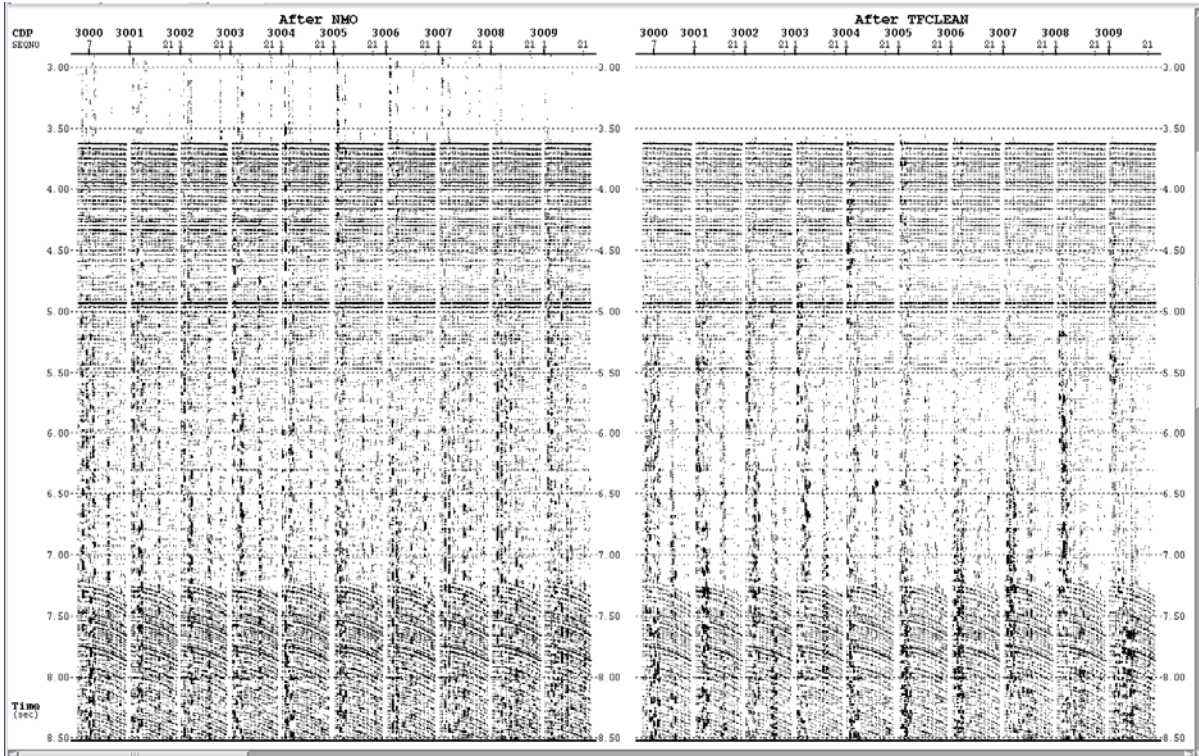
Kill trace 192 - Tail buoy noise is noted in most shots and the far channel (192) is particularly noisy.

Multichannel predictive (GAP) deconvolution: minimum phase with 11 trace window, 300 ms operator and 24 ms gap length, design window of 3s starting below seafloor. (See screenshot on next page)

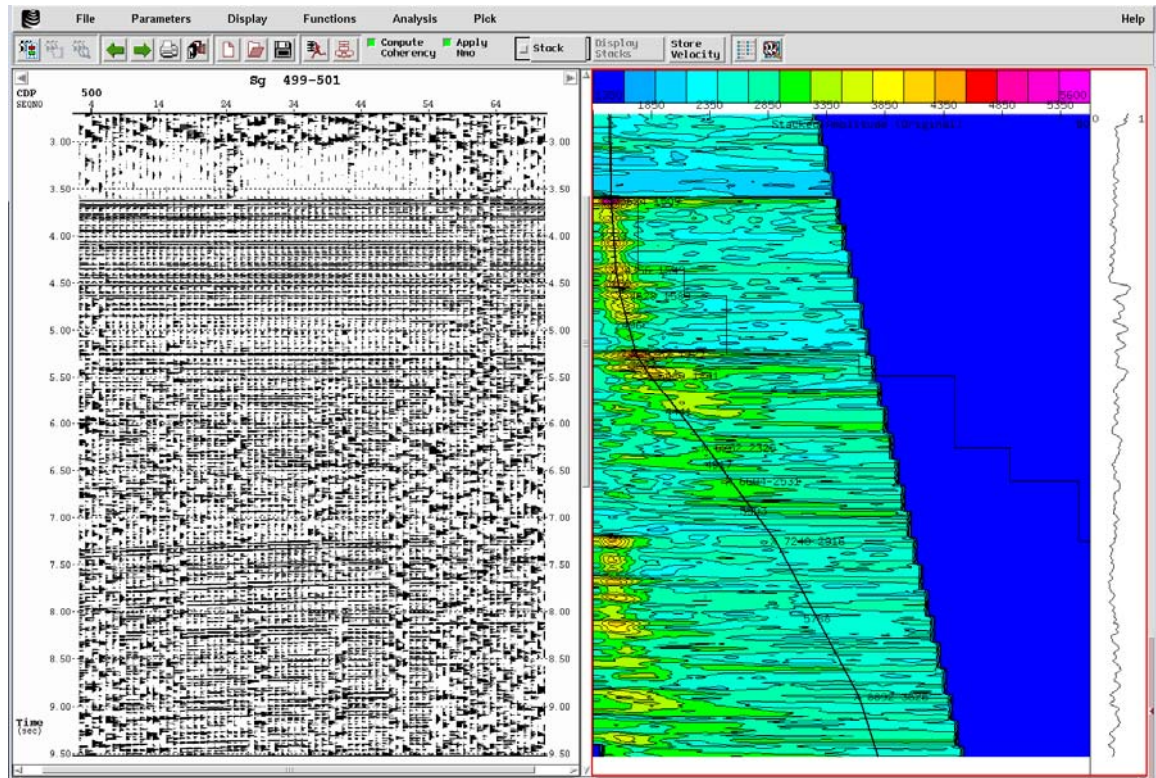


Sort: bin traces into CMPs (defined every 6.25m)

Time-frequency noise suppression (TFCLEAN): scales groups of 7 traces to the median amplitude within the 3-55 Hz frequency band. The goal is to minimize the swell noise while affecting the signal as little as possible. (See screenshot below)



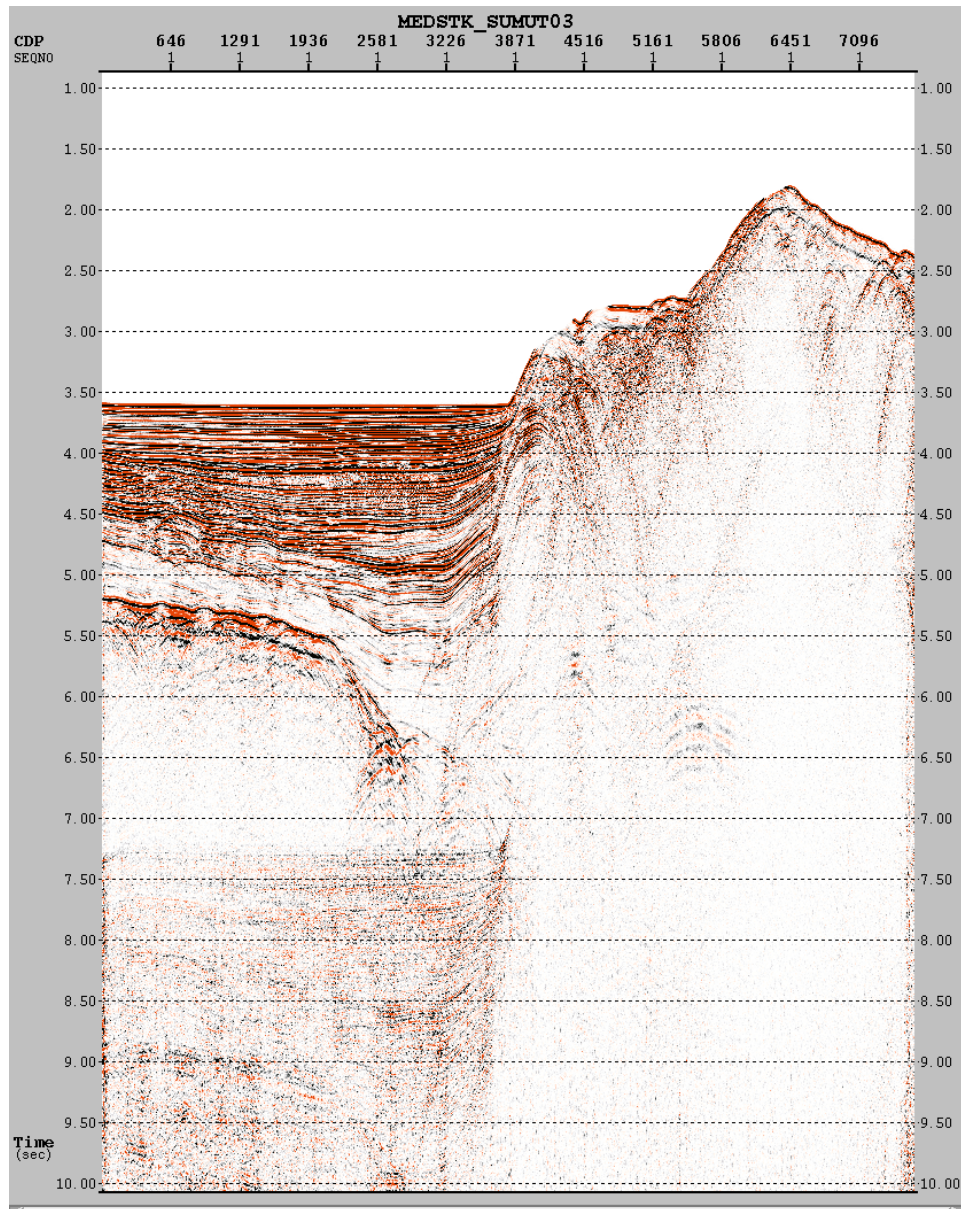
NMO correction: velocity analysis performed on supergathers every 500 CMPs  
(additional analysis every 250 CMPs on lines crossing the West Andaman Fault)



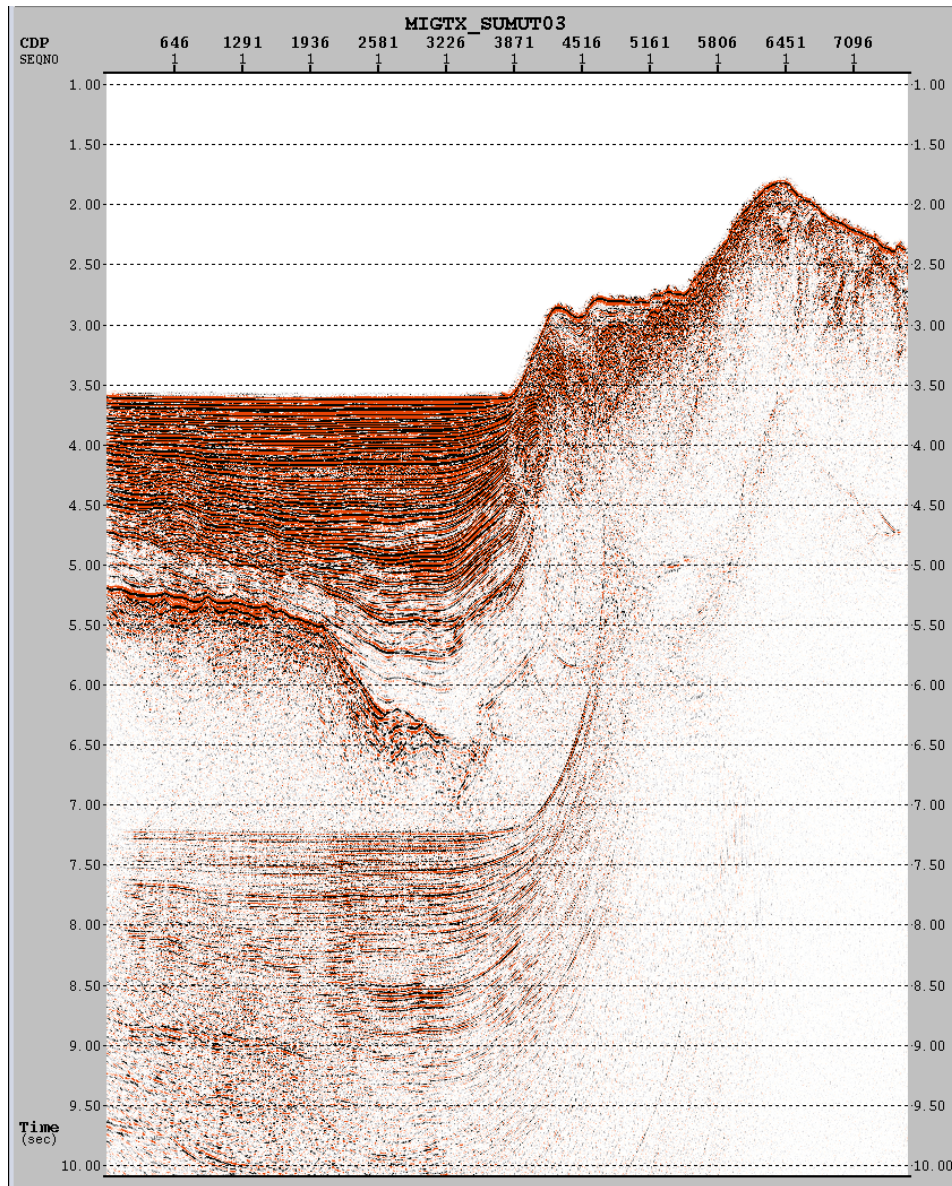
Mute: picked during interactive velocity analysis, ~0.5s above seafloor

Stack: Median, trim rate of 20%

Note: Median stack designed to minimize swell noise in the final section.



Time-Space Kirchhoff Migration: 800 trace lateral and 1000ms vertical smoothing operators



Mute applied 50ms above seafloor

Final product output from focus in segy format and imported into Geoframe. Plots made using the Geoframe scaled hardcopy command.

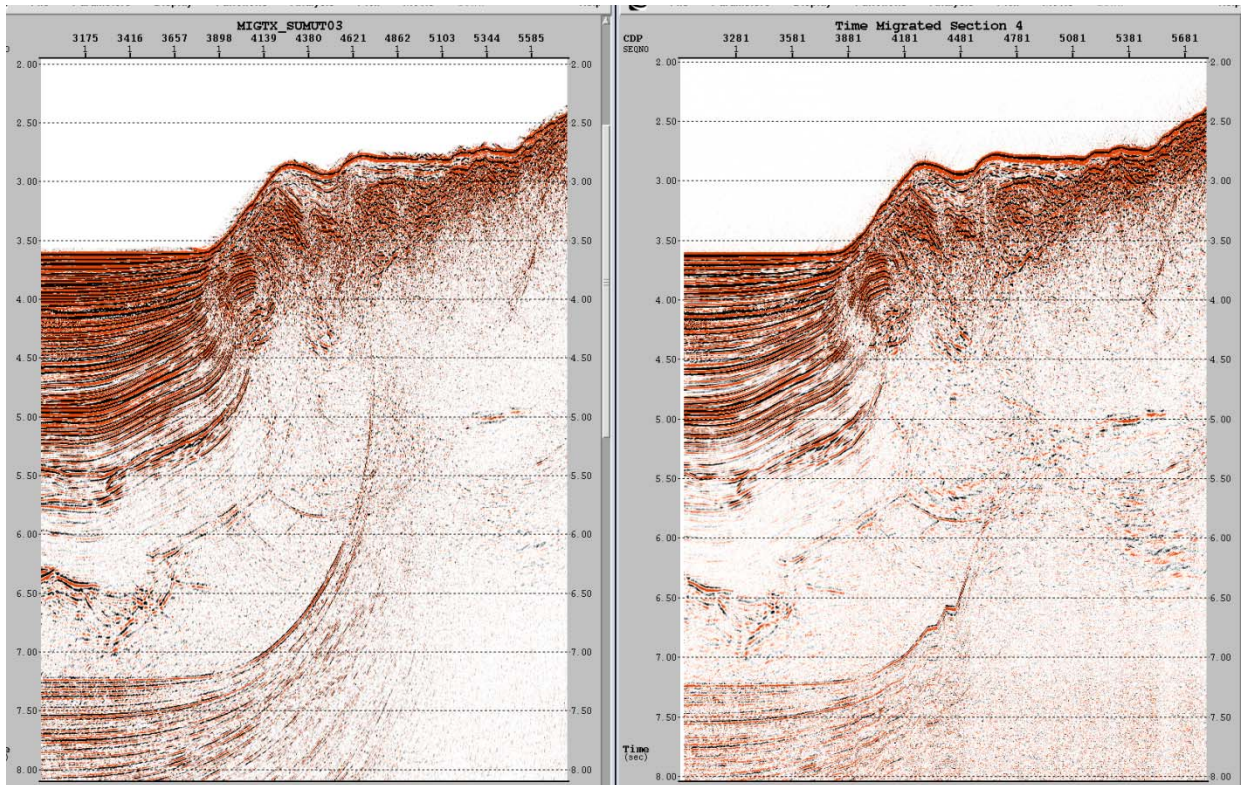
## **APPENDIX F: SUMUT PRE-STACK MIGRATION PROCESSING FLOW**

Pre-stack migration was performed on portions of lines SUMUT 01, 03, 05 and 07 where these lines cross the West Andaman Fault at the edge of the Aceh Forearc Basin. Steps 1-7 are the same as above, without the gain function.

- Read in shots from SEG-D file
- Define geometry
- Export shot times from focus and calculate ship's position at each time from 1-second navigation data
- Find average shot spacing by utilizing Open Office
- Define station locations every 1.25m along a line
- Call PATTERN to define receiver locations relative to shots
- Call SOURCE
- Define first shot location such that far offset receiver is at station 1
- Set shot spacing to even number of stations
- Desample: 4ms
- Bandpass filter: 3-6-60-80 Hz minimum phase
- Kill trace 192 (consistently noisy)
- Multichannel predictive (GAP) deconvolution: minimum phase with 11 trace window, 300 ms operator and 24 ms gap length, design window of 3s starting below seafloor
- Sort: bin traces into CMPs (defined every 6.25m)

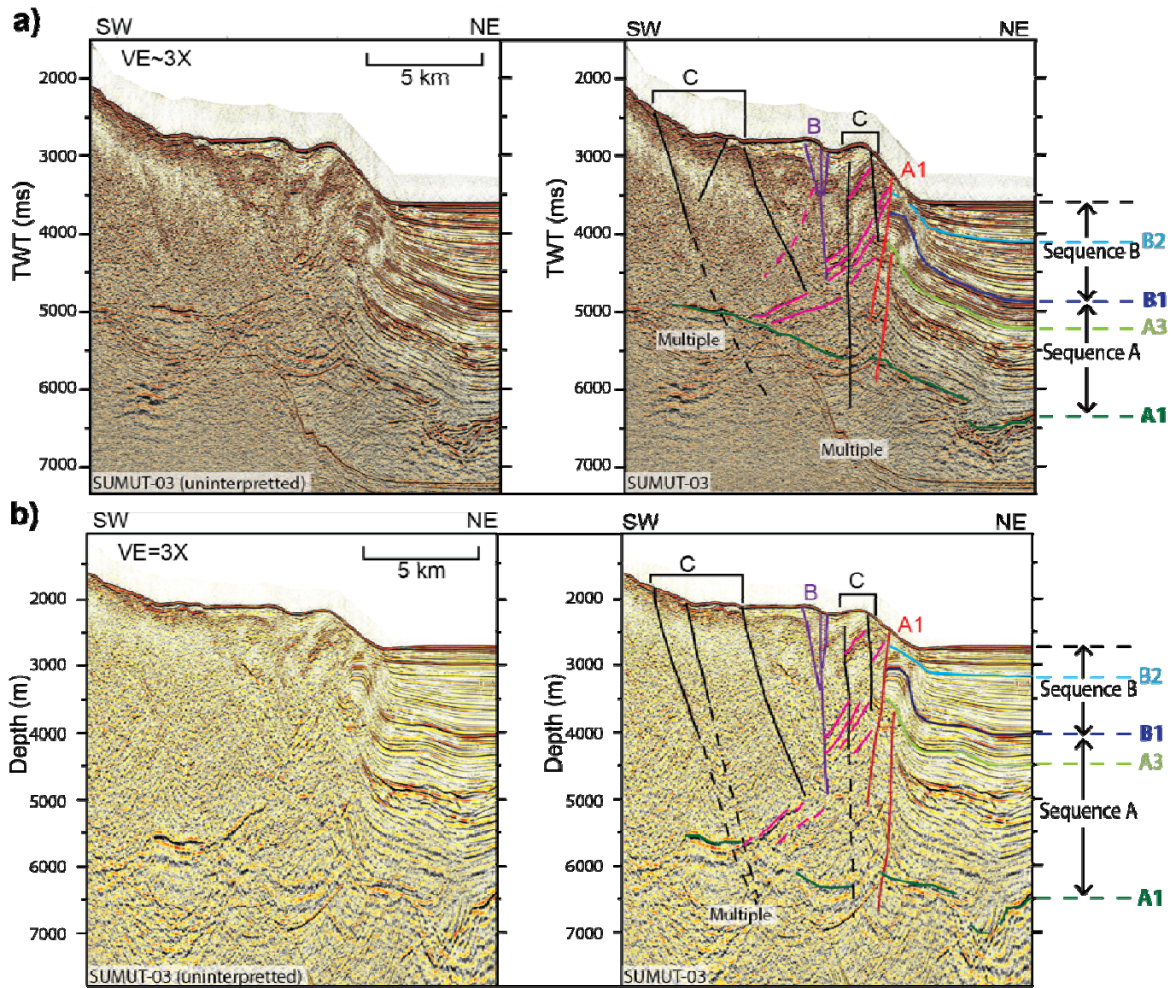
Following step 7, I performed a 2D Kirchoff pre-stack time migration using the "Travel Times by Curve Fitting" module in Geodepth. This module calculated the p-wave travel times by second order curve fitting using the velocity section picked in the

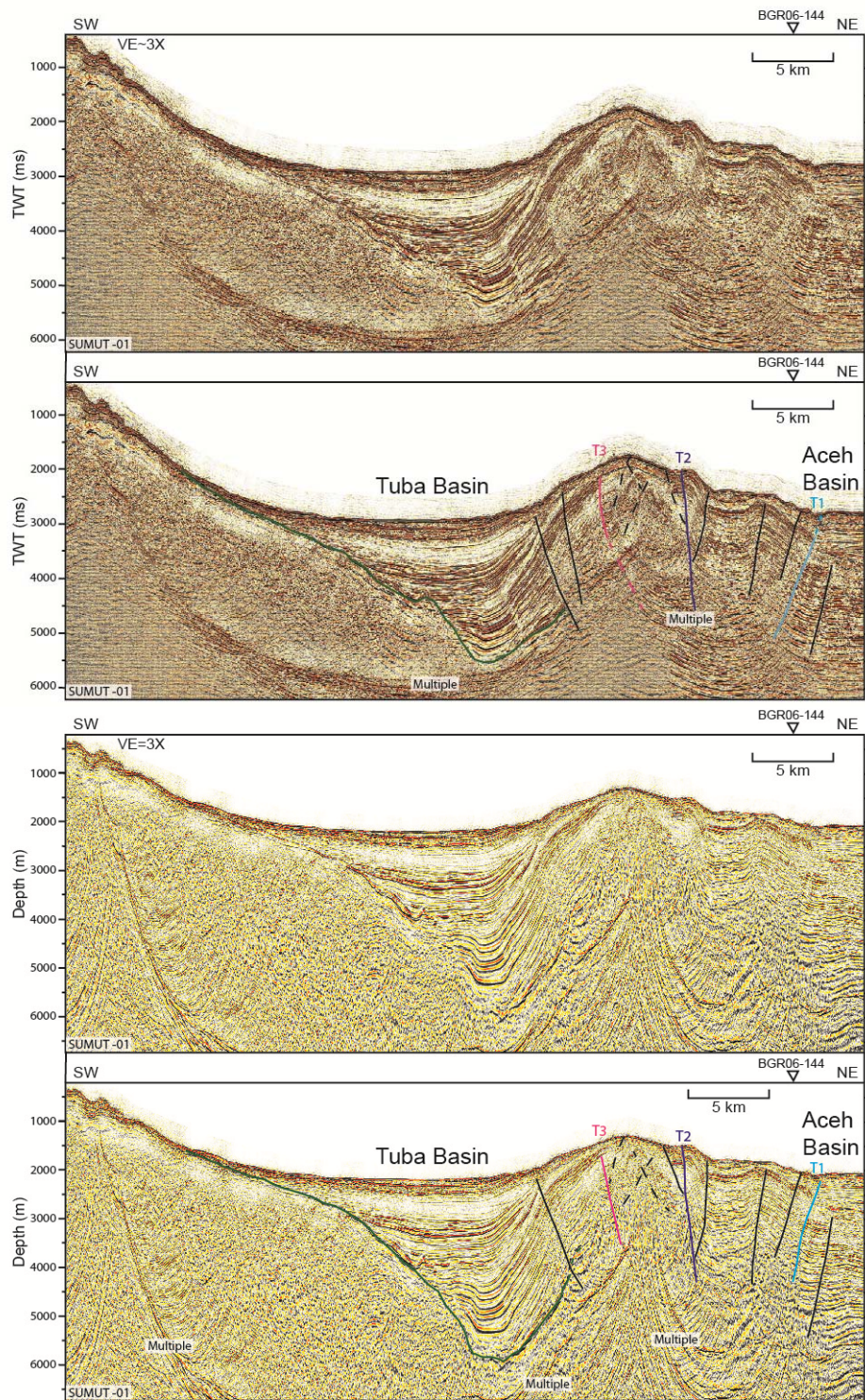
initial round of processing (see Appendix E). I used residual moveout analysis to refine the velocity section before producing the final migrated sections presented in Chapter 4. The images produced by this pre-stack migration are less noisy and allow for more certain interpretation than the images produced by the post-stack migration above (see figure below). In particular, the pre-stack images exhibit smoother basin sediment reflections with more variability in the brightness of these reflections. Also, the over-migration artifacts from the multiple are less obvious and the multiple itself is somewhat weaker in amplitude, allowing better visibility of the low-frequency reflector A1.



## APPENDIX G: EXAMPLE PRE-STACK DEPTH MIGRATIONS

Pre-stack depth migrations were run for lines SUMUT-03 and SUMUT-01 using a processing flow similar to that described in Appendix F for the pre-stack time migration. The resultant images are shown here and yield interpretations similar to those made on the pre-stack time sections.





## References

- Allen, D., S. Bonner, A. Bagersh, B. Clark, G. Dajee, M. Dennison, J. S. Hall, J. Jundt, J. Lovell, and R. Rosthal (1994), A new generation of electrode resistivity measurements for formation evaluation while drilling, in SPWLA 35th Annual Logging Symposium, edited, p. 25, Society of Petrophysicists & Well Log Analysts.
- Ammon, C. J., et al. (2005), Rupture Process of the 2004 Sumatra-Andaman Earthquake Science, 308(5725), 1133 - 1139.
- Ashi, J., S. Lallement, and H. Masago (2007), NanTroSEIZE Stage 1: NanTroSEIZE megasplay riser pilot, IODP Sci. Prosp., 315. doi: 10.2204/iodp.sp.315.2007.
- Baba, T., P. R. Cummins, T. Hori, and Y. Kaneda (2006), High precision slip distribution of the 1944 Tonankai earthquake inferred from tsunami waveforms: Possible slip on a splay fault, Tectonophysics, 426, 119-134.
- Bangs, N. L. B., T. H. Shipley, and G. F. Moore (1996), Elevated fluid pressure and fault zone dilation inferred from seismic models of the northern Barbados Ridge decollement, Journal of Geophysical Research-Solid Earth, 101(B1), 627-642.
- Bangs, N. L. B., S. P. S. Gulick, and T. H. Shipley (2006), Seamount subduction erosion in the Nankai Trough and its potential impact on the seismogenic zone, Geology, 34(8), 701-704.
- Bangs, N. L. B., T. H. Shipley, S. P. S. Gulick, G. F. Moore, S. Kuromoto, and Y. Nakamura (2004), Evolution of the Nankai Trough decollement from the trench into the seismogenic zone: Inferences from three-dimensional seismic reflection imaging, Geology, 32(4), 273-276.
- Bangs, N. L. B., G. F. Moore, S. P. S. Gulick, E. M. Pangborn, H. J. Tobin, S. Kuramoto, and A. Taira (2009), Broad, weak regions of the Nankai Megathrust and implications for shallow coseismic slip, Earth and Planetary Science Letters, 284(1-2), 44-49.
- Beaudry, D., and G. F. Moore (1985), Seismic stratigraphy and Cenozoic evolution of west Sumatra fore-arc basins, Aapg Bulletin-American Association of Petroleum Geologists, 69(5), 742-759.
- Berglar, K., C. Gaedicke, D. Franke, S. Ladage, F. Klingelhoefer, and Y. S. Djajadihardja (2010), Structural evolution and strike-slip tectonics off north-western Sumatra, Tectonophysics, 480, 119-132.
- Bird, R. B., W. E. Stewart, and E. N. Lightfoot (2007), Transport Phenomena, Rev. 2nd Edition ed., 905 pp., J. Wiley, New York.

- Carslaw, H. S., and J. C. Jaeger (1959), *Conduction of Heat in Solids*, 2nd ed., 510 pp., Clarendon Press, Oxford.
- Chauhan, A. P. S., S. C. Singh, N. D. Hananto, H. Carton, F. Klingelhoefer, J.-X. Dessa, H. Permana, N. J. White, D. Graindorge, and SumatraOBS Scientific Team (2009), Seismic imaging of forearc backthrusts at northern Sumatra subduction zone, *Geophysical Journal International*, 179, 1772-1780.
- Cobern, M. E., and E. B. Nuchols (1985), Application of MWD resistivity logs to evaluation of formation invasion, in *SPWLA 26th Annual Logging Symposium*, edited, pp. 1-16.
- Cochran, J. R. (2010), Morphology and tectonics of the Andaman Forearc, northeastern Indian Ocean, *Geophysical Journal International*, 182(2), 631-651.
- Cozzolino, K., A. Q. Howard, Jr., and J. S. Protázio (2000), A new look at multiphase invasion with applications to borehole resistivity interpretation, *Journal of Applied Geophysics*, 43, 91-100.
- Craig, R. F. (2004), *Craig's Soil Mechanics*, Seventh ed., 447 pp., Spon Press, New York.
- Curry, J. R. (2005), Tectonics and history of the Andaman Sea region, *Journal of Asian Earth Sciences*, 25(1), 187-228.
- Dahlen, F. A., J. Suppe, and D. Davis (1984), Mechanics of fold-and-thrust belts and accretionary wedges - cohesive Coulomb theory, *Journal of Geophysical Research*, 89(NB12), 87-101.
- Davis, D., J. Suppe, and F. A. Dahlen (1983), Mechanics of Fold-and-Thrust Belts and Accretionary Wedges, *Journal of Geophysical Research*, 88(NB2), 1153-1172.
- Dean, S. M., L. C. McNeill, T. J. Henstock, J. M. Bull, S. P. S. Gulick, J. A. Austin, N. L. B. Bangs, Y. S. Djajadihardja, and H. Permana (2010), Contrasting Decollement and Prism Properties over the Sumatra 2004-2005 Earthquake Rupture Boundary, *Science*, 329(5988), 207-210.
- Delescluse, M., and N. Chamotrooke (2007), Instantaneous deformation and kinematics of the India-Australia Plate, *Geophysical Journal International*, 168(2), 818-842.
- DeMets, C., R. G. Gordon, and J. Y. Royer (2005), Motion between the Indian, Capricorn and Somalian plates since 20 Ma: implications for the timing and magnitude of distributed lithospheric deformation in the equatorial Indian ocean, *Geophysical Journal International*, 161(2), 445-468.
- DeMets, C., R. G. Gordon, and D. F. Argus (2010), Geologically current plate motions, *Geophysical Journal International*, 181(1), 1-80.
- Diament, M., H. Harjono, K. Karta, C. Deplus, and F. Dahrin (1992), Mentawai fault zone off Sumatra: A new key to the geodynamics of western Indonesia, *Geology*, 20, 259-261.

- Dobson, M. R., H. A. Karl, and T. L. Vallier (1996), Sedimentation Along the Fore-Arc Region of the Aleutian Island Arc, Alaska, in *Geology of the United States' Seafloor: The View from GLORIA*, edited by J. V. Gardner, M. E. Field and D. C. Twichell, pp. 279-304, Cambridge University Press.
- Dugan, B., and H. Daigle (2010), Data Report: Permeability, compressibility, stress state and grain-size of shallow sediments from the Sites C0004, C0006, C0007 and C0008 of the Nankai accretionary complex. In M. Kinoshita, H. Tobin, J. Ashi, G. Kimura, S. Lallemand, E. J. Screaton, D. Curewitz, H. Masago, K. T. Moe and the Expedition 314/315/316 Scientists, *Proc. IODP, 314/315/316: Washington, DC (Integrated Ocean Drilling Program Management International, Inc.)*.
- Dunbar, P. (2010), National Geophysical Data Center Tsunami Runup Database, edited, NOAA Satellite and Information Service.
- Ellis, D. V., and J. M. Singer (2007), *Well Logging for Earth Scientists*, 2nd ed., 692 pp., Singer.
- Expedition 314 Scientists (2009a), Expedition 314 Site C0004. In M. Kinoshita, H. Tobin, J. Ashi, G. Kimura, S. Lallemand, E. J. Screaton, D. Curewitz, H. Masago, K. T. Moe and the Expedition 314/315/316 Scientists, *Proc. IODP, 314/315/316: Washington, DC (Integrated Ocean Drilling Program Management International, Inc.)*.
- Expedition 314 Scientists (2009b), Expedition 314 Site C0001. In M. Kinoshita, H. Tobin, J. Ashi, G. Kimura, S. Lallemand, E. J. Screaton, D. Curewitz, H. Masago, K. T. Moe and the Expedition 314/315/316 Scientists, *Proc. IODP, 314/315/316: Washington, DC (Integrated Ocean Drilling Program Management International, Inc.)*.
- Expedition 314 Scientists (2009c), Expedition 314 Site C0006. In M. Kinoshita, H. Tobin, J. Ashi, G. Kimura, S. Lallemand, E. J. Screaton, D. Curewitz, H. Masago, K. T. Moe and the Expedition 314/315/316 Scientists, *Proc. IODP, 314/315/316: Washington, DC (Integrated Ocean Drilling Program Management International, Inc.)*.
- Fisher, D., D. Mosher, J. A. Austin, S. P. S. Gulick, T. Masterlark, and K. Moran (2007), Active deformation across the Sumatran forearc over the December 2004 Mw 9.2 rupture, *Geology*, 35(2), 99-102.
- Fitch, T. J. (1972), Plate Convergence, Transcurrent Faults, and Internal Deformation Adjacent to Southeast Asia and the Western Pacific, *Journal of Geophysical Research*, 77(23), 4432-4460.
- Franke, D., M. Schnabel, S. Ladage, D. R. Tappin, S. Neben, Y. S. Djajadihardja, C. Muller, H. Kopp, and C. Gaedicke (2008), The great Sumatra-Andaman earthquakes - Imaging the boundary between the ruptures of the great 2004 and 2005 earthquakes, *Earth and Planetary Science Letters*, 269(1-2), 118-130.

- Fuller, C. W., S. D. Willett, and M. T. Brandon (2006), Formation of forearc basins and their influence on subduction zone earthquakes, *Geology*, 34(2), 65-68.
- Gamage, K., and E. Screaton (2003), Data Report: Permeabilities of Nankai accretionary prism sediments. In H. Mikada, G. F. Moore, A. Taira, K. Becker, J. C. Moore and A. Klaus, *Proc. Ocean Drill. Program Sci. Results*, 190/196: College Station, TX (Ocean Drilling Program), 1-22 [Online]. doi: 10.2973/odp.proc.sr.190196.213.2003.
- Goldfinger, C., L. D. Kulm, R. S. Yeats, L. C. McNeill, and C. Hummon (1997), Oblique strike-slip faulting of the central Cascadia submarine forearc, *Journal of Geophysical Research-Solid Earth*, 102(B4), 8217-8243.
- Graindorge, D., et al. (2008), Impact of lower plate structure on upper plate deformation at the NW Sumatran convergent margin from seafloor morphology, *Earth and Planetary Science Letters*, 275(3-4), 201-210.
- Gulick, S. P. S., and N. L. B. Bangs (2004), Negative polarity at the frontal thrust - is free gas the culprit?: insights from Nankai accretionary prism off Cape Muroto using seismic-logging integration. In H. Mikada, G. F. Moore, A. Taira, K. Becker, J. C. Moore and A. Klaus, *Proc. ODP, Scientific Results*, 190/196: College Station, TX (Ocean Drilling Program).
- Gulick, S. P. S., N. L. B. Bangs, T. H. Shipley, Y. Nakamura, G. F. Moore, and S. i. Kuramoto (2004), Three-dimensional architecture of the Nankai accretionary prism's imbricate thrust zone off Cape Muroto, Japan: Prism reconstruction via en echelon thrust propagation, *Journal of Geophysical Research*, 109.
- Gulick, S. P. S., N. L. B. Bangs, G. F. Moore, J. Ashi, K. M. Martin, D. S. Sawyer, H. J. Tobin, S. Kuramoto, and A. Taira (2010), Rapid forearc basin uplift and megasplay fault development from 3D seismic images of Nankai Margin off Kii Peninsula, Japan, *Earth and Planetary Science Letters*, 300(1-2), 55-62.
- Gulick, S. P. S., J. A. Austin, L. C. McNeill, N. L. B. Bangs, K. M. Martin, T. J. Henstock, J. M. Bull, S. Dean, Y. S. Djajadihardja, and H. Permana (2011), Updip rupture of the 2004 Sumatra earthquake extended by thick indurated sediments, *Nat Geosci*, 4(7), 453-456.
- Henstock, T. J., L. C. McNeill, and D. R. Tappin (2006), Seafloor morphology of the Sumatran subduction zone: Surface rupture during megathrust earthquakes?, *Geology*, 34(6), 485-488.
- Hubbert, M. K., and W. W. Rubey (1959), Role of fluid pressure in mechanics of overthrust faulting, I. Mechanics of fluid-filled porous solids and its application to overthrust faulting, *Geol. Soc. America Bull.*, 70, 115-166.
- Huchon, P., H. Tokuyama, S. Lallemand, A. Taira, P. Henry, S. Mazzotti, X. Le Pichon, and t. K.-T. o.-b. s. party (1998), Pervasive dextral strike-slip faulting within the

- backstop of the Eastern Nankai wedge confirmed by the deep-towed seismic data (Kaiko-Tokai 1996 cruise), *C. R. Acad. Sci.*, 326, 869-875.
- Ishii, M., P. M. Shearer, H. Houston, and J. E. Vidale (2005), Extent, duration and speed of the 2004 Sumatra-Andaman earthquake imaged by the Hi-Net array, *Nature*, 435(7044), 933-936.
- Jarrard, R. D. (1986), Terrane Motion by Strike-Slip Faulting of Fore-Arc Slivers, *Geology*, 14(9), 780-783.
- Karig, D. E., S. Suparka, G. F. Moore, and P. E. Hehanussa (1979), Structure and Cenozoic Evolution of the Sunda Arc in the Central Sumatra Region, in *Geological and Geophysical Investigations of Continental Margins*, edited by J. S. Watkins, L. Montadert and P. W. Dickerson, pp. 223-237.
- Karig, D. E., M. B. Lawrence, G. F. Moore, and J. R. Curray (1980), Structural Framework of the Fore-Arc Basin, Nw Sumatra, *Journal of the Geological Society*, 137(JAN), 77-91.
- Kimura, G., Y. Kitamura, Y. Hashimoto, A. Yamaguchi, T. Shibata, K. Ujiie, and S. Okamoto (2007), Transition of accretionary wedge structures around the up-dip limit of the seismogenic subduction zone, *Earth and Planetary Science Letters*, 255(3-4), 471-484.
- Kinoshita, M., H. J. Tobin, and K. T. Moe (2007), NanTroSEIZE Stage 1: LWD transect, *IODP Sci. Prosp.*, 314. doi: 10.2204/iodp.sp.314.2007.
- Kinoshita, M., H. Tobin, K. T. Moe, and the Expedition 314 Scientists (2008), NanTroSEIZE Stage 1A: NanTroSEIZE LWD transect, *IODP Prel. Rept.*, 314. doi: 10.2204/iodp.pr.314.2008.
- Kinoshita, M., H. Tobin, J. Ashi, G. Kimura, S. Lallemand, E. J. Screaton, D. Curewitz, H. Masago, K. T. Moe, and the Expedition 314/315/316 Scientists (2009), *Proc. IODP*, 314/315/316. doi: 10.2204/iodp.proc.314315316.2009.
- Krabbenhoft, A., R. W. Weinrebe, H. Kopp, E. R. Flueh, S. Ladage, C. Papenberg, L. Planert, and Y. Djajadihardja (2010), Bathymetry of the Indonesian Sunda margin-relating morphological features of the upper plate slopes to the location and extent of the seismogenic zone, *Natural Hazards and Earth System Sciences*, 10(9), 1899-1911.
- Lallemand, S. E., P. Schnurle, and J. Malavieille (1994), Coulomb Theory Applied to Accretionary and Nonaccretionary Wedges - Possible Causes for Tectonic Erosion and or Frontal Accretion, *Journal of Geophysical Research-Solid Earth*, 99(B6), 12033-12055.
- Long, H., P. B. Flemings, J. T. Germaine, D. M. Saffer, and B. Dugan (2008), Data Report: consolidation characteristics of sediments from IODP Expedition 308, Ursa Basin, Gulf of Mexico. In P. B. Flemings, J. Behrmann, C. M. John and t. E.

- Scientists, Proc. IODP, 308: Washington, DC (Integrated Ocean Drilling Program Management International, Inc.)10.2204/iodp.proc.308.204.2008.
- Malod, J. A., and B. M. Kemal (1996), The Sumatran margin: oblique subduction and lateral displacement of the accretionary prism, in Geological Society, London, Special Publications, edited, pp. 19-28, London.
- Manaker, D. M., E. Calais, A. M. Freed, S. T. Ali, P. Przybylski, G. Mattioli, P. Jansma, C. Prepetit, and J. B. de Chabaliere (2008), Interseismic Plate coupling and strain partitioning in the Northeastern Caribbean, *Geophysical Journal International*, 174(3), 889-903.
- Martin, K. M., S. P. S. Gulick, and J. A. Austin (2011), The West Andaman fault as a strain partitioning structure in the Sumatran forearc, in British Geophysical Association New Advances in Geophysics meeting 2011: Controlling factors of subduction zone earthquakes, edited, London, England.
- Martin, K. M., S. P. S. Gulick, N. L. B. Bangs, G. F. Moore, J. Ashi, J. O. Park, S. i. Kuramoto, and A. Taira (2010), Possible Strain Partitioning Structure Between the Kumano Forearc Basin and the Slope of the Nankai Trough Accretionary Prism, *Geochemistry Geophysics Geosystems*, 11(B12), Q0AD02.
- McCaffrey, R. (1991), Slip vectors and stretching of the Sumatran fore arc, *Geology*, 19, 881-884.
- McCaffrey, R. (1993), On the Role of the Upper Plate in Great Subduction Zone Earthquakes, *Journal of Geophysical Research-Solid Earth*, 98(B7), 11953-11966.
- McCaffrey, R. (2009), The Tectonic Framework of the Sumatran Subduction Zone, *Annual Review of Earth and Planetary Sciences*, 37, 345-366.
- McCaffrey, R., P. C. Zwick, Y. Bock, L. Prawirodirdjo, J. F. Genrich, C. W. Stevens, S. S. O. Puntodewo, and C. Subarya (2000), Strain partitioning during oblique plate convergence in northern Sumatra: Geodetic and seismologic constraints and numerical modeling, *Journal of Geophysical Research-Solid Earth*, 105(B12), 28363-28376.
- Meltzner, A. J., K. Sieh, M. Abrams, D. C. Agnew, K. W. Hudnut, J. P. Avouac, and D. H. Natawidjaja (2006), Uplift and subsidence associated with the great Aceh-Andaman earthquake of 2004, *Journal of Geophysical Research-Solid Earth*, 111(B2).
- Mikada, H., G. F. Moore, A. Taira, K. Becker, J. C. Moore, and A. Klaus (2005), Proc. ODP, Sci. Results, 190/196. doi: 10.2973/odp.proc.sr.190196.2005.
- Moore, G. F., J. R. Curran, and F. J. Emmel (1982), Sedimentation in the Sunda Trench and forearc region, Geological Society, London, Special Publications, 10, 245-258.

- Moore, G. F., N. L. B. Bangs, A. Taira, S. i. Kuramoto, E. M. Pangborn, and H. J. Tobin (2007), Three-Dimensional Splay Fault Geometry and Implications for Tsunami Generation, *Science*, 318, 1128 – 1131.
- Moore, G. F., et al. (2009), Structural and Seismic Stratigraphic Framework of the NanTroSEIZE Stage 1 Transect: Kumano 3D Seismic Survey. In M. Kinoshita, H. Tobin, J. Ashi, G. Kimura, S. Lallemand, E. J. Screaton, D. Curewitz, H. Masago, K. T. Moe and the Expedition 314/315/316 Scientists, Proc. IODP, 314/315/316: College Station, TX (Integrated Ocean Drilling Program Management International, Inc.), 1-46. doi: 10.2204/iodp.proc.314315316.102.2009
- Moore, J. C., G. F. Moore, G. R. Cochrane, and H. J. Tobin (1995), Negative-polarity seismic reflections along faults of the Oregon accretionary prism - indicators of overpressuring, *Journal of Geophysical Research-Solid Earth*, 100(B7), 12895-12906.
- Moore, J. C., et al. (1998), Consolidation patterns during initiation and evolution of a plate-boundary decollement zone: Northern Barbados accretionary prism, *Geology*, 26(9), 811-814.
- Moran, K., and D. R. Tappin (2006), SEATOS 2005 Cruise Report: Sumatra Earthquake and Tsunami Off shore Survey (SEATOS), edited, p. 92.
- Morley, C. K. (2007), Development of crestal normal faults associated with deep water fold growth, *Journal of Structural Geology*, 29, 1148-1163.
- Mosher, D. C., J. A. Austin, D. Fisher, and S. P. S. Gulick (2008), Deformation of the northern Sumatra accretionary prism from high-resolution seismic reflection profiles and ROV observations, *Marine Geology*.
- Nelson, P. (1994), Permeability-porosity relationships in sedimentary rocks., *The Log Analyst*, 35(3), 38-62.
- Neuzil, C. E. (1994), How permeable are clays and shales?, *Water Resources Research*, 30(2), 145-150.
- Neuzil, C. E. (1995), Abnormal pressures as hydrodynamic phenomena, *American Journal of Science*, 295(6), 742-786.
- Nishimura, S., and M. Hashimoto (2006), A model with rigid rotations and slip deficits for the GPS-derived velocity field in Southwest Japan, *Tectonophysics*, 421(3-4), 187-207.
- Pangborn, E. M. (2007), Thrust fault characteristics inferred from 3D seismic reflection data from the Nankai Trough subduction zone, southwest Japan, PhD thesis, 97 pp, University of Texas at Austin, Austin, Texas.
- Park, J.-O., T. Tsuru, S. Kodaira, P. R. Cummins, and Y. Kaneda (2002), Splay Fault Branching Along the Nankai Subduction Zone *Science*, 297(5584), 1157-1160.

- Rajendran, K., V. Andrade, and C. P. Rajendran (2011), The June 2010 Nicobar Earthquake: Fault Reactivation on the Subducting Oceanic Plate, *Bulletin of the Seismological Society of America*, 101(5), 2568-2577.
- Rider, M. (2000), *The Geological Interpretation of Well Logs*, 2nd ed., 280 pp., Rider-French Consulting Ltd., Sutherland, Scotland.
- Rowe, K., E. Screaton, J. Guo, and M. B. Underwood (2010), Data Report: Permeabilities of sediments from the Kumano Basin Transect offshore the Kii Peninsula, Japan. In M. Kinoshita, H. Tobin, J. Ashi, G. Kimura, S. Lallemand, E. J. Screaton, D. Curewitz, H. Masago, K. T. Moe and the Expedition 314/315/316 Scientists, *Proc. IODP, 314/315/316: Washington DC (Integrated Ocean Drilling Program Management International, Inc.)*.
- Ryan, H. F., and D. W. Scholl (1989), The evolution of fore-arc structures along an oblique convergent margin, central Aleutian Arc, *Tectonics*, 8(3), 497-516.
- Saffer, D. M. (2010), Hydrostratigraphy as a control on subduction zone mechanics through its effects on drainage: an example from the Nankai Margin, SW Japan, *Geofluids*, 10, 114-131.
- Saffer, D. M., and B. A. Bekins (1998), Episodic fluid flow in the Nankai accretionary complex: Timescale, geochemistry, flow rates, and fluid budget, *Journal of Geophysical Research*, 103(B12), 30,351-330,370.
- Saffer, D. M., and B. A. Bekins (2002), Hydrologic controls on the morphology and mechanics of accretionary wedges, *Geology*, 30(3), 4.
- Saffer, D. M., and B. A. Bekins (2006), An evaluation of factors influencing pore pressure in accretionary complexes: Implications for taper angle and wedge mechanics, *Journal of Geophysical Research-Solid Earth*, 111(B4).
- Saffer, D. M., J. Guo, M. B. Underwood, W. Likos, R. M. Skarbek, I. Song, and M. Gildow (2010a), Data Report: Consolidation and Permeability of sediments from the Nankai continental slope, IODP Sites C0001, C0008, and C0004. In M. Kinoshita, H. Tobin, J. Ashi, G. Kimura, S. Lallemand, E. J. Screaton, D. Curewitz, H. Masago, K. T. Moe and the Expedition 314/315/316 Scientists, *Proc. IODP, 314/315/316: Washington, DC (Integrated Ocean Drilling Program Management International, Inc.)*.
- Saffer, D. M., L. C. McNeill, T. B. Byrne, E. Araki, S. Toczko, N. Eguchi, K. Takahashi, and t. E. Scientists NanTroSEIZE Stage 2: NanTroSEIZE riser/riserless observatory, *Proc. IODP*, 319.
- Saffer, D. M., L. C. McNeill, T. B. Byrne, E. Araki, S. Toczko, N. Eguchi, K. Takahashi, and t. E. Scientists (2010b), *Proc. IODP*. doi: 10.2204/iodp.proc.319.2010.
- Saito, S., M. B. Underwood, Y. Kubo, and t. E. Scientists (2010), in *Proc. IODP*, edited, Integrated Ocean Drilling Program Management International, Inc., Tokyo.

- Salazar, J. M., C. Torres-Verdin, and R. Sigal (2005), Assessment of permeability from well logs based on core calibration and simulation of mud-filtrate invasion, *Petrophysics*, 46(6), 434-451.
- Samuel, M. A., and N. A. Harbury (1996), The Mentawai fault zone and deformation of the Sumatran Forearc in the Nias area, Geological Society, London, Special Publications, 106, 337-351.
- Satake, K., and B. F. Atwater (2007), Long-term perspectives on giant earthquakes and tsunamis at subduction zones, *Annual Review of Earth and Planetary Sciences*, 35, 349-374.
- Schlumberger (2000), HRLA High-Resolution Laterolog Array Tool: Improving the accuracy of Rt, edited by Schlumberger, Schlumberger.
- Schlumberger (2009), Log Interpretation Charts, edited, p. 306, Schlumberger.
- Screaton, E. J., D. R. Wuthrich, and S. J. Dreiss (1990), Permeabilities, fluid pressures, and flow-rates in the Barbados Ridge Complex, *Journal of Geophysical Research-Solid Earth and Planets*, 95(B6), 8997-9007.
- Seeber, L., C. Mueller, T. Fujiwara, K. Arai, W. Soh, Y. S. Djajadihardja, and M. H. Cormier (2007), Accretion, mass wasting, and partitioned strain over the 26 Dec 2004 Mw9.2 rupture offshore Aceh, northern Sumatra, *Earth and Planetary Science Letters*, 263(1-2), 16-31.
- Seno, T., S. Stein, and A. E. Gripp (1993), A Model for the Motion of the Philippine Sea Plate Consistent with Nuvel-1 and Geological Data, *Journal of Geophysical Research-Solid Earth*, 98(B10), 17941-17948.
- Shipley, T. H., G. F. Moore, N. L. B. Bangs, J. C. Moore, and P. L. Stoffa (1994), Seismically inferred dilatancy distribution, northern Barbados Ridge decollement - implications for fluid migration and fault strength, *Geology*, 22(5), 411-414.
- Sieh, K., and D. Natawidjaja (2000), Neotectonics of the Sumatran fault, Indonesia, *Journal of Geophysical Research-Solid Earth*, 105(B12), 28295-28326.
- Simons, W. J. F., et al. (2007), A decade of GPS in Southeast Asia: Resolving Sundaland motion and boundaries, *Journal of Geophysical Research-Solid Earth*, 112(B6).
- Singh, S. C., N. D. Hananto, and A. P. S. Chauhan (2011), Enhanced reflectivity of backthrusts in the recent great Sumatran earthquake rupture zones, *Geophysical Research Letters*, 38.
- Singh, S. C., N. D. Hananto, A. P. S. Chauhan, H. Permana, M. Denolle, A. Hendriyana, and D. Natawidjaja (2010), Evidence of active backthrusting at the NE Margin of Mentawai Islands, SW Sumatra, *Geophysical Journal International*, 180(2), 703-714.

- Song, T. R. A., and M. Simons (2003), Large trench-parallel gravity variations predict seismogenic behavior in subduction zones, *Science*, 301(5633), 630-633.
- Subarya, C., M. Chlieh, L. Prawirodirdjo, J. P. Avouac, Y. Bock, K. Sieh, A. J. Meltzner, D. H. Natawidjaja, and R. McCaffrey (2006), Plate-boundary deformation associated with the great Sumatra-Andaman earthquake, *Nature*, 440(7080), 46-51.
- Tabai, T., et al. (2002), Subsurface structure and faulting of the Median Tectonic Line, southwest Japan inferred from GPS velocity field, *Earth Planets and Space*, 54, 1065-1070.
- Taira, A., et al. (1992), Sediment Deformation and Hydrogeology of the Nankai Trough Accretionary Prism - Synthesis of Shipboard Results of Odp Leg 131, *Earth and Planetary Science Letters*, 109(3-4), 431-450.
- Taylor, E., and A. Fisher (1993), Sediment permeability at the Nankai Accretionary prism, Site 808, *Proc. Ocean Drill. Program Sci. Results*, 131: College Station, TX (Ocean Drilling Program), 235-245. doi: 10.2973/odp.proc.sr.131.131.1993.
- Terzaghi, K., and R. B. Peck (1967), *Soil mechanics in engineering practice*, J. Wiley, New York.
- Tokuyama, H., J. Ashi, W. Soh, S. Kuramoto, and Y. Ikeda (1999), *Active submarine faults off Tokai: Results from the Japan-France Kaiko-Tokai Project*: Tokyo, Univ, 151 pp., Tokyo Press.
- Uraki, S., Y. Kido, Y. Sanada, S. Kuramoto, T. Okano, H. Saga, J. O. Park, G. F. Moore, and A. Taira (2009), Kumano-nada 3D seismic data acquisition and processing, *Butsuri-Tansa*, 62(2), 277-288.
- van der Werff, W. (1996), Variation in forearc basin development along the Sunda Arc, Indonesia, *Journal of Southeast Asian Earth Sciences*, 14(5), 331-349.
- Wang, K., and Y. Hu (2006), Accretionary prisms in subduction earthquake cycles: The theory of dynamic Coulomb wedge, *Journal of Geophysical Research*, 111(B06410).
- Weisstein, E. W. (2007), Péclet Number in Eric Weisstein's World of Physics, edited.
- Wells, R. E., R. J. Blakely, Y. Sugiyama, D. W. Scholl, and P. A. Dinterman (2003), Basin-centered asperities in great subduction zone earthquakes: a link between slip, subsidence and subduction erosion?, *Journal of Geophysical Research*, 108(B10).